FIRST PRINCIPLES STUDY OF NOVEL MATERIALS

Thesis submitted for the degree of
Doctor of Philosophy (Science)

in

Physics (Theoretical)

by

Sudipta Kanungo

Department of Physics
University of Calcutta
May 2013

to

my friend

mahuya

Acknowledgments

At last!!, as a sense of fulfillment, at the completion of this long phase of five years of my life, I wish to acknowledge to all my well wishers who have contributed, influenced and supported explicitly or implicitly during this period.

Naturally, first of all I want to express my sincere and humble gratitude to my respected supervisor Prof. Tanusri Saha-Dasgupta. I have always been benefited by her valuable expert guidance, constant push, endless enthusiasm, prompt ideas with her limitless passion for science. It is my privilege to work with such a science devoted honorable figure like my supervisor. I would like to thank Prof. Kalobaran Maiti of Tata Institute of Fundamental Research, for his kind acceptance to work together with in the very first scientific project of my life. I would like to thanks Prof. Peter Oppeneer of Uppsala University for his wonderful support, help and hospitality during my stay in Uppsala, Sweden. It was a great and valuable experience for me to work with Prof. Oppeneer. I would like to acknowledge "Indo- Swedish joint link project" for funding the same. Thanks to Kartick'da for your all sorts of help in academic as well as non-academic matter in Uppsala.

I am fortunate enough to have a great friend circle in our institute S.N Bose. Due to their presence the environment become always very charming and joyful. It is my pleasure to have such a group mates like; Badiur'da, Soumendu'da, Hena'di, Soumyajit'da, Swastika'di, Swarnakamal, Santu, Hrishit and Kartick. Thanks Hrishit for the painful job you did for me. Special thanks for Soumyajit'da and Swastika'di, for their continuous help and suggestions in any matter at in any situations. The memory of my daily life during my stay in S.N. Bose are very eventful (!!!) and enjoyable due to vibrant presence of friends like; Debmalya, Sirshendu, Prajna, Abhijit, Tanumay, Sandeep, Rajib, Prashant bhai, Jena ji. Thanks to Sudeep (Sudeep Narayan Banerjee) for all sort of computer related technical help he extended to me. I have spent one of my best period of my life here with them. I will really miss the "New Hostel" and "room no. 217", where I have spent this long five years.

Utilizing this scope I would like to thanks to my school days teachers, Utpal'da, Soumen'da, Hemen babu and college teacher Aloke sir for setting up initial interest in subject "Physics". Special acknowledgment goes to my 'baba' who was my first physics teacher at home.

It is obvious that this long journey would not be possible without the unconditional support of my family throughout my life in any situation at any cost. I would like to take this opportunity to express my heart-felt gratitude to my family; baba, ma and didi for understanding me and tolerate me. It will be my audacity if I try to express their contribution in my life.

At last I accord my most special felling to "the best friend of mine", Mahuya (meantime she become my better half). Some time silence tells much more than the words. So just I want to tell her, thanks for everything.

Finally I would like to thank everybody who played important role throughout my journey. As well as I am expressing my apology some one, I forget to mention.

Sudipta Kanungo
Kolkata, India
May, 2013

List of Publications

1. ⋆ Debdutta Lahiri, T. Shibata, S. Chattopadhyay, **Sudipta Kanungo**, T. Saha-Dasgupta, R. S. Singh, Surinder M. Sharma, and Kalobaran Maiti
   Evidence of active role played by the nonmagnetic element Sr in magnetostructural coupling in $SrRuO_3$
   Phys. Rev B 82, 094440 (2010)

2. ⋆ Soumyajit Sarkar,**Sudipta Kanungo**, and T. Saha-Dasgupta *Ab-inito study of low dimensional quantum spin system Sr_3NiPtO_6, Sr_3CuPtO_6, Sr_3NiIrO_6*
   Phys. Rev. B 82, 235122 (2010)

3. ⋆ E. Jakobi, **S. Kanungo**, S. Sarkar, S. Schmitt, and T. Saha-Dasgupta
   LDA+DMFT study of Ru-based perovskite $SrRuO_3$ and $CaRuO_3$
   Phys. Rev B (Rapid) 83, 041103 (2011)

4. ⋆ **Sudipta Kanungo** and T. Saha-Dasgupta
   Pressure driven change in electronic structure of $BiCoO_3$
   Phys. Rev. B 83, 104104 (2011)

5. Paolo Barone, **Sudipta Kanungo**, Silvia Picozzi, and Tanusri Saha-Dasgupta
   Mechanism of ferroelectricity in d3 perovskite: A model study
   Phys. Rev. B 84, 134101 (2011)

6. ⋆ **Sudipta Kanungo** and T. Saha-Dasgupta
   First principle study of organic-inorganic hybrid framework $Mn(C_4H_4O_4)$
   Phys. Rev. B 84, 134415 (2011)

7. ⋆ K. Tarafder,**S. Kanungo**, P. M. Oppeneer, and T. Saha-Dasgupta
   Pressure and Temperature Control of Spin-switchable Metal-organic Coordination Polymers from ab initio Calculations
   Phys. Rev. Lett. 109, 077203 (2012)

8. Hena Das, **Sudipta Kanungo**, and T. Saha-Dasgupta
   First-principles study of magnetoelastic effect in the difluoride compounds MF_2 (M=Mn, Fe, Co, Ni)
   Phys. Rev. B 86, 054422 (2012)

9. ⋆ **Sudipta Kanungo**, Satyaki Kar and T.Saha-Dasgupta
   Tuning of magnetic ground state of spin 1/2 square lattice compound $Zn_2VO(PO_4)_2$ through chemical substitution
   Phys. Rev. B 87, 054431 (2013)

10. Pablo Maldonado, **Sudipta Kanungo**, T. Saha-Dasgupta and P. M Oppeneer
    Two-step Spin-switchable Tetra-nuclear Fe(II) Molecular Solid: Ab-initio Simulations and Predictions
    Communicated

11. **Sudipta Kanungo**, Rina Dutt and T. Saha-Dasgupta
    Evolution of Electronic and Magnetic Properties in Four Polytypes of $BaRuO_3$
    Communicated

Publications marked with ⋆ are reported in this thesis.

Contents

Table of Contents ix

List of Figures xiii

List of Tables xxii

1 Introduction 1
- 1.1 Introduction to Novel Materials . . . 1
- 1.2 Perovskite based Transition Metal Oxides . . . 2
  - 1.2.1 Structure . . . 3
  - 1.2.2 Few interesting perovskites and their emergent physical properties . . . 5
- 1.3 Low Dimensional Quantum Spin System . . . 9
  - 1.3.1 Different classes of quantum spin system . . . 11
- 1.4 Organic-Inorganic Hybrid Systems . . . 13
  - 1.4.1 Classification of Organic-Inorganic Hybrids . . . 14
  - 1.4.2 Different novel physical properties . . . 14
- 1.5 Overview of Present Thesis . . . 16

2 Theoretical Basics of electronic structure calculations 27
- 2.1 Foundation of Density Functional Theory (DFT) . . . 27
  - 2.1.1 The many-electron Hamiltonian . . . 27
  - 2.1.2 Wave function based approach for electronic structure calculation . . . 29
  - 2.1.3 Density based approach: Density Functional Theory . . . 30
    - 2.1.3.1 Exchange- Correlation Functional . . . 34
- 2.2 Different methods for electronic band structure calculations . . . 36
  - 2.2.1 The Linear Muffin Tin orbital Method . . . 36
  - 2.2.2 N^{th} Order Muffin Tin Orbital (NMTO)- a downfolding method . . . 38
  - 2.2.3 The Pseudopotential Method . . . 41
  - 2.2.4 The Linearized Augmented Plane Wave + local orbital method . . . 42
  - 2.2.5 The Projector-Augmented-Wave Formalism . . . 44
- 2.3 Other advanced supporting techniques . . . 45
  - 2.3.1 Ab-initio Molecular Dynamics . . . 45
    - 2.3.1.1 Ehrenfest Molecular Dynamics . . . 46
    - 2.3.1.2 Born-Oppenheimer Molecular Dynamics . . . 47
    - 2.3.1.3 Car-Parrinello Molecular Dynamics . . . 47
  - 2.3.2 AIMD followed in this study . . . 48
  - 2.3.3 Dynamical Mean Field Theory . . . 49

3 First principle study of 4-*d* perovskite ruthenates* 57
3.1 Back ground and Motivation of the present study . . . 57
3.2 Results and Discussions . . . 59
3.2.1 Crystal Structural . . . 59
3.2.2 Electronic Structure . . . 61
3.2.3 Structural Optimization . . . 63
3.2.4 Experimental Evidence . . . 65
3.2.5 Electron-electron correlation effect in Sr/$CaRuO_3$ . . . 67
3.2.6 Model Hamiltonian for LDA+DMFT calculation . . . 67
3.3 Conclusions . . . 71

4 Pressure driven changes in electronic structure of $BiCoO_3$ * 75
4.1 Back ground and Motivation of the present study . . . 75
4.2 Results and Discussions . . . 77
4.2.1 Crystal Structure at ambient pressure and high pressure . . . 77
4.2.2 Electronic Structure of $BiCo_3$ in AP and HP phase . . . 78
4.2.3 Bi-O covalency and distortion . . . 84
4.3 Conclusion . . . 87

5 Ab-initio study of low dimensional quantum spin systems Sr_3NiPtO_6, Sr_3CuPtO_6 and Sr_3NiIrO_6 * 91
5.1 Background and motivation of the present work . . . 91
5.2 Results and Discussions . . . 93
5.2.1 Crystal Structure . . . 93
5.2.2 Electronic Structure . . . 96
5.2.3 Magnetic Property . . . 98
5.2.4 Low Energy Hamiltonians and Hopping Interactions . . . 99
5.2.5 Magnetic Interaction . . . 106
5.2.6 Spin-Orbit Interaction . . . 108
5.3 Conclusion . . . 110

6 Tuning of magnetic ground state of spin $\frac{1}{2}$ square lattice compound $Zn_2VO(PO_4)_2$ through chemical substitution* 115
6.1 Background and Motivation of the present study . . . 115
6.2 Results and Discussions . . . 116
6.2.1 Crystal Structure . . . 116
6.2.2 Electronic Structure of Pristine Compound . . . 119
6.2.3 Electronic Structure of Ti substituted Compound . . . 124
6.2.4 Calculation of Magnetic Properties . . . 125
6.3 Conclusion . . . 128

7 First principles Study of Organic-inorganic Hybrid Framework Compound, $Mn(C_4H_4O_4)$* 133
7.1 Introduction and motivation of the present work . . . 133
7.2 Results and Discussions . . . 135
7.2.1 Crystal Structure . . . 135
7.2.2 Electronic Structure . . . 137
7.2.3 Low Energy Hamiltonian and Hopping Interaction . . . 140
7.2.4 Magnetic Exchange Interaction . . . 146

7.3 Conclusion 147

8 Pressure and Temperature Driven Spin-switching in Metal-organic Coordination Polymers from ab initio Calculations* **151**
8.1 Introduction and motivation of the present work 151
8.2 Calculation details 153
8.3 Results and Discussion 153
8.3.1 Crystal Structure 153
8.3.2 Structural optimization: Effect of hydrostatic pressure 154
8.3.3 Temperature effect and Ab-initio molecular dynamics (AIMD) results 158
8.3.4 Combined Pressure-Temperature route 160
8.3.5 Mn substitution 161
8.4 Conclusion 163

9 Summary and Outlook **167**
9.1 Summary 167
9.2 Scope for future work: 171

List of Figures

1.1 Conventional Cubic perovskite. Green, blue, red balls represents A, B and O atom respectively. . . . 3

1.2 $GdFeO_3$ type distorted perovskite structure . . . 4

1.3 Example of perovskite compounds showing variety of magnetic states. Reproduced from Ref. [16] . . . 7

1.4 Schematic representation of dimer spin model . . . 11

1.5 Schematic representation of alternating chain spin model . . . 12

1.6 Left panel shows the classification of hybrid system according to connectivity as proposed by Rao and Cheetham[47]. Right panel shows example of different hybrids belonging to different class according to connectivity. Reproduced from Ref. [47] . . . 14

2.1 Schematic figure of actual crystal potential and the approximated potential used in LMTO formalism. . . . 37

2.2 Construction of Kink partial wave . . . 39

2.3 N^{th} order approximation to the energy dependence of the partial wave . . . 39

2.4 Construction of pseudo potential and pseudo wavefuction (red lines) out of full coulomb potential. Figure adapter from web:*http://en.wikipedia.org/wiki/Pseudopotential* . . . 42

2.5 Schematic representation of: full many body lattice problem is mapped onto single impurity problem attached with the self consistent bath. . . . 50

2.6 Schematic flow chart of self consistent cycle of DMFT. . . . 51

3.1 Crystal structure of $SrRuO_3$ forming in perovskite structure. (a) Cubic phase, (b) tetragonal phase and (c) orthorombic phase. RuO_6 (blue ball) units are shown by shaded octahedra. Sr (green ball) atoms sit in the hollow formed by corner-shared RuO_6 units. The oxygen atoms at the apical positions of the RuO_6 octahedra are labeled as O1 (red ball) and those at the plane are labeled as O2 (orange ball). 59

3.2 Representative figure of orthorhombic distortion, namely $GdFeO_3$ type distortion, characterized by tilting and rotation of RuO_6 (shaded polyhedra) octahedral unit. Color conventions are same as that of previous figure. 60

3.3 LDA density of states of $SrRuO_3$ (upper panel) and $CaRuO_3$ (lower panel). The DOS projected onto O-*p*, Ru-*d* and Sr/Ca-*d* are shown with cyan, black and shaded lines. For CRO this leads to a nonmagnetic solution with identical DOS between spin-up and spin-down channels. 62

3.4 Wannier functions of the O-*2p* NMTO's calculated for optimized geometries with magnetization off (left panel) and magnetization on (right panel). The orbital shapes (constant amplitude surfaces) with lobes of opposite signs are labeled by red and blue colors respectively. 65

3.5 Temperature dependence of the bond lengths and corresponding Debye-Waller factors for the structural units around (A) Ru sites; (B) Sr site. 66

3.6 Effective Wannier functions corresponding to Ru-d_{xy} (left) and Ru-$dx^2 - y^2$ (right) for $SrRuO_3$. Plotted are the orbital shapes (constant-amplitude surfaces) with lobes of opposite signs colored black and white. 68

3.7 (a) Mass enhancement factor obtained within the LDA+DMFT calculations for $SrRuO_3$ and $CaRuO_3$. (a) FM moment of SRO and CRO plotted as a function of strength of electron-electron correlation, U. Panel (b) also shows the unscreened local moments for SRO and CRO. 69

3.8 LDA+DMFT spectral functions of (a) SRO and (c) CRO in comparison with LDA DOS. Only one of the spin channels is plotted for CRO since there is no net magnetic moment. (b) The spin-integrated LDA+DMFT spectral function and LDA DOS of SRO in comparison with photoemission data from Ref. [18]. 70

3.9 Intensity plot of the k-resolved spectral function A(k,ω) calculated within the LDA+DMFT formalism. The LDA band structure, shown with dots, has been superimposed for comparison. 70

3.10 The temperature evolution of the mass enhancement factors for SRO and CRO. 71

4.1 (a) Pressure dependence of the resistivity at 300 K and (b)temperature dependence of the resistivity at 6 GPa of $BiCoO_3$. Figures are reproduced from Ref. [10] 76

4.2 Crystal structure of $BiCoO_3$ in AP phase (left panels) and in HP phase (right panels). The large sized (green color) and medium sized (blue color) balls represent Bi and Co atoms respectively. The red and yellow colored small balls represent the O1 and O2 oxygens respectively. The local oxygen environment around Co atom is indicated with shaded polyhedra. The bottom panels show the local oxygen environment around the isolated Bi atoms. 78

4.3 Non spin-polarized density of states computed for $BiCoO_3$ at AP (left panels) and at HP (right panels). DOS are projected on to Bi (top panels), Co-*d* (middle panels) and O-*p* (bottom panels) states. The black and cyan colored lines in the top panels represent projections on to Bi *s* and Bi *p* states respectively. The black and brown colored lines in the bottom panels represent projections on to O1 and O2 states respectively. The insets in the middle panels represent partial DOS projected on to different *d* characters of Co. The zero of the energy, marked by a dashed vertical line, is set at E_F. 79

4.4 Spin-polarized density of states of $BiCoO_3$ at AP, computed considering the ferromagnetic spin alignment of Co (left panels) and C-type antiferromagnetic spin alignment of Co (right panels). DOS are projected on to Bi (top panels), Co-*d* (middle panels) and O-*p* (bottom panels) states. The black and cyan colored lines in the top panels represent projections on to Bi-*s* and Bi-*p* states respectively. The black and brown colored lines in the bottom panels represent projections on to O1 and O2 states respectively. The inset in the left, middle panel represent the energy level splitting of different *d* levels of Co. 80

4.5 Spin arrangements of C type antiferromagnetic configuration of Co site. Color conventions are same as Fig. 4.2 81

4.6 Spin-polarized density of states, projected on to Bi (top, left panel), Co-*d* (middle, left panel) and O-*p* (bottom, left panel), and band structure of $BiCoO_3$ at HP (right panel). The color convention for the DOS plot is same as in Figs. (4.3) and (4.4). The inset in the left, middle panel represent the energy level splitting of different *d* levels of Co. The band structure plot shows opening of an indirect gap of about 0.06 eV between Γ point and the Y point. 82

4.7 Plot of the effective O-*2p* Wannier functions for $BiCoO_3$ at AP, placed within the unit cell formed by Bi atoms at the corners and CoO_5 pyramid at the center. The left panel and right panels show one of the O1 and O2 *p* Wannier functions, respectively. Constant amplitude surfaces are shown with lobes of opposite signs colored with cyan and magenta. The central parts of the Wannier functions are shaped according to O1 p_y (left panel)and O2 p_z (right panel) while the tails extending to Co and Bi are shaped according to Co-*d* and Bi degrees of freedom. The pdσ bonds with Co and the covalency with Bi lone pair are visible. 84

4.8 Same as in Fig. 4.7, but for $BiCoO_3$ at HP. The Wannier functions are placed within the unit cell formed by the Bi atoms at the corners and CoO_6 octahedra at the center. . 86

4.9 Crystal orbital Hamiltonian populations (COHPs) between Bi and O (top panels), that between Co and O (bottom panels) in AP (left panels) and HP (right panels) phases of $BiCoO_3$. The black and cyan colored lines represent COHP defined for O1 and O2 respectively. The Bi-O COHP's are scaled to 4 nearest Bi-O1 interactions and Bi-O2 interactions, and Co-O COHPs are scaled to one (two) nearest Co-O1 interactions for AP (HP) phases, and four nearest Co-O2 interactions. Zero of the energy is set at E_F. . 86

5.1 Left Panel: Crystal structure of $A_3BB'O_6$ compounds, showing the chains running along the vertical direction. Right Panel: Hexagonal packing of chains viewed along the chain direction. The blue and grey colored balls denote B′ and B atoms, while red colored, small balls denote the shared oxygen atoms. A atoms, sitting in the hollows in between the chains are indicated as green colored balls. 93

5.2 Comparison of $BB'O_6^{-6}$ chains in Sr_3NiPtO_6 and Sr_3NiIrO_6 compounds (left panel) and in Sr_3CuPtO_6 compound (right panel). The color convention is same as in Fig. (5.1). 96

5.3 Non-spin polarized DOS calculated within GGA. B′-*d* states, B-*d* states, Sr-*s* and O-*p* states are presented by solid black lines, cyan lines, broken black lines and filled brown lines respectively. The zero of the energy is set at E_f. From top to bottom, the three panels correspond to plots for Sr_3NiPtO_6, Sr_3CuPtO_6 and Sr_3NiIrO_6 compounds respectively. 97

5.4 Non-spin polarized band-structure calculated within GGA. The dominant orbital characters for the bands are indicated. Zero of the energy is set at E_f. From left to right, the three panels correspond to plots for Sr_3NiPtO_6, Sr_3CuPtO_6 and Sr_3NiIrO_6 respectively. 98

5.5 The energy levels of B and B′ *d* levels in eV unit and their occupancies. From top to bottom, the three panels correspond to plots for Sr_3NiPtO_6, Sr_3CuPtO_6 and Sr_3NiIrO_6 respectively. 102

5.6 Bands obtained with downfolded basis (solid lines) compared to full DFT band structure (dashed lines). The energy points, marked as E_0 and E_1 in each panel, denote the energy points used in NMTO calculation. From left to right, the three panels correspond to plots for Sr_3NiPtO_6, Sr_3CuPtO_6 and Sr_3NiIrO_6 respectively. 102

5.7 Panels (a) and (b): Ni-Ni hopping interaction paths, t_n in Sr_3NiPtO_6. Panels (a) and (b) show perspectives showing the chains and that viewed along the chain direction, showing the hexagonal packing. The color convention of atoms is same as in Fig. (5.1). 103

5.8 Cu-Cu interaction paths, t_n in Sr_3CuPtO_6. The color convention of atoms is same as in Fig. (5.1). 103

5.9 Ni-Ni, Ni-Ir and Ir-Ir interaction paths, t_n in Sr_3NiIrO_6. The color convention of atoms is same as in Fig. (5.1). 104

5.10 Effective orbitals corresponding to the downfolded d_{xz} NMTOs, placed at two Ni sites situated in a given chain. An equivalent super-exchange path exists, created by overlap of two Ni downfolded d_{yz} NMTOs. Lobes of orbitals placed at different sites are colored differently. Lobe colored black (white) at one site represents the same sign as that colored magenta (cyan) at other neighboring site. 105

5.11 Effective orbitals corresponding to the downfolded d_{xz} NMTOs, placed at two Cu sites situated in a given chain. An equivalent super-exchange path exists, created by overlap of two Cu downfolded d_{yz} NMTOs. Lobes of orbitals placed at different sites are colored differently. Lobe colored black (white) at one site represents the same sign as that colored magenta (cyan) at other neighboring site. 105

5.12 Overlap of effective orbital corresponding to the downfolded Ni-d_{xz} and Ir-$t_{2g}^{(3)}$ NMTOs placed at neighboring sites within a chain. Other intra-chain super-exchange paths involve overlap of Ni-d_{yz} with Ir-$t_{2g}^{(3)}$ and Ni-d_{xz}/d_{yz} with Ni-d_{xz}/d_{yz}. Lobes of orbitals placed at different sites are colored differently. Lobe colored black (white) at one site represents the same sign as that colored magenta (cyan) at other neighboring site. . . . 106

6.1 (a)-(c)VO_5, ZnO_5 and PO_4 structural units. The larger ball represents either V or Zn or P while the smaller balls represent O. Various in-equivalent O atoms have been marked. (d) The projection of the structure in *ab* plane, showing the square planar arrangement of VO_5 pyramids. (e) The three dimensional connected structure. 118

6.2 The crystal structure of $\frac{1}{4}$ Ti substituted $Zn_2VO(PO_4)_2$. 119

6.3 Non spin-polarized density of states of $Zn_2VO(PO_4)_2$ as obtained in GGA calculation. The zero of the energy is set at GGA Fermi energy. The black-solid line, cyan solid line and the shaded area represent the density of states projected on to V-*d*, O-*p* and P-*p* respectively. The upper inset shows the energy level positions of V-*d* level as obtained in NMTO downfolding calculation. The lower inset shows the zoomed plot showing the contribution of O-*p* and P-*p* states to the V-d_{xy} derived states that cross the Fermi energy. 121

6.4 (a) The band structure of $Zn_2VO(PO_4)_2$ plotted along the high symmetry points of the tetragonal Brillouin zone. The dominant orbital characters of the bands have been marked. (b) The downfolded V-d_{xy} band (fat solid line) in comparison to full band structure (dashed line). The energy points indicate the energies about which the expansion has been made in NMTO downfolding calculation. (c) The overlap of V-d_{xy} Wannier functions placed at two NN, V sites in *ab* plane. Shown are the constant value surfaces with positive and negative lobes colored differently. 122

6.5 The V only sublattice of $Zn_2VO(PO_4)_2$. Shown are the dominant hoppings, t_1, t_2 and t_c 123

6.6 Upper panels: Comparison of the band structure of $Zn_2VO(PO_4)_2$ (left panel) and $Zn_8TiV_3O_4(PO_4)_8$ (right panel) plotted along the high symmetry points of the supercell. Lower panels: The density of states of $Zn_2VO(PO_4)_2$ (left panel) and $Zn_8TiV_3O_4(PO_4)_8$ (right panel). The V-*d* and Ti-*d* (applicable for the right panel) projected states are shown as solid and dashed lines. 124

6.7 The spin models corresponding to $Zn_2VO(PO_4)_2$ (left panel) and $Zn_8TiV_3O_4(PO_4)_8$ (right panel) compounds. The thick solid, thin solid and dashed lines represent strongest J_1 (J_1') and weak J_2 (J_1'') and J_c (J_c') interactions for $Zn_2VO(PO_4)_2$ ($Zn_8TiV_3O_4(PO_4)_8$) compound. The spins corresponding to inequivalent V ions in case of the substituted $Zn_8TiV_3O_4(PO_4)_8$ compound has been marked. 126

6.8 Upper panel: Calculated magnetic susceptibility plotted as a function of temperature for the pristine (black lines) and Ti-substituted (grey lines) compounds. The magnetic susceptibility for the pristine compound has been computed in absence (dashed line) and in presence of applied magnetic field of 10000 Oe (solid line). The latter has been compared with the experimentally measured data, [14] shown as open circles. Lower panel: Magnetization plotted as a function of temperature for the pristine (black lines) and Ti-substituted (grey lines) compounds for two different values of the magnetic field, H = 5000 Oe (solid line) and H= 1560 Oe (dashed line). 127

7.1 (a) Heat-capacity measurements for $MnC_4H_4O_4$ and the Fisher heat capacity determined using magnetic-susceptibility data indicating the two antiferromagnetic phase transitions at approximately 6 K and 10 K. Taken form Ref. [12]. (b) and (c) The Rietveld fit to the 8 K and 4.2 K neutron pattern respectively. The inset plot indicates the observed reflections caused by the magnetic ordering of the edge-sharing layer and corner sharing layer respectively. Figures are reproduced form Ref. [13]. 134

7.2 (a) The layer of edge sharing $Mn1O_6$ octahedra forming the chain like structure. (b) The layer of corner sharing $Mn2O_6$ octahedra forming connected 2-D geometry. (c) The alternate stacking of the edge shared and the corner shared MnO_6 layers connected through succinate ligands. The magenta colored octahedra belongs to the edge shared layer and the grey colored octahedra belongs to the corner shared layer. 135

7.3 (a) Local environment of the edge shared $Mn1O_6$ octahedra, (b) Local environment of the corner shared $Mn2O_6$ octahedra. The various Mn-O bond lengths as well as the edge shared Mn-O-Mn bond angle and corner shared Mn- O-Mn bond angle have been marked. 136

7.4 GGA non spinpolarized density of states of Mn succinate. The top panel shows the total density of states while the middle and bottom panels show the density of states projected onto Mn1-*d* and Mn-2-*d* characters respectively.The insets in the middle and bottom panels show the C-*p* projected states (left insets) and O-*p* projected states (right insets) marked as shaded regions in green/red in comparison to Mn-*d* projected states in solid lines. 140

7.5 Mn-*d* orbital projected GGA non spin polarized band structure. Different band characters are marker in the figure. 141

7.6 The positions of *d* energy levels at Mn1 and Mn2 sites obtained from NMTO downfolding calculation. 142

7.7 Spin polarized GGA density of states. Upper panel for Mn1 and lower panel for Mn2. . 143

7.8 Dominant Mn-Mn hopping interactions. Left panel: Mn1-Mn1 intra-chain interaction, t_1 and inter-chain interaction, t_2, Right panel: Mn2-Mn2 interaction, t_3. 145

7.9 (a) Overlap of downfolded d_{xy} and $d_{x^2-y^2}$ NMTOs, placed at two Mn1 sites corresponding to the intra-chain interaction, t_1. (b) Overlap of downfolded d_{yz} NMTOs, placed at two Mn1 sites corresponding to the inter-chain interaction, t_2. (c) Overlap of downfolded d_{xz} and $d_{x^2-y^2}$ NMTOs, placed at two Mn2 sites corresponding to the t_3 interaction. Lobes of the orbitals placed at different sites are colored differently. Plotted are the orbital shapes (constant amplitude surfaces) with the lobes of opposite signs colored black (magenta) and white (cyan) at 1^{st} (2^{nd}) Mn site. 145

8.1 light-induced spin-crossover phenomena. a) Magnetization vs. temperature plot at 100 Oe. Light irradiation induces a spontaneous magnetization with curie temperature 2 K. b) Magnetic hysteresis curves at 2 K. Light irradiation, opens up a hysteresis loop with a coercive field of 240 Oe. Circles denote measurements before and after irradiation with 473 nm light. Figures reproduced from Ref. [10] 152

8.2 Left panel shows the crystal structure of the system in a tetragonal unit cell. Fe , Nb, N, C, O and H atoms are represented by magenta, yellow, blue, brown, red and pink color balls respectively. Right panel highlights the environment around Fe and Nb sites. . . . 154

8.3 Computed magnetic moment at the Fe site plotted *vs* the unit cell volume of the Fe-Nb complex. The hydrostatic pressures corresponding to selected volumes are marked in the upper ordinate. The t_{2g} and e_g orbital occupations of Fe in HS, IS and LS states are shown schematically. 155

8.4 Computed magnetic moment at the Fe site plotted as a function of the unit cell volume of the Fe-Nb complex. The moment *vs* volume is the same as Fig. (8.3), but here plotted for two different paths. The data points in blue denote the path following a decreasing volume, starting from the HS state and the data points in red) denote the path following an increasing volume, starting from the LS state. Both HS $\rightarrow$ IS and IS $\rightarrow$ LS transitions exhibit interesting hysteresis effects. 158

8.5 Density of states projected onto spin-polarized Fe-*d* (black, solid), Nb-*d* (cyan, dashed), N-*p* (green, solid) and C-*p* (shaded area) states, for HS, IS, and LS configurations (top to bottom panel) of the Fe-Nb SCO compound. The zero energy is set at the Fermi energy (E_F). The upper and lower subpanels in each panel, correspond to up and down spin channels, respectively. 159

8.6 Evolution of the average Fe-N bond length as a function of temperature, starting from the low temperature IS state at 2.94% reduced volume to the high temperature HS-2 state. The insets show the computed probability distributions P of the average bond lengths at $T = 20$ K and $T = 275$ K. 160

8.7 Magnetization density plots for the HS-1 (upper panel) and HS-2 (lower panel) states (isosurface value set at 0.025/Å^3). The magenta and yellow color indicates positive and negative values of the magnetization densities, respectively. Also shown are the structural comparison of the super-exchange Fe-N-C-Nb path in HS-1 and HS-2, together with a zoomed plot of the magnetization density along the super-exchange path. 161

8.8 Schematic representation of the temperature-pressure induced spin-state transitions in the Fe-Nb framework. 162

8.9 Magnetic moment at the Mn site plotted against the unit-cell volume of the Mn-Nb complex. The magnetization density plots in the insets illustrate the pressure-induced switching from ferrimagnetic alignment between Mn^{2+} (S=$\frac{5}{2}$) and Nb^{4+} (S=$\frac{1}{2}$) to ferromagnetic alignment between Mn^{2+} (S=$\frac{1}{2}$) and Nb^{4+} (S=$\frac{1}{2}$) along the superexchange path. 163

List of Tables

1.1 Example of perovskites belonging to different crystallographic structures. * denote non-oxide perovskite materials. 4

1.2 Lists of perovskites of different physical properties 6

1.3 Few example of perovskites with their novel physical features 6

1.4 Lists of some mulfiferroic perovskite 9

1.5 Variety of magnetic properties of different organic-inorganic hybrids. Reproduced from Ref. [47] 19

3.1 Selected bond lengths and bond angles for $SrRuO_3$ and $CaRuO_3$ 60

3.2 Magnetic moments at different sites for $SrRuO_3$ and $CaRuO_3$ from LDA calculations . 63

3.3 Relative changes in the distortion of Sr-O, Sr-Sr, and Ru-O bonds in absence and presence of magnetic ordering. 64

4.1 Magnetic Moments at Co, O1 and O2 sites for $BiCoO_3$ at AP, as obtained in spin-polarized GGA calculations in LMTO basis for FM and C-AFM spin arrangements. The entries within the bracket denote the numbers obtained in plane wave basis. 82

4.2 Total energies (in eV) per formula unit calculated for the discussed HP phases in literature, orthorhombic phase as predicted in the experimental study of Ref.[10], the cubic phase predicted in theoretical study in Ref.[7] and the tetragonal phase predicted in the theoretical study in Ref.[9]. 83

5.1 Energy-minimized structural parameters of Sr_3NiPtO_6, Sr_3CuPtO_6 and Sr_3NiIrO_6. Lattice constants have been kept fixed at the experimental values [12, 24, 16]. 94

5.2 Selected bond lengths and bond angles for the optimized crystal structure of Sr_3NiPtO_6, Sr_3CuPtO_6 and Sr_3NiIrO_6. 95

5.3 Magnetic Moments at B, B′ and O sites, as obtained in spin-polarized GGA calculations. 99

5.4 List of dominant hopping interactions for the three compounds. In case of Sr_3NiPtO_6, hoppings are defined between Ni-d_{xz}/d_{yz} and Ni-d_{xz}/d_{yz}. In case of Sr_3CuPtO_6, hoppings are defined between Cu-d_{xz} and Cu-d_{xz}. 100

5.5 List of dominant hopping interactions for Sr_3NiIrO_6. Hoppings are defined between Ni-d_{xz}/d_{yz} and Ir-$t_{2g}^{(3)}$ (t_1)as well as between Ni-d_{xz}/d_{yz} and Ni-d_{xz}/d_{yz} (t_5), and between Ir-$t_{2g}^{(3)}$ and Ir-$t_{2g}^{(3)}$ (t_2,t_3, t_4). 101

5.6 Spin and orbital moments in μ_B as obtained in GGA+SO calculations for the three compounds.[31] The magnetic anisotropy energies are also listed. 108

6.1 Various atomic positions of the pristine $Zn_2VO(PO_4)_2$ and Ti-substituted $Zn_8TiV_3O_4(PO_4)_8$ compounds. 117

6.2 The TM-O bond lengths and O-TM-O bond angles in pristine ($Zn_2VO(PO_4)_2$) and Ti-substituted ($Zn_8TiV_3O_4(PO_4)_8$) compounds. 120

6.3 Dominant hopping interactions for the pristine and Ti-substituted compounds. Hopping interactions having magnitude less than 1 meV have been neglected. 125

7.1 The theoretically optimized atomic positions compared to the experimentally determined data. During the optimization the lattice constants are fixed at experimentally measured values, a=30.28 Å, b=4.86 Å, c=6.29 Å, β=99.50^o. 138

7.2 Bond lengths(Å) and Bond angles(^{o}) for the theoretically optimized structure compared to the experimentally determined structure. 139

7.3 Magnetic Moments (in μ_B) at different sites as obtained in spin-polarized GGA calculation. 142

7.4 List of dominant Hopping Interactions for $Mn(C_4H_4O_4)$. 144

8.1 The optimized theoretical crystal structure for ambient pressure, and for 2.94% and 7.58% reduced volumes. During the optimization the lattice parameters are kept fixed at the mentioned values. The space group is in all three cases $I4_1/a$. The atomic coordinates are given in IORIGIN=1 setting. 156

Chapter 1

Introduction

1.1 Introduction to Novel Materials

Material Science is an interdisciplinary subject of common interest to both purely scientific community as well as to the technologist. Materials are fundamental for development of civilization. The materials are important in the history of human evolution. The prehistoric ages are named after different materials like; *Stone age*, *Bronze age* and *Iron age*. Therefore material science research has become unavoidable to fulfill the growing demands of modern society. Recent time has seen various classic discoveries which are mainly material dependent. Therefore design and modeling of new materials for new improved functionalities are essential for technological progress. For that purpose demand of *'novel materials'* with novel properties are increasing.
Novel Materials are functional materials which are novel in their properties which are tunable. The novel materials may be classified in the following way:

a) Materials whose existing properties are improved to make the properties more accessible. The family of high T_c cuprate materials fall in this category.

b) Materials that are not an extension or evolution of families or combination of materials, but are distinct materials in their own right. The example of carbon nano tube and fullerence fall in this category.

c) Composite materials where combination of two or more components lead to unexpected or unconventional properties. The hybrid systems of organic and inorganic component fall in this class.
With the advent of computational material science these materials can now be understood at the microscopic level. Such microscopic understanding is required for optimization of known materials, with the possibility of prediction of new materials. One of the major component of computational material science, is to study the electronic structure. Electrons at the microscopic level govern the properties like, magnetic, optical, transport etc.

In the present thesis we used *density functional theory* based *first principles methods* (will be discussed in the next chapter) for investigation of electronic structure of materials. The advantages of first principle method is that, the only input is the crystal structure with proper atomic information. These are very reliable, fast, accurate and parameter free approaches. These can capture the material dependent chemistry accurately. Using such methods one can handle almost any type of materials, starting from crystalline to amorphous and disordered materials, clusters, organics, inorganics, composites, molecules, biological systems, nano systems etc. In the present thesis we have studied three broad category of materials namely; i) perovskite based transition metal oxides, ii) low dimensional quantum spin systems, and iii) organic-inorganic hybrid materials. In the following sections we will discuss these three classes in detail.

1.2 Perovskite based Transition Metal Oxides

Metal oxide perovskites constitute one of the largest class of materials exhibiting various novel features. First perovskite based mineral $CaTiO_3$ was discovered in 1839 in Ural mountain by geologist Guastav Rose and the name given in the honor of famous Russian mineralogist Count Lev Alexevich Perovski [1]. The general formula of any perovskite is ABC_3, where 'B' atom is surrounded by 'C' in a 6 coordinated environment whereas 'A' atom is surrounded in a 12 coordinated environment by 'C' atom. Perovskite materials $MgSiO_3$ and $FeSiO_3$ are the most abundant compound in the earth's crust [3].

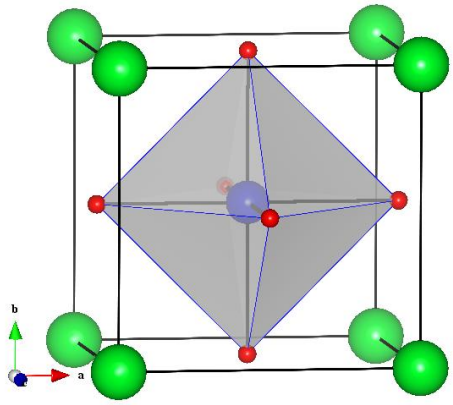

Figure 1.1 Conventional Cubic perovskite. Green, blue, red balls represents A, B and O atom respectively.

1.2.1 Structure

The general formula of perovskite based transition metal oxides is ABO_3, where 'A' is a rare earth or alkaline earth element and 'B' is a transition metal. Generally the structure consists of an array of corner shared BO_6 octahedral unit with a large 'A' cation sitting at the void spaces in between the octaheda units. The structure of these perovskite oxides are mainly derived from cubic structure as shown in Fig. (1.1). But many compounds in low temperature often exist with lower symmetry structures such as tetragonal, orthorhombic or hexagonal structure. Table. (1.1) show lists of different perovskites belonging to different structures.

Ideally the corner shared ∠B-O-B is 180^o, but due to structural distortion this angle may deviate from 180^o as well as the bond lengths may become unequal. Primarily this distortion arises due to mismatch between 'A' site and 'B' site ionic radii. Qualitatively Goldschmidt [2] proposed a quantity, called *tolerance factor* ($t = \frac{r_A + r_O}{\sqrt{2}(r_B + r_O)}$) describing the stability and distortion in the perovskite type structure, where r_A, r_B and r_O are the ionic radii of A, B and O atom respectively. When the radius of 'A' atom is small the structure become more distorted leading to tetragonal or orthorhombic distortion, i.e $GdFeO_3$ type distortion, where the individual BO_6 corner shared octahedra are rotated and tilted with respect to the z axis, as shown in Fig. 1.2. In perovskite compound 't' lies approximately between

Table 1.1 Example of perovskites belonging to different crystallographic structures. * denote non-oxide perovskite materials.

Cubic	Tetragonal	Orthorhombic	Hexagonal
$KTiO_3$	$BiAlO_3$	$GdFeO_3$	BaRuO3
$NaTiO_3$	$SrRuO_3$	$SrRuO_3$	Li_xWO3
$NaNbO_3$	$PbSnO_3$	$CaRuO_3$	Cs_xWO3
$BaMnO_3$	$BaTiO_3$	$YFeO_3$	Rb_xWO3
$SrRuO_3$	$PdTiO_3$	$NdGaO_3$	K_xWO3
$BaZrO_3$	*$TlMncl_3$	$NaMgF_3$	LaAlO3
$SrTiO_3$			LaNiO3
$CaRuO_3$			BiFeO3
$BaRuO_3$			KNbiO3
*$KMnF_3$			
*$KFeF_3$			

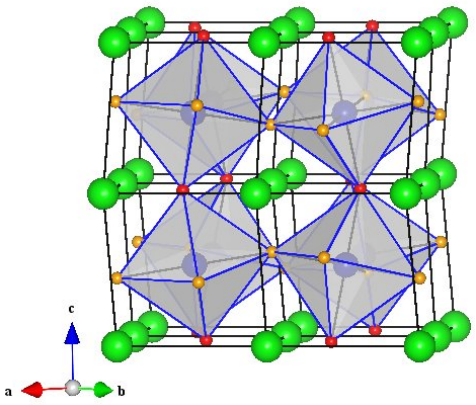

Figure 1.2 $GdFeO_3$ type distorted perovskite structure

0.8 to 1.1. The ABO_3 structure with $t>1$, forms hexagonal polytypes [4] such as $BaRuO_3$ [5] in normal ambient condition. As the t value decreases the structure goes from cubic to tetragonal to orthorhombic structure due to increase of distortion. The symmetry of the perovskite structure depends on the types of chemical species in the position of 'A' and 'B'. For example, $AMnO_3$ crystallizes in a conventional perovskite structure where 'A' is limited to La/Ce/Dy. But in the case of A=Ho-Lu/Y it crystallizes with a structure where Mn and 'A' are coordinated by 5 and 7 oxygen respectively [6]. Also there are Ge based perovskite are reported where it deviates from ideal 6 coordination [7].

Similarly out of the conventional perovskite structure many different variant structures have emerged which have perovskite like structure. As a whole this series is called Ruddelsden-Popper series with general formula $(ABO_3)_n.AO$ [8]. If one replaces 'B' site cation by another cation, say B', super structure systems are formed. Typical example of such super-structure is $Ba_3MTa_2O_9$, where M and Ta are distributed randomly in the octahedral positions (M= Fe, Co, Ni, Zn or Ca), whereas for M=Sr the hexagonal superstructure is obtained. Another class of super-structure exist where cation vacancy is located at 'A' site *i.e* ANb_3O_3 (A= La, Ce, Pr, Nb) and ATa_3O_9 (A= La, Ce, Pr, Nd, Sm, Dg, Dy, Ho, Y, Er). Another typical poly type of perovskite structure are *Brownmillerite* ($A_2B_2O_5$), which are the oxygen deficient type of perovskite where the oxygen vacancies are ordered. An extreme example is the combination of ordered 'B' site and oxygen defect case as seen in K_2NiF_4 structure. The structure consist of conventional perovskite unit $KNiF_3$ and rock salt unit KF.

The perovskite family, therefore, includes a huge number of different types of structures, and at the same time different elements of the periodic table, giving rise to wide variety of physical properties [9, 10, 11, 12].

1.2.2 Few interesting perovskites and their emergent physical properties

As mentioned perovskite oxides are extremely interesting because of enormous variety of rich physical phenomena they exhibit. The perovskite the elements 'A' and 'B' can exhibit different combinations of charge states, *e.g* (+1/+5), (+2/+4) and (+3/+3) giving rise to a wide spectrum of electronic and magnetic behavior. Table. (1.2) and (1.3) show some perovskite systems with their corresponding properties.

A. Magnetic and Electric properties : Magnetic properties of the transition metal based per-

Table 1.2 Lists of perovskites of different physical properties

Insulating	Metallic	Semi conductor	Magnetic	Superconductor
$NaTiO_3$	$LaTiO_3$	$LaRhO_3$	$PbCrO_3$	SrTiO3 (n type)
$SrRuO_3$	$NaWO_3$	$GdTiO_3$	$LaFeO_3$	Na_xWO3
$SrTiO_3$	$KMnO_3$	$CaCrO_3$	$LaCrO_3$	K_xWO3
$LiNbO_3$	$LaWO_3$	$PbCrO_3$	$CaMnO_3$	Rb_xWO3
$BaTiO_3$	$SrNbO_3$		$LaMnO_3$	Cs_xWO3
$KTaO_3$			$LaCoO_3$	Li_xWO3

Table 1.3 Few example of perovskites with their novel physical features

Properties	Compounds
Ferromagnetic	$BaTiO_3$, $PdTiO_3$
Piezoelectric	$Pb(Zr,Ti)O_3$, $(Ba,Na)TiO_3$
Electrical conductivity	$SrFeO_3$, $LaCoO_3$, $LaNiO_3$, $LaCrO_3$
superconductivity	$La_{0.1}Sr_{0.9}CuO_3$, SrTiO3(n type), $YBa_2Cu_3O_7$, $HgBa_2Ca_2Cu_2O_8$
Ion conductivity	$La(Ca)AlO_3$, CaTiO3, La(Sr)Ga(Mg)O3, BaZrO3, SrZrO3, BaCeO3
Magnetic property	$LaMnO_3$, $LaFeO_3$, La_2NiMnO_6
Catalytic property	$LaCoO_3$, $LaMnO_3$, $BaCuO_3$
Electrode	$La_{0.6}Sr_{0.4}CoO_3$, $La_{0.8}Ca_{0.2}MnO_3$

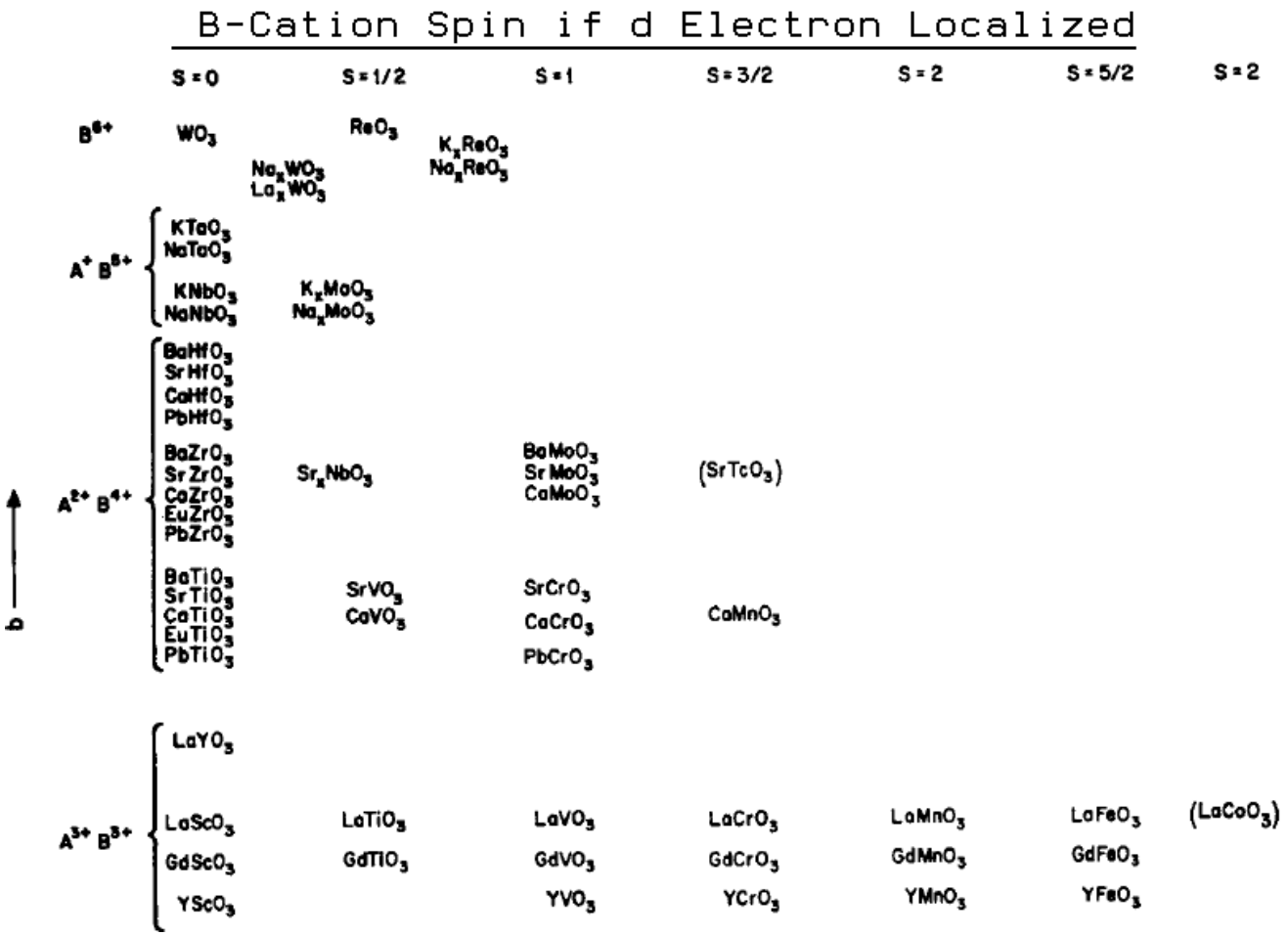

Figure 1.3 Example of perovskite compounds showing variety of magnetic states. Reproduced from Ref. [16]

ovskite are governed by the partially filled *d* electrons of 'B' atom. Electron-electron correlation effects in these systems are generally strong, i.e the coulomb repulsion energy is strong compared to the band width [13]. Many of them show metal insulator transition as a function of external perturbations like temperature, pressure or doping [14]. Typical examples are, $Ln_{1_x}Sr_xMO_3$ (Ln = La, Pr,Nd; M = V, Mn, Co) which show Mott metal- insulator transition with increase in x values [29]. Similarly $LaNi_{1-x}M_xO_3$ (M = Cr, Mn, Fe, or Co) compounds show metallic to insulator behavior above a critical value x. Generally the magnetism in these materials are described by the super-exchange mechanism [15], where the hopping and the super-exchange paths between the two transition metal 'B' sites are mediated by the intervening oxygen atoms. The distortions (tilting and rotation) in the BO_6 ocathe-

dra also play a very crucial role in the determination of magnetism. Fig. (1.3) shows spin states and magnetic behavior of some important perovskites [16]. In the Fig. (1.3) the compounds in first column (*i.e* S=0) are all insulators because the electronic configuration at 'B' cationic site is d^0, whereas most of the compounds in column two (*i.e* S=1/2) are metallic and shows Pauli paramagnetism. Only exception is $GdTiO_3$ which is a semiconductor with a ferromagnetic Curie temperature of 21 K. In the third column (S=1) of this chart first few compounds *i.e* $SrCrO_3$ and AMo03 (where A = Ca, Sr, Ba) are metallic and Pauli paramagnetic. Among the other compounds in this column, $CaCrO_3$ and $PbCrO_3$ are semiconductor with an antiferromagnetic ordering. The compounds in columns 4, 5, and 6 *i.e* S=$\frac{3}{2}$ - S=$\frac{5}{2}$ exhibit conventional antiferromagnetic insulating behavior. In the above chart $LaCoO_3$ arises twice, one in S=0 and next in S=2 because Co can exist in two different spin state configurations namely low spin and high-spin states. $SrFeO_3$ is placed in the same column on the assumption that Fe^{4+} ($3d^4$) is in the low-spin states. On the other hand in case of $CaFeO_3$, Fe^{4+} seems to undergo charge disproportionation to Fe^{3+} and Fe^{5+} below 290 K. There are some other oxides which show different kind of magnetic behavior, such as $LaNi_{1-x}Mn_xO3$, with Mn^{2+} which show spin-glass behavior [17]. Apart from the above mentioned systems there also exist some perovskite derived systems which show distinct features compared to the parent compound [20, 25]. For example, $LaNiO_3$ is metallic with Pauli paramagnetism whereas La_2NiO_4 exhibits two-dimensional antiferromagnetic ordering around 200 K and a semiconductor-metal transition around 600 K. Similarly while $LaCoO_3$ shows a spin-state transition of Co^{3+} and associated paramagnetism [28], La_2CoO_4 seems to exhibit antiferromagnetic ordering at fairly high temperatures [18]. La_2CuO_4 is a low-resistivity oxide with no magnetic moment at the Cu site but not metallic, whereas $LaCuO_3$ is a metal [26] $SrRuO_3$ is a ferromagnetic metal whereas Sr_2RuO_4 is a paramagnetic insulator [19, 14].

B. Dielectric Properties: Ferroelectricity, pizeoelectricity, electrostriction, pyroelectricity are some of very special properties that are exhibited by large number of perovskite materials. Most common ferroelectric perovskites are $BaTiO_3$, $PdZrO_3$ and $LiNbO_3$. These systems have been studied extensively in the last century [27]. The ferroelectric polar distortion arises due to the off-centric movement of 'B' site atom with respect to oxygen cage. There also exist some examples of anti-ferroelectric material as well such as $PbZrO_3$, $NaNbO_3$ etc [27].

Table 1.4 Lists of some mulfiferroic perovskite

Properties	Compounds
Ferroelectric-Ferroelastic	$Gd_2(MoO_4)_3$, $KNbO_3$
Ferroelectric-Ferromagnetic	$Bi_9Ti_3Fe_5O_{27}$, $BiMnO_3$
Ferroelectric-Antiferromagnetic	$YMnO_3$, $HoMnO_3$, $BiCoO_3$, $InMnO_3$
Antiferroelectric-Antiferromagnetic	$BiFeO_3$
Ferroelectric-Spiral magnetic	$TbMnO_3$
Ferroelectric-Semiconductor	$SrTiO_3$, $YMnO_3$

Apart from ferroelectric materials within these class of materials there are some compounds which are found to exhibit piezoelectric behavior, such as $Pb(Zr,Ti)O_3$, $(Bi,Na)TiO_3$ etc. These piezoelectric materials are used for relaxor application. Some commonly known relaxor are PZT ($Pb(Zn_{\frac{1}{3}}Nb_{\frac{2}{3}})O_{3-x}PbTiO_3$) and PMN ($Pb(Mg_{\frac{1}{3}}Nb_{\frac{2}{3}})O_{3-x}PbTiO_3$). Perovskites also exhibit multiferroic properties with co-existing ferromagnetic and ferroelectric order. In the Table. (1.4) show some examples of perovskites showing different multiferroic properties are enlisted.

1.3 Low Dimensional Quantum Spin System

Spin systems are important as they provide prototypical models of quantum magnetic insulators. They are conceptually simple, yet demonstrate surprisingly rich physics. Low dimensional systems, in 2D and especially in 1D, have been particularly attractive because their simplicity enables exact solution to be found, nevertheless they exhibit highly nontrivial features. The interest in low dimensional magnets developed into a field of its own because these materials provide a unique possibility to study ground and excited states of quantum models, possible new phases, phase transition and the interplay of thermal and quantum fluctuations. There are many cases in which one can find no exact solution and in these cases they can be used as a testing ground for approximate methods. These quantum systems thus provide a great variety of interesting and difficult challenges to the mathematician or physicist.

In early days this field enjoyed attention from theoretical point of view but after that it has been realized that one and two dimensional models of interest to theoretical physicist might also be relevant

for real materials which could be found in nature or synthesized by crystallographers. One of the classic example is the early neutron scattering experiment on $(CH_3)_4NMnCl_3$ (TMMC) [30]. While structurally these materials are three dimensional, but the directional nature of chemical bonds and magnetic interactions, reduces the effective dimensionality of the underlying spin system to less than three.

In contrast to ferromagnetic ground state, the ground state of the antiferromagnetic (AFM) Heisenberg model shows quantum fluctuation. Considering antiferromagnetic Heisenberg model, strict antiferro alignment of spins gain energy only from the Ising part (S^zS^z)of the Heisenberg interaction (the energy value is -JS^2, where J is coupling strength and S is spin operator). In order to get the true ground state, one need to let the spins fluctuate so that the system can gain energy also from spin flip (or x-y) term (the extra energy lowering is -JS). This can be measured by the ratio of the quantum correction to the classical z-z energy $\frac{-JS}{-JS^2} = \frac{1}{S}$ For two site case, quantum effect are of the order of 1/S. Going over to the lattice case it can be concluded that the relevant parameter is more likely $\sim \frac{1}{zS}$, where z is the coordination number. Therefore quantum fluctuations are more stronger for small spin and low dimensional system.

Here we highlight some of the important consequences of quantum fluctuations. Bethe [32] showed the quantum fluctuation prevent true long range AFM ordering for homogeneous 1D S=1/2 system. For 2D S=1/2 system, the Heisenberg model has a ground state with long range AF order only at 0 K. Neither system has a spin gap i.e there is no cost in energy to create excitation with S=1. The quantum fluctuations brings a dramatic effect in behavior of compounds of intermediate dimension between 1D and 2D i.e quasi 1D S=1/2 systems. These systems may have a finite energy gap between singlet ground state (S=0) and triplet excited state (S=1). The even leg ladder [31], alternating Heisenberg AFM chain [34], dimer system [35], spin-peirls system [36] show energy gap in their spin excitation spectrum. Halden [34] conjected that a simple 1D magnetic chain would have a spin gap for all integer spin, but would be gap less for half integer spins. An analogous situation has been found to exist in quasi 1D spin ladder configuration in which ladder with even legs would exhibit an energy gap , but with odd number of legs would not [37]. In the following we discuss in detail different possible spin systems.

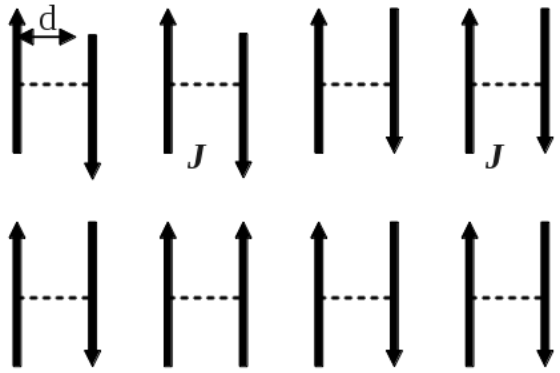

Figure 1.4 Schematic representation of dimer spin model

1.3.1 Different classes of quantum spin system

A) Spin Dimer System: Dimer system is one in which two sites are magnetically coupled and are magnetically isolated from rest of the sites. More complex systems can often be built up starting with dimers, especially if the inter-dimer coupling is weak compared to the intra-dimer coupling. A schematic diagram of spin dimer system is shown in Fig. (1.4). The Heisenberg Hamiltonian corresponding to antiferromagnetically coupled isotropic dimer is given by $H = J\mathbf{S}_1.\mathbf{S}_2$, where, J > 0 is the coupling strength and and $\mathbf{S_1}$ and $\mathbf{S_2}$ are the spins of the two coupled ions. With J > 0, the system has minimum energy when two spins are aligned in opposite directions. On the other hand the Hamiltonian corresponding to anisotropic dimer can be represented

$$H = J\left[S_1^z S_2^z + \frac{\alpha}{2}\left(S_1^+.S_2^- + S_1^-.S_2^+\right)\right]$$

Here again, J > 0 is the coupling strength and $\mathbf{S_1}$ and $\mathbf{S_2}$ are the spins of the two coupled ions, S^+ and S^- are the spin raising and lowering operator. α is the spin anisotropy, where α=1 is identical with the isotropic case presented in the $H = J\mathbf{S}_1.\mathbf{S}_2$. Example of dimer systems are $CaCuGe_2O_6$, organic vanadyl glycolate [38] etc.

B) Alternating Chain Model: Alternating chain is an infinite chain of dimers connected together, but the strength of connection between the dimers is not the same as the connection within the dimer. The intra-dimer exchange and inter-dimer exchange constants, J_1 and J_2 ($< J_1$) alternate along the chain. A schematic represent ion of an alternating Heisenberg antiferromagnetic chain is shown in the Fig. (1.5).

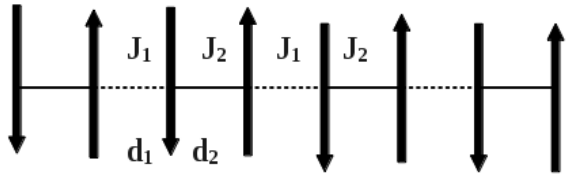

Figure 1.5 Schematic representation of alternating chain spin model

The system is represented by the Hamiltonian

$$H = \sum_i [J_1 \mathbf{S}_1(i).\mathbf{S}_2(i) + J_2 \mathbf{S}_2(i).\mathbf{S}_1(i+1)]$$

where 'i' is the position of a dimer. $J_1, J_2 > 0$ for AFM coupling. If $J_1 = J_2$, the system is a uniform AFM Heisenberg chain, the ground state of which has been solved exactly. While the uniform Heisenberg chain has no spin gap, the alternating chain compound shows spin gap [39, 40] the magnitude of which depends on the ratio $\frac{J_2}{J_1}$. Examples of alternating chain system is that of vanadyl pyrophosphate, $(VO)_2P_2O_7$ [41], spin $\frac{1}{2}$ penta fluorophenyl nitroxide (F_5PNN) [42].

C) Spin Ladder System: Both the magnetic systems, dimer and alternating chains, discussed above are one dimensional systems, while a ladder system is intermediate between a one and two dimensional system, called quasi 1-D system. To make the transition from the quasi long range order in a chain of AFM coupled S=$\frac{1}{2}$ spin to the true long range order that occurs in a plane, one can assemble chains to make ladders of increasing width. Therefore ladder consist of two or more spin chains coupled together in a fashion of ladder. The Hamiltonian for general spin ladder is given by

$$H = J_{\parallel} \sum_{i,j} \mathbf{S}_i.\mathbf{S}_j + J_{\perp} \sum_{i,j} \mathbf{S}_i.\mathbf{S}_j$$

where $J_{\parallel}$ is the exchange coupling along the direction of the spin chain (i.e. along the leg of the ladder), and $J_{\perp}$ is the exchange coupling between the chains(i.e. along the rung of the ladder). The interest of spin ladder systems was driven by the importance in understanding the mechanism of high T_C superconductor. It has been suggested that spin ladder may exhibits superconductivity under doping [31]. Physical realization of ladders like $SrCu_2O_3$ [33] corresponds to $J_{\parallel} = J_{\perp}$.

D) Spin-Peierls System : Spin-Peierls transition is an intrinsic lattice instability in spin $\frac{1}{2}$ AFM Heisenberg chains, the driving force being the magneto-elastic coupling between the one dimensional spin

structure and the three dimensional lattice vibrations [43]. Above the transition temperature T_{sp}, there is an uniform AFM next-neighbor exchange in each chain, below T_{sp} there is an elastic distortion resulting in dimerization, giving rise to two, unequal alternating exchange constants. The alternating chain exhibits an energy gap between the singlet ground state and lowest lying band of triplet excited states. The magnitude of the gap is related to the degree of dimerization and hence to the degree of lattice distortion. Thus the magnetic susceptibility χ(T) shows a knee at T_{sp}, with a rather abrupt fall of χ below T_{sp}, corresponding to the opening of the gap. Whereas the normal Peierls distortion occurs at a temperature of the order $k_B T_p \sim J \exp(-\frac{1}{\lambda})$, where λ is the electron-phonon coupling constant, the spin-peierls transition will occurs at $k_B T_{sp} \sim E_F \exp(-\frac{1}{\lambda})$, where λ is the exchange interaction between adjacent spins and E_F is the Fermi energy; since $J << E_F$, T_{sp} is always small in comparison with T_p. Example of such materials are mainly organic systems, e.g. MEM(TCNQ) [44], TTT-$CuS_4C_4(CF_3)_4$ [45], TTT-$AuS_4C_4(CF_3)_4$ [46].

1.4 Organic-Inorganic Hybrid Systems

Hybrid materials with extraordinary properties have become one of the frontier topic of research in material science. *Hybrid* materials are composite of different types of elements arranged in a non trivial way. Hybrid materials couple the best part of different materials world into a single system. Some of the applications of hybrid materials are catalytic activity, Storage, Gas-separation, Media device, Switch [48] etc.

The *organic-inorganic hybrid* systems are made out of inorganic and organic chemical species form a special sub general class within the general class of hybrid materials. Depending on the synthesis procedure these hybrid material can be formed in a dense system, porous system, isolated molecular system or extended network system. The present thesis deals with network type organic-inorganic hybrid system. Technically these network of organic-inorganic hybrid system is called *metal-organic framework* (MOF) system. MOF's defined as the compounds that contain inorganic metallic centres connected via organic ligands or functional groups and form a 3-D crystalline network [60]. In chemistry community and literature this class of materials are broadly called *coordination polymers* [49]. The interest on these hybrid systems starts increasing after 1990's when several functional molecular building block

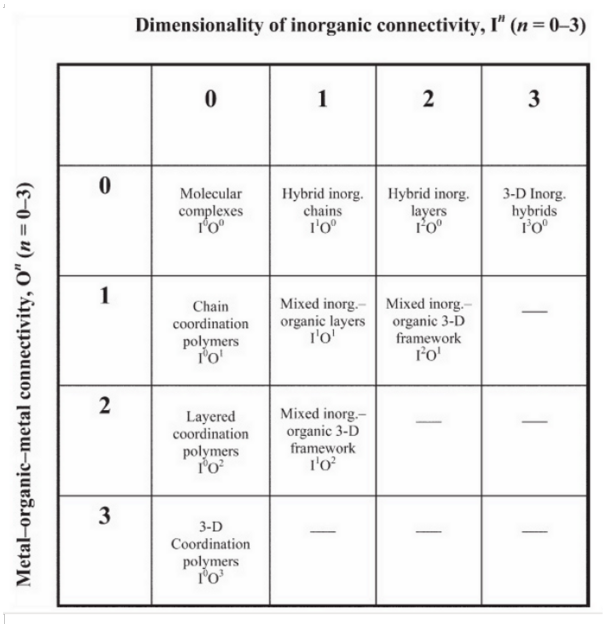

I^nO^m	Formula
I^0O^0	$[Mn(H_2O)(1,3\text{-CHDC})(1,10\text{-phen})]$
I^0O^1	$[Mn_3(1,3\text{-CHDC})_3(1,10\text{-phen})_2]\cdot 4H_2O$
I^0O^2	$[Cd(H_2O)_2(1,3\text{-CHDC})]\cdot 2H_2O$
I^0O^3	$Zn_4O(1,4\text{-BDC})_3$, terephthalate
I^1O^0	$[Nd_2(H_2O)2(C_{14}H_8O_4)_3]$, diphenate
I^1O^1	$[Cd(H_2O)_2(1,3\text{-BDC})]$, isophthalate
I^1O^2	$[La_3(1,4\text{-HCHDC})_2(1,4\text{CHDC})_5(H_2O)_2]\cdot H_2O$
I^2O^0	$[Cd(1,2\text{-CHDC})]$
I^2O^1	$Co_2(H_2O)_2(O_3P(CH_2)_2PO_3)$, phosphonate
I^3O^0	$[Ni_7(OH)_2(C_4H_4O_4)_6(H_2O)_2\cdot 2H_2O]$, succinate
I^3O^0	$[Cd(C_3H_2O_4)(H_2O)]\cdot H_2O$, malonate

Figure 1.6 Left panel shows the classification of hybrid system according to connectivity as proposed by Rao and Cheetham[47]. Right panel shows example of different hybrids belonging to different class according to connectivity. Reproduced from Ref. [47]

materials [50, 51, 52, 53, 54] and hybrid metal oxides are synthesized [55, 56, 57, 58, 59, 60].

1.4.1 Classification of Organic-Inorganic Hybrids

The family of these hybrid materials are huge. To track this whole class of materials Rao and Cheetham [47] proposed a way to classify these materials on the basis of connectivity between organic and inorganic centres. The classification are shown in Fig. (1.6).

Present thesis deals with those organic-inorganic hybrid systems, which have 3-D connected network. These class of hybrids show various novel feature, some are discussed in the following section.

1.4.2 Different novel physical properties

A. Magnetic Property: A variety of magnetic properties have been found in hybrid materials. For example, a chiral 3D nickel glutarate $[Ni_{20}(H_2O)_8(C_5H_6O_4)_{20}.40H_2O]$ [61] shows a pure co-operative ferromagnetic behavior with $T_c \approx 4$ K, without any spin frustration. Another example is cobalt succinate, $[Co_5(OH)_2(C_4H_4O_4)_4]$, exhibiting ferrimagnetic interactions, is a 2D metal oxide framework

pillared by the succinate moiety into a 3D network (I^2O^1) [62]. It is constructed from zig-zag layers of edge-sharing cobalt octahedra that generate pentamers of octahedra and 12-membered ring cavities. The succinate moieties act as bridges between the sheets. This compound exhibits ferrimagnetic behavior below 10 K. Similarly the system 1,4-cyclohexane dicarboxylate, $[Co_5(OH)_8$ (CHDC).$4H_2O]$, has the highest T_c = 60 K, observed in this class of compounds [63]. The gist of all different types of magnetic behavior are listed in the Table. (1.5).

Optical properties : One of the major interesting properties from application point of view are the optical properties. For example system like 2D cadmium phthalate, [Cd(1,2-BDC)(H_2O)] [64], 3D porous, $[Cd_3L_6](BF_4)_2$-$(SiF_6)(OH)_2.13.5H_2O$, where L = 2,6-di-(4-triazolyl)pyridine,[65] 3D pyridine-2,5-dicarboxylate-$[Ln_3(OH)_4$(2,5-pydc)$(2,5\text{-Hpydc})_3(H_2O)_4]$ where (Ln = Dy, Eu) [66] all shown fluorescence property in different wave length regions.

Electronic properties : The organic-inorganic hybrid systems are also very popular for their interesting insulating and semiconducting properties. For example 3D compound, $Cu(DCNQI)_2$,(DCNQI= N,N′ -dicyano quinodiimine) formed by the linkages between Cu ion donors and organic DCNQI acceptors exhibits an interesting metal-insulator (M-I) transition under high pressure [67]. This behavior is due to the interaction between the localized 3-*d* electron bands of the Cu ions and the p-electron conductive bands of DCNQI. On the other hand 3-*d*-4*f* heterometallic Ln_6Cu_{24} clusters $[Ln_6Cu_{24}(OH)_{30}(Ala)_{12}(Ac)_6(ClO_4)(H_2O)_{12}].(ClO_4)_{10}.(OH)_7.(H_2O)_{34}$, (Ln= Tb, Gd, Sm and La) with L-alanine as the ligand reveal that they are ionic conductors [68]. Recently a novel hybrid compound, κ-$BETS_2[Fe^{III}(C_2O_4)Cl_2]$,(BETS = bis(ethylenedithio)) is found to display metallic behavior down to 4.2 K, with a large optical anisotropy [69].

Dielectric properties : Some of hybrid systems are very good dielectrics. For example,3D [Cd(papa)(Hpapa)]$ClO_4.H_2O$, Hpapa=3-(3-pyridyl)-3-aminopropionic acid [70] and Cd(TBP)Cl, HTBP = N-(4-(1H-tetrazol-5-yl)benzyl) [71] praline both crystallize in non-centro symmetric space group, showing very good ferroelectric property with associated hysteresis loss [71]. Some of hybrids also exhibit multiferroic properties, such as homochiral 2D compounds, [Cu((R)-hmp)(dca)] and [Cu((S)-hmp)(dca)], both show ferroelectric behavior along with a strong antiferromagnetic interaction [72]. Similarly 3D porous manganese formate, $[Mn_3(HCOO)_6].(C_2H_5OH)$, with 1D channels along the b-axis, exhibits a ferroelectric transition at 165 K and a ferrimagnetic transition at 8.5 K [73].

Storage properties : One of the major appealing property of these hybrid materials is the storage property, such as H_2 storage, CO_2 storage etc. Typical example of such hybrids are, Zn_4O(1,3,5-benzenetribenzoate)$_2$ [74] acting as H_2 storage system at 77 K temperature and 70 bar pressure. Another example of CO_2 storage system is 3D erbium 1,4-phenylendiacetate, $[Er_2(PDA)_3(H_2O)].2H_2O$ [75] acting as CO_2 storage system.1,3,5-benzenetricarboxylate, Dy(BTC) (H_2O).DMF act as both H_2 and CO_2 storage system [76].

1.5 Overview of Present Thesis

It is evident from several examples presented in the previous section that variety of class of system show variety of properties which are not completely understood in microscopic level. Therefore first principles calculations on these compounds have been most obvious choice, in terms of making accurate predictions in microscopic level. Needless to say, the impressive improvements in computational techniques and computer resources helped to reach this point. First principle calculations help to understand the structure and many intriguing properties of these compounds, which at a glance seems to be very complex with many degrees of freedom. The understanding at the microscopic level opens avenues for the design of new materials. A better understanding of the interplay between the different ordering like magnetic, charge and orbital degrees of freedom will lead to the identification of materials with desirable functional properties .

In this present thesis we have studied six different type of system grouped into three different class of materials as mentioned in the last section. The systems are perovskite materials Sr/$CaRuO_3$, $BiCoO_3$, low dimensional spin system $Sr_3BB'O_6$ (B=Ni, Cu; B′=Pt, Ir), $Zn_2VO(PO_4)_2$, hybrid materials $Mn(C_4H_4O_4)$ and F-Nb coordination polymer. First principles calculations have been done on these compounds to understand from microscopic point of view the exciting properties exhibited by them. The contents of the various chapters discussed in the present thesis are as follows :

Chapter 2: In this chapter, we discuss the theoretical background of the DFT and applying the same, how in practice one can solve a many electron Hamiltonian. Additionally We discuss the different basis sets which we have considered during the course of calculation, depending upon the properties we

have studied. We discuss the construction of low energy model Hamiltonian of such complex materials starting from a first-principles calculation. We also discuss few tools beyond the zero temperature DFT such as Ab-initio molecular dynamics and Dynamical mean field theory.

Chapter 3: In this chapter we propose a possible reason of observed different magnetic properties in 4-*d* Ru based systems, such as ferromagnetic ordering in $SrRuO_3$ and absence of magnetic ordering in $CaRuO_3$. Our study show that the observed varies ground state magnetic properties can be explained in term of covelency effect between 'A' site cation and oxygen sites. Our theoretical results are consistent with the experimental findings. We also discuss the correlated aspect of these systems.

Chapter 4: In this chapter, we study the changes in the electronic structure of $BiCoO_3$ between the ambient-pressure condition and the high-pressure condition. Our study shows that the application of high pressure drives the high-spin-to-low-spin transition at the Co site. We find that the finite mixing of a Bi lone pair with O p drives the $GdFeO_3$ type of orthorhombic distortion at high pressure, as opposed to previously predicted cubic or tetragonal symmetry of the high-pressure phase. This orthorhombic distortion gives rise to semiconducting behavior in contrast to previously predicted metallic or semimetallic behavior. Our study provides justification for the drop in resistivity on increasing pressure, as observed experimentally.

Chapter 5: In this chapter, we investigate the electronic structure of a class of low dimensional quantum spin systems of general formula $A_3BB'O_6$, which has drawn recent interest due to their intriguing magnetic properties. In our study, we focus on three compounds, Sr_3NiPtO_6, Sr_3CuPtO_6, and Sr_3NiIrO_6, formed from choices of 3*d* and 5*d* elements in B and B$'$ sites. Based on our first-principles calculations, we derive the strength of magnetic interactions and the single-ion anisotropies, which define the underlying spin models for the three compounds.

Chapter 6: In this chapter, We derive the low-energy spin model of the compound $Zn_2VO(PO_4)_2$, and $\frac{1}{4}$-th Ti-substituted compound $Zn_8TiV_3O_4(PO_4)_8$ which is yet to be synthesized. We compute the thermodynamics properties of the proposed spin models by the quantum Monte Carlo technique. For the pristine compound ($Zn_2VO(PO_4)_2$) our computed susceptibility is found to be in good agreement with the available experimental data and is in accordance with the earlier proposed spin model of the spin-$\frac{1}{2}$ antiferromagnetic square lattice. Upon Ti substitution, which may be viewed as $\frac{1}{4}$-spin depletion, the two- dimensional antiferromagnetic square-lattice behavior of the parent compound is found

to be altered significantly, giving rise to spin-gap behavior.

Chapter 7: Using first-principles density functional theory based calculations, in this chapter we study the electronic structure and magnetism in a succinate-based hybrid compound $Mn(C_4H_4O_4)$ consisting of both organic and inorganic components. Our study reproduces the two-step ordering of Mn spins, with the first ordering being at the edge-shared layer, followed by the second ordering at the corner-shared Mn layer, in agreement with the recent experimental observations. The origin of this two-step ordering turned out to be due to differential covalency between Mn and neighboring C and O, in two different Mn layers. This study justifies the applicability of density-functional-theory-based calculations in the description of hybrid compounds.

Chapter 8: In this chapter we explore spin-crossover (SCO) phenomenon in coordination polymers. We demonstrate the applicability of the DFT combined with the Ab-initio molecular dynamics method for the case of Fe-Nb bimetallic metal-organic framework. Our study shows that this approach is capable of capturing the SCO transitions driven by pressure as well as temperature. In addition to discovering novel spin-state transitions, magnetic states involving changes in the long-range magnetic ordering pattern are achieved, thereby offering the tunability of spin states as well as the long-range order of the spins. We compare the SCO transition in the Fe-based framework with a computer designed Mn-based variant.

Table 1.5 Variety of magnetic properties of different organic-inorganic hybrids. Reproduced from Ref. [47]

Sr. No.	Formula	I^nO^m	Properties
(A)	Ferromagnetic (FM)		
1	Glutarate	I^3O^0	$T_c \simeq 4$ K
	$[Ni_{20}(H_2O)_8(C_5H_6O_4)_{20}.40H_2O]$		
2	1,4-cyclohexane dicarboxylate	I^2O^1	$T_c \simeq 60$ K
	$[Co_5(OH)_8(CHDC).4H_2O]$		
3	Succinate	I^1O^2	Super exchange interaction
	$[Ln_2(C_4H_4O_4)_3(H_2O)_2].0.5H_2O$		
	Ln = Gd, Dy		
(B)	Ferrimagnetic (FiM)		
1	Succinate	I^2O^1	$T_N \simeq 10$ K
	$[Co_5(OH)_2(C_4H_4O_4)_4]$		
2	Succinate	I^2O^0	$T_N \simeq 10$ K
	$[Co_4(OH)_2(H_2O)_2(C_4H_4O_4)_3.2H_2O]$		
3	Fumarate	I^1O^2	$T_N \simeq 20$ K
	$[Ni_3(OH)_2(H_2O)_4(C_4H_2O_4)_2.2H_2O]$		
(C)	Canted antiferromagnetic (CAFM)		
1	Terephthalate	I^2O^1	$T < 45$ K
	$[Co_2(OH)_2(1,4\text{-BDC})]$		
2	Terephthalate	I^2O^1	$T < 20$ K
	$V_2^{IV}O_2F_2O2C\text{-}C_6H_4CO_2$		
(D)	Antiferromagnetic (AFM)		
1	Ethylenediphosphonate	I^2O^1	$T_N \simeq 7$ K, M= Co
	$M_2^{II}(H_2O)_2(O_3P(CH_2)_2PO_3)$	$T_N \simeq 7$ K, M=Ni	
2	Succinate	I^2O^1	$T_N \simeq 26$ K
	$[Co_6(OH)_2(C_4H_4O_4)_5.H_2O]$		
3	Terephthalate	I^1O^2	$T_N \simeq 5$ K
	$Fe_2OO_2C\text{-}CH_32$1,4-BDC.$2CH_3OH$		

Bibliography

[1] D. G. Marc and M. E. McHenry, Structure of Materials: an introduction to crystallography, diffraction and symmetry, Cambridge University Press. ISBN 978-0-521-65151-6 (2007).

[2] Victor M. Goldschmidt, "Die Gesetze der Krystallochemie". Die Naturwissenschaften, **21**, 477-485, (1926), Xiang Chun Liu, Rongzi Hong and Changsheng Tian, Journal of Materials Science: Materials in Electronics, **20**, 323-327 (2012).

[3] M. Murakami, K. Hirose, K. Kawamura, N. Sata and Y. Ohishi, Science **304**, 855-858 (2004); A. R. Oganov and S. Ono, Nature **403**, 445 (2004).

[4] J. B. Goodenough, J. A. Kafalas, J. M. Longo, Preparation methods in Solid State Chemistry, Academic Press (1972).

[5] J.G. Zhao, L.X. Yang, Y. Yu, F.Y. Li, R.C. Yu, Z. Fang, L.C. Chen and C.Q. Jin, J. of Solid State Chemistry **180**, 2816-2823 (2007); Seung-Tae Hong and Arthur W. Sleight, J. of Solid State Chemistry **128**, 251-255 (1997).

[6] S. Geller, J. B. Jeffries, P. J. Curlander, Acta. Crystallographic **B31**, 2770 (1975).

[7] R.C. Liebermann, L.E.A. Jones, A.E. Ringwood, Phys. Earth Planet. Inter. **14**, 165 (1977).

[8] S. N. Ruddlesden and P. Popper, Acta. Cryst. **10**, 538 (1957); S. N. Ruddlesden and P. Popper, Acta. Cryst. **11**, 54 (1958).

[9] A.F. Well, Structural Inorganic Chemistry, pp. 575 (5th ed.), Oxford University Press (1984).

[10] A.F. Cotton, G. Wilkinson, Advanced Inorganic Chemistry, John Wiley and Sons (1988).

[11] F.S. Galasso, Perovskites and High Tc Superconductors, Gordon and Breach, New York (1990).

[12] R.H. Mitchell, T. Bay, Perovskites Modern and Ancient, Ontario Almaz Press (2002).

[13] P. Fazekas, Lecture Notes on Electron Correlations and Magnetism (World Scientific, Singapore, 1999).

[14] M. Imada, A. Fujimori, Y. Tokura, Rev. Mod. Phys. **70**, 1039 (1998).

[15] P. W. Anderson, Phys. Rev. **115**, 2 (1959); Solid State Physics **14**, 99 (1963); A Career in Theoretical Physics, pp. 113-129, World Scientific, Singapore, 1994.

[16] J. B. Goodenough, Progr. Solid State Chern. **5**, 149-399 (1971).

[17] N. Y. Vasanthacharya, P. Ganguly, J. B. Goodenough, C. N. R. Rao, J. Phys. C **17**, 2745-60 (1984).

[18] R. A. Mohan Ram, P. Ganguly, C. N. R. Rao, J. M. Honig, Mater. Res. Bull. **23**, 501-5 (1988).

[19] Y. Maeno, H. Hashimoto, K. Yoshida, S. Nishizaki, T. Fujita, J. G. Bednorz and F. Lichtenberg, Nature, **372**, 532-534 (1994).

[20] R. A. Mohan Ram, L. Ganapathi, P. Ganguly and C. N. R. Rao, J. Solid State Chem. **63**, 139-147 (1986); C. N. R. Rao, P. Ganguly, K. K. Singh and R. A. Mohan Ram, J. Solid State Chem. **72**, 14-23 (1988).

[21] R. Portier, A. Carpy, M. Fayard and J. Galy, Phys. Status Solidi A **30**, 683-89 (1975).

[22] D. C. Johnston, H. Prakash, W. H. Zachariascn and R. Viswanathan, Mater. Res. Bull. **8**, 777-782 (1973); P. M. Lambert, M. R. Harrison and P. P. Edwards, J. Solid State Chem. **75**, 332-346 (1988).

[23] R. A. Beyerlein, H. S. Horowitz and J. M. Longo, J. Solid State Chem. **72**, 2-13 (1988).

[24] C. N. R. Rao, Int. Rev. Phys. Chem. **4**, 19-38 (1985).

[25] H. Imoto and A. Simon, Inorg. Chem. **21**, 308-314 (1982).

[26] G. Shirane, Y. Endoh, R. J. Birgneau, M. A. Katsner, Y. Hidaka, M. Oda, M. Suzuki, T. Murakami, Phys. Rev. Lett. **59**, 1613 (1987).

[27] L. E. Cross and R.E. Newham, History of Ferroelectrics, Ceramics and Civilization, Volume 111. (1987) by The American Ceramic Society.

[28] M.A. Korotin, S.Yu. Ezhov, I.V. Solovyev, V.I. Anisimov, D.I. Khomskii, and G.A. Sawatzky, Phys. Rev. B **54**, 5309 (1996); P. M. Raccah and J. B. Goodenough Phys. Rev. **155**, 932 (1967).

[29] P. P. Edwards, C. N. R. Rao, eds. The Metallic and the Nonmetallic States of Mauer. London: Taylor and Francis (1985).

[30] M. T. Hutchings, G. Shirane, R. J. Birgeneau and S. L. Holt, Phys. Rev. B **5**, 1999 (1972).

[31] E. Dagotto and T.M Rice, Science **271**, 618 (1996).

[32] H. Bethe, Z. Physik **71**, 205 (1931).

[33] A. W. Sandvik, E. Dagotto and D. J. Scalapino, Phys. Rev. B **53**, R2934-R2937 (1996).

[34] F. D. M. Halden, Phys. Rev. Lett. **50**, 1153 (1983).

[35] Y. Sasago, M. Hase, K. Uchinokura, M. Tokunaga and N. Miura, Phys. Rev. B **52**, 3533 (1995).

[36] M. Nishi, O. Fujita and J. Akimitsu, Phys. Rev. B **50**, 6508 (1994).

[37] M. Azuma, Z. Hiroi, M. Takano, K. Ishida and Y. Kitaoka, Phys. Rev. Lett. **73**, 3463 (1994).

[38] C. Weeks, Y. Song, M. Suzuki, N. A. Chernova, P. Y. Zavalij and M.S. Whittingham, J. Mater. Chem. **13**, 1420 (2003).

[39] A. Auerbach, Interacting electrons and Quantum Magnetism, Springer Series.

[40] G.S. Uhrig and H.J. Schulz, Phys. Rev. B **54**, R9624 (1996).

[41] C. C. Torardi and J. C, Calabrese, Inorg. Chem. **23**, 1308 (1984); C. C. Torardi, Z. G. Li, H. S. Horowitz, W. Liang and W. H. Whangbo, J. Solid State Chem. **119**, 349 (1995).

[42] Y. Yoshida, K. Yurue, M. Mitoh, T. Kawae, Y. Hosokoshi, K. Inoue, M. Kinoshita and K. Takeda, Physica B: Condensed Matter **979**, 329-333 (2003).

[43] J.W Bray, L.V. Interrante, I.S. Jacobs and L.C. Bonner, "Extended Linear chain Compounds" vol. 3, pp-353 (1983).

[44] S. Huizinga, J. Kommandeur, G. A. Sawatzky, B. T. Thole ,K. Kopinga, W. J. M. de Jonge, and J. Roos, Phys. Rev. B **19**, 4723 (1979).

[45] J. W. Bray, H. R. Hart, Jr., L. V. Interrante, I. S. Jacobs, J. S. Kasper, G. D. Watkins, S. H. Wee and J. C. Bonner, Phys. Rev. Lett. **35**, 744 (1975).

[46] I. S. Jacobs, J. W. Bray, H. R. Hart, Jr., L. V. Interrante, J. S. Kasper, and G. D. Watkins,D. E. Prober and J. C. Bonner, Phys. Rev. B **14**, 3036 (1976).

[47] C. N. R. Rao, A. K. Cheetham and A. Thirumurugan, J. Phys. Condens. Matter **20**, 083202 (2008).

[48] L. J. Murray, M. Dinca, and J. R. Long, Chem. Soc. Rev. **38**, 1294 (2009).

[49] J. C. Jr. Bailar, Prep. Inorg. React. **1**, 1 (1964).

[50] B. F. Hoskins and R. Robson, J. Am. Chem. Soc. **112**, 1546 (1990).

[51] R. Robson, J. Chem. Soc., Dalton Trans. **3735** (2000).

[52] B. Moulton and M. J. Zaworotko, Chem. Rev. **101**, 1629 (2001).

[53] B. Moulton and M. J. Zaworotko, Curr. Opin. Solid State Mater. Sci. **6**, 117 (2002).

[54] M. O. Keeffe, M. EddaoudiM, H. Li, T. Reineke and O. M. Yaghi, J. Solid State Chem. **152**, 3 (2000).

[55] A. Clearfield, Curr. Opin. Solid State Mater. Sci. **6**, 495 (2002).

[56] A. K. Cheetham and P. M. Forster, Top. Catal. **24**, 79 (2003).

[57] J. L. C. Rowsell and O. M. Yaghi, Micropor. Mesopor.Mater. **73**, 3 (2004).

[58] M. J. Rosseinsky, Micropor. Mesopor. Mater. **73**, 15 (2004).

[59] C. N. R. Rao, S. Natarajan and R. Vaidhayanathan, Angew. Chem. Int. Edn **43**, 1466 (2004).

[60] A. K. Cheetham, C. N. R. Rao and R. K. Feller, Chem. Commun. **4780** (2006).

[61] N. Guillou, C. Livage, M. Drillon and G. FÂt'erey, Angew. Chem. Int. Edn **42**, 5314 (2003).

[62] C. Livage, C. Egger, M. Nogues and G. Ferey, J. Mater. Chem. **8**, 2743 (1998).

[63] M. Kurmoo, H. Kumagai, S. M. Hughes and C. J. Kepert, Inorg. Chem. **42**, 6709 (2003).

[64] S. Wang, Y. Hou, E. Wang, Y. Li, L. Xu, J. Peng, S. Liua and C. Hua, New J. Chem. **27**, 1144 (2003).

[65] Y-Q. Huang, B. Ding, H-B Song, B. Zhao, P. Ren, P. Cheng, H-G. Wang, D-Z. Liao and S- P. Yan, Chem. Commun. **4906** (2006).

[66] J. Yang, Q. Yue, G-D. Li, J-J. Cao, G-H. Li and J-S. Chen, Inorg. Chem. **45**, 2857 (2006).

[67] R. Kato, Bull. Chem. Soc. Japan **73**, 515 (2000).

[68] J-J. Zhang, T-L. Sheng, S-Q. Xia, G. Leibeling, F. Meyer, S-M. Hu, R-B. Fu, S-C. Xiang and X-T. Wu, Inorg. Chem. **43**, 5472 (2004).

[69] B. Zhang, Z. Wang, Y. Zhang, K. Takahashi, Y. Okano, H. Cui, H.Kobayashi, K. Inoue, M. Kurmoo, F. L. Pratt and D. Zhu, Inorg. Chem. **45**, 3275 (2006).

[70] Z-R. Qu, H. Zhao, Y-P. Wang, X-S. Wang, Q. Ye, Y-H. Li, R-G. Xiong, B. F. Abrahams, Z-G. Liu, Z-L. Xue and X-Z. You, Chem. Eur. J. **10**, 53 (2004).

[71] Q. Ye, Y-M. Song, G-X. Wang, K. Chen, D-W. Fu, P. W. H. Chan, J-S. Zhu, S. D. Huang and R-G. Xiong, J. Am. Chem. Soc. **128**, 6554 (2006).

[72] Z-G. Gu, X-H. Zhou, Y-B. Jin, R-G. Xiong, J-L. Zuo and X-Z. You, Inorg. Chem. **46**, 5462 (2007).

[73] H. Cui, Z. Wang, K. Takahashi, Y. Okano, H. Kobayashi and A. Kobayashi, J. Am. Chem. Soc. **128**, 15074 (2006).

[74] H. Furukawa, M. A. Miller and O. M. Yaghi, J. Mater. Chem. **17**, 3197 (2007).

[75] L. Pan, K. M. Adams, H. E. Hernandez, X. Wang, C. Zheng, Y. Hattori and K. Kaneko, J. Am. Chem. Soc. **125**, 3062 (2003).

[76] X. Guo, G. Zhu, Z. Li, F. Sun, Z. Yang and S. Qiu, Chem. Commun. **3172** (2006).

Chapter 2

Theoretical Basics of electronic structure calculations

2.1 Foundation of Density Functional Theory (DFT)

2.1.1 The many-electron Hamiltonian

The behavior of materials are governed by the constituent atoms, and many of the properties are governed by the electrons in the materials. Therefore, to understand the properties of material, namely electronic, magnetic and optical properties we have to analyze the electronic behavior in their surrounded environment of nuclei. The general theory for any material, composed of ions and electrons is quantum mechanical and it may be based on the time- independent non-relativistic Schrödinger equation of the form,

$$\hat{H}\psi(\mathbf{r_1},\mathbf{r_2}...\mathbf{r_N},\mathbf{R_1},\mathbf{R_2}..\mathbf{R_P}) = E\psi(\mathbf{r_1},\mathbf{r_2}...\mathbf{r_N},\mathbf{R_1},\mathbf{R_2}..\mathbf{R_P}), \tag{2.1}$$

where, $\hat{H}$ is the Hamiltonian for a system of N number of electrons and P number of nuclei.

The general form of $\hat{H}$ for any interacting system can be written as,

$$H = -\frac{\hbar^2}{2m_e}\sum_{i=1}^{N}\nabla^2_{\mathbf{r_i}} - \frac{\hbar^2}{2M_I}\sum_{I=1}^{P}\nabla^2_{\mathbf{R_I}} - \frac{1}{4\pi\varepsilon_0}\sum_{i,I}\frac{Z_I e^2}{|\mathbf{R_I}-\mathbf{r_i}|} + \frac{1}{2}\frac{1}{4\pi\varepsilon_0}\sum_{i>j}\frac{e^2}{|\mathbf{r_i}-\mathbf{r_j}|} + \frac{1}{4\pi\varepsilon_0}\sum_{I>J}\frac{Z_I Z_J e^2}{|\mathbf{R_I}-\mathbf{R_J}|}, \tag{2.2}$$

where, the mass of the electron at $\mathbf{r_i}$ is m_i and that of nucleus at $\mathbf{R_I}$ is M_I. Z is the atomic number of the nucleus, summation <i,j> runs over the number of electrons *i.e* N, and summation <I,J> runs over the number of nuclei *i.e* P in the system.

First term in Eq.(2.2) is the kinetic energy (K.E) term of electron at $\mathbf{r_i}$, whereas the 2nd term is the K.E term of a nucleus at coordinate $\mathbf{R_I}$. The 3rd and 4th term denote repulsive coulomb interaction term between two electrons at position $\mathbf{r_i}$ and $\mathbf{r_j}$ and between two ion cores at positions $\mathbf{R_I}$ and $\mathbf{R_J}$ respectively. The last term denotes the attractive coulomb interaction between negative charge, electron at position $\mathbf{r_i}$, and positively charged ion at position $\mathbf{R_I}$.

Exact solution of Eq.(2.2) is almost impossible, except for very small system, due to large number of degrees of freedom involved in this equation as well as coupled nature of different interacting terms. Therefore to solve this equation we need to do several approximations at different levels.
The first reasonable approximation to solve this complex systems, is the *Adiabatic approximation* or *Born-Oppenheimer approximation* [1]. This approximation is basically based on the difference in the time scales associated with the motion of electrons and nuclei. The mass of the nuclei are much heavier compared to electrons, therefore the motion of the nuclei are slower than that of the electron. Therefore we can ignore the smaller K.E term of the ion and the ion-ion interaction term [last term in Eq. (2.2)] can be assumed to be constant with respect to the electron. Under this adiabatic approximation the Hamiltonian becomes somewhat simpler,

$$\hat{H} = -\frac{\hbar^2}{2m_e}\sum_{i=1}^{N}\nabla^2_{\mathbf{r_i}} - \frac{1}{4\pi\varepsilon_0}\sum_{i,I}\frac{Z_I e^2}{|\mathbf{R_I}-\mathbf{r_i}|} + \frac{1}{2}\frac{1}{4\pi\varepsilon_0}\sum_{i,j}\frac{e^2}{|\mathbf{r_i}-\mathbf{r_j}|} + E_{Madelung}, \tag{2.3}$$

where, $E_{Madelung}$ is the constant energy term coming from ion-ion interactions.
In spite of this major simplification by ignoring explicit ionic degrees of freedom, Eq.(2.3) can not be solved exactly due to the interacting nature of the electrons. The next level of approximation is the *Independent Electron Approximation*. In this approximation we effectively map the interacting problem into a system of non-interacting particle in an efficient external potential. Till date there are only two effective approaches for solving this mapped single particle problem; 1) Wave function based approach, 2) Density based approach.

2.1.2 Wave function based approach for electronic structure calculation

The wave function based approach relies on the assumption that each electron can be represented by its own wave function, which is function of individual electronic coordinate only. This approximation is known as *independent electron approximation*. That means the Hamiltonian for each electron should look like,

$$\hat{H}_i = -\frac{\hbar^2}{2m_i}\bigtriangledown_i^2 - \frac{1}{4\pi\varepsilon_0}\sum_I \frac{Z_I e^2}{|\mathbf{R_I}-\mathbf{r_i}|} + \upsilon_i(|r_i|), \tag{2.4}$$

where, the first term represents the K.E of the i-th the electron, 2nd term represents the coulomb interaction at i-th electron due to other ions and 3rd term represents the effective average interaction potential as felt by the i-th electron due to all other electrons in the system. The total wave function of the system within this approximation is the product of all single particle wave functions,

$$\psi^H(\mathbf{r_1},\mathbf{r_2}\ldots,\mathbf{r_N}) = \phi_1(\mathbf{r_1})\phi_2(\mathbf{r_2})\ldots\phi_N(\mathbf{r_N}). \tag{2.5}$$

Hartee in 1928 first proposed [2] the way of solving the many body problem via this product of single particle wave function method. Though it takes into account the electron-electron interaction in a mean field way, there are a few very severe inherent problem in the formulation of product wave function. Hartee treats the electrons as a distinguishable particles, however electrons are S=$\frac{1}{2}$ indistinguishable fermions and the associated wave function should obey Pauli exclusion principle, which stats that " for a system of electrons the total wave function must be anti-symmetric in the electronic coordinates including spin". Therefore next level of modification has been made by Fock [3] by introducing anti symmetry property in the construction of many body wave function out of N number of single particle wave functions in the form of Slater determinant;

$$\psi^{HF} = \frac{1}{\sqrt{N!}}\begin{vmatrix} \phi_1(\mathbf{r_1}) & \phi_1(\mathbf{r_2}) & \cdots & \phi_1(\mathbf{r_N}) \\ \phi_2(\mathbf{r_1}) & \phi_2(\mathbf{r_2}) & \cdots & \phi_2\mathbf{r_N}) \\ \vdots & \vdots & \ddots & \vdots \\ \phi_N(\mathbf{r_1}) & \phi_N(\mathbf{r_2}) & \cdots & \phi_N(\mathbf{r_N}) \end{vmatrix} \tag{2.6}$$

Solving Eq.(2.4) by variational principle using determinantal wave function, the composite Hartee-Fock equation looks like;

$$H_i = -\frac{\hbar^2}{2m_e}\nabla^2_{\mathbf{r_i}} + V_{ion}(\mathbf{r_i}) + e^2\sum_j^{occ}\int \frac{\left|\phi_j(\mathbf{r_j})\right|^2}{\left|\mathbf{r_i}-\mathbf{r_j}\right|}d\mathbf{r_j} - \sum_j^{occ}\phi_j(\mathbf{r_i})\int \phi_j^*(\mathbf{r_j})\frac{e^2}{\left|\mathbf{r_i}-\mathbf{r_j}\right|}\phi_i(\mathbf{r_j})\,d\mathbf{r_j}, \quad (2.7)$$

where, the 3rd term is the Hartee term which represents the electron-electron coulomb interaction in an approximate way, the last term represents a new term called *exchange* term arising due to antisymmetric nature of the determinantal wave function.

The main drawback of Hartee-Fock (HF) formalism is that it completely ignores the electron-electron correlation term. More over huge computational resources are needed for capturing the detailed wave function. In spite of these facts various many body computational tools are developed specifically in the chemistry community based on the extension of HF method. Although some of the methods are potentially accurate but extending these methods to large and complex systems produces an almost exponential increase of the computational difficulty.

2.1.3 Density based approach: Density Functional Theory

Simultaneously as development of HF method, Thomas and Fermi suggested an alternative way of treating many electron systems by considering full electronic density as a basic variable of the many electronic system, ignoring the specific details of the individual electrons. Though the Thomas-Fermi approximation did not survive due to insufficient treatment of K.E as well as correlation and exchange terms, along the same line of thought, after a few decades in 1964, Hohenberg and Kohn proposed *Density Functional Theory* (DFT) [4] for dealing with the many electron systems more efficiently by considering the ground state electron density as the variable of many body Schrödinger equation instead of electronic wave function ignoring other specific details. The ground state electron density is defined as;

$$\rho(\mathbf{r}) = N\int \psi^*(\mathbf{r},\mathbf{r_2},\ldots,\mathbf{r_N})\,\psi(\mathbf{r},\mathbf{r_2},\cdots,\mathbf{r_N})\,d\mathbf{r_2}d\mathbf{r_3}\ldots d\mathbf{r_N}, \quad (2.8)$$

where, $\psi(\mathbf{r_1},\mathbf{r_2},\ldots,\mathbf{r_N})$ is the many electron wave function. By doing this the degrees of freedom of the problem reduced from 3N variable to 3 variable. If we know all the distributions of ground state electron density, then in principle we can calculate all the ground state properties of many electron systems. Density functional theory is based on two basic theorems of Hohenberg-Kohn (HK). The

ground state energy of a system on N interacting electrons, is given by,

$$E = \langle \psi | \hat{T}_e + \hat{V}_{ne} + \hat{U}_{ee} | \psi \rangle, \tag{2.9}$$

where, one can express the first term, *i.e* the K.E of an electron as a functional of density by,

$$T_e[\rho] = -\frac{\hbar^2}{2m} \int \left[\nabla^2_{\mathbf{r}} \rho(\mathbf{r}, \mathbf{r}') \right] d\mathbf{r}, \tag{2.10}$$

$\nabla_{\mathbf{r}}$ is the derivative with respect to position coordinates of particles, and

$$V_{ne} = \sum_{I=1}^{P} \int \rho(\mathbf{r}) \upsilon_I(\mathbf{r} - \mathbf{R}_I) d\mathbf{r}, \tag{2.11}$$

The exact functional form of the third term of the above Eq. is unknown. Hohenberg-Kohn in 1964 gave a proposal, which basically tells us what we can compute using density.

1^{st} **HK theorem::** The external potential of many electron system is uniquely determined by the ground state electron density of many electron system, except for a trivial additive constant term. That means there is a one-to-one correspondence between electron density $\rho(r)$ and the external potential V_{ne}. An immediate consequence is that the ground state expectation value of any observable say $\hat{O}$ is an unique functional of the ground state density ρ_0, *i.e* ,

$$\left\langle \Psi | \hat{O} | \Psi \right\rangle = O[\rho_0].$$

Let us consider a particular electronic system characterized by two different external potential v_1 and v_2, such that their ground state density is same $\rho(r)$. Let us consider the wave function corresponding to two different external potential is ψ_1 and ψ_2 respectively. Therefore,

$$E_1 = \langle \psi_1 | \hat{H}_1 | \psi_1 \rangle,$$

$$E_2 = \langle \psi_2 | \hat{H}_2 | \psi_2 \rangle,$$

using variation principle one can write ;

$$E_1 = \langle \psi_1 | \hat{H}_1 | \psi_1 \rangle,$$

$$\therefore E_1 < \langle \psi_2 | \hat{H}_1 | \psi_2 \rangle = \langle \psi_2 | \hat{H}_2 | \psi_2 \rangle + \langle \psi_1 | \hat{H}_1 - \hat{H}_2 | \psi_1 \rangle,$$

now $\hat{H} = \hat{T} + \hat{U} + \hat{V}$ hence

$$E_1 < \langle \psi_2 | \hat{H}_2 | \psi_2 \rangle + \langle \psi_1 | V_1(\mathbf{r}) - V_2(\mathbf{r}) | \psi_2 \rangle,$$

$$\therefore E_1 < E_2 + \int [V_1(\mathbf{r}) - V_2(\mathbf{r})]\,\rho(\mathbf{r})d\mathbf{r},$$

Since the potential is multiplicative operator, we can simply reverse this situation, where,

$$E_2 < E_1 + \int [V_2(\mathbf{r}) - V_1(\mathbf{r})]\,\rho(\mathbf{r})d\mathbf{r}.$$

Combining the two inequities we get, $E_1 + E_2 < E_2 + E_1$ which is not possible. Therefore our starting assumption was wrong, which means two different external potentials can not arise out of the same electron density. The wave function as well as energy therefore is an unique functional of the ground state electron density.

2^{nd} **HK theorem and Kohn-Sham Equation::**

The ground state density can be calculated, in principle exactly, using the variational method involving only density. That means the total energy for a given density or external potential is as follows;

$$E_{Tot}[\rho] = \langle \psi[\rho]\,|\hat{T} + \hat{U}|\,\psi[\rho]\rangle + \int \rho(r)V_{ext}(\mathbf{r})d\mathbf{r}.$$

The above theorem states that, the total energy ($E_{Tot}[\rho]$) will be minimum only for the ground sate density, ρ_0. That means,

$$E_{Tot}[\rho] > E_{Tot}[\rho_0].$$

where, $E_{Tot}[\rho_0]$ is the ground sate energy. In HF method we have trail wave function and consequently energy and any other observable , whereas in DFT we have trail density and from that we can get any other observable.

For the ground state density we can minimize the energy functional by using the constraint that $\int \rho(r)$dr=N using the method of Lagrangian multipliers;

$$\delta E[\rho] - \mu(\int \rho(r)dr - N) = 0,$$

which the ground state density must satisfy. Solving for μ we get,

$$\mu = \frac{\delta E[\rho]}{\delta \rho},$$

$$\therefore \mu = V_{ext}(r) + \frac{\delta F[\rho]}{\delta \rho},$$

where, 'F' is the universal functional of density applicable for any system and does not depend on the external potential.

Based on the ideas given by the Hohenberg-Kohn we have a moderately good description for separating out electrostatic exchange and correlation term. Though the correction term is the biggest challenge in this formulation, even there is a problem in the K.E term. In 1965 Kohn-Sham [5] proposed an idea of replacing the K.E term of interacting electron with that of an equivalent non-interacting system, such that the density of true interacting system is same as that of the fictitious non-interacting system. Therefore the K.E of the interacting system can be calculated via K.E of non-interacting system.

$$T = -\frac{\hbar^2}{2m}\sum_{i=1}^{\infty} f_i \langle \phi_i | \nabla^2 | \phi_i \rangle,$$

where, ϕ_i's are the one electron orbitals and f_i's are the occupation number corresponding to these orbitals. The many electron density can be related to f_i by the following relation,

$$\rho(r) = \sum_{i}^{N} f_i |\phi_i(r)|^2.$$

The eigen state can be written in slater determinant form,

$$\Phi(r) = \frac{1}{\sqrt{N!}} SD\left[\phi_1(r_1)\phi_2(r_2)...\phi_N(r_N)\right],$$

where, 'SD' stands for *slater determinant* as mentioned in the Eq. 2.6. The K.E term;

$$T\left[\rho\right] = -\frac{\hbar^2}{2m}\sum_{i=1}^{N} \langle \phi_i | \nabla^2 | \phi_i \rangle,$$

where, $\phi_i(r)$'s are the single particle orbitals for the Hamiltonian;

$$\hat{H}_{KS} = -\frac{\hbar^2}{2m}\nabla^2 + \upsilon_R(\mathbf{r}).$$

The corresponding eigen value equation is;

$$\hat{H}_{KS}\phi_i(\mathbf{r}) = \varepsilon_i \phi_i(\mathbf{r}),$$

which is known as Kohn-Sham self consistent equation which is like the single particle Schrödinger equation. ϕ_i and ε_i are fictitious single particle orbital and eigen value. The effective potential in the KS Hamiltonian,

$$\upsilon_R = v\left(\mathbf{r}\right) + V_H\left(\mathbf{r}\right) + V_{XC}\left(\mathbf{r}\right) = V_{KS}\left(\mathbf{r}\right). \tag{2.12}$$

The Kohn-Sham total energy is given by;

$$E_{KS}\left[\rho\right] = T_R\left[\rho\right] + \int \rho(r)\upsilon_{ext}(r)dr + \frac{1}{2}\int\int \frac{\rho(r)\rho(r')}{|r-r'|} d\mathbf{r}d\mathbf{r}' + E_{xc}\left[\rho\right]. \tag{2.13}$$

Therefore the fictitious non-interacting Kohn-Sham eigen value equation becomes

$$\left[-\frac{\hbar^2}{2m}\nabla^2 + V_{KS}(r)\right]\phi_i = \varepsilon_i\phi_i. \tag{2.14}$$

Since the potential V_{KS} is a functional of density and density is a function of ϕ, we have to solve this eigen value equation by using iterative methods with a starting initial guess value of density $\rho(r)$. Solving the K-S equation we will get a value of ϕ. From that ϕ we generate a new density, and put it back to the K-S equation and solve it to get new ϕ. This process should be repeated until the density converges.

2.1.3.1 Exchange- Correlation Functional

The Kohn-Sham potential can be calculated exactly except for the V_{XC} term. The corresponding energy E_{XC} involves both correlation energy as well as the exchange energy, E_{XC}=E_C+E_X, where, E_C arises due to the fact that motion of one electron depends on the motion of another electron, which is a probabilistic effect and E_X arises due to Pauli exclusion principle.

Lets us first discuss the correlation term. Let us introduce a two body direct correlation function: g($\mathbf{r},\mathbf{r}'$) such that two body density matrix can be written as;

$$\rho_2(\mathbf{r},\mathbf{r}':\mathbf{r},\mathbf{r}') = \frac{1}{2}\rho(\mathbf{r},\mathbf{r})\rho(\mathbf{r}',\mathbf{r}')g(\mathbf{r},\mathbf{r}') \tag{2.15}$$

$$\therefore \langle\phi|V_{ee}|\phi\rangle = \frac{1}{2}\int\int\frac{\rho(\mathbf{r})\rho(\mathbf{r}')}{|\mathbf{r}-\mathbf{r}'|}d\mathbf{r}d\mathbf{r}' + \frac{1}{2}\int\int\frac{\rho(\mathbf{r})\rho(\mathbf{r}')}{|\mathbf{r}-\mathbf{r}'|}\left[g(\mathbf{r},\mathbf{r}')-1\right]d\mathbf{r}d\mathbf{r}'. \tag{2.16}$$

First term of the above equation is the classical electron-electron electrostatic term and the second term represents the correlation effect. Since the correlation term is a probabilistic quantity, exact and unique functional form is not possible to define.

A widely used approximation is known as *Local Density Approximation* (LDA). In LDA approximation the exchange-correlation functional have the following form;

$$E_{XC}^{LDA} = \int\rho(\mathbf{r})\,\varepsilon_{xc}^{homo}(\rho(\mathbf{r}))\,d\mathbf{r}. \tag{2.17}$$

Under this approximation $\varepsilon_{xc}^{homo}[\rho(\mathbf{r})]$ is assumed to be the exchange and correlation energy density of the homogeneous electron gas of density ρ. In this approximation, the inhomogeneous systems are

considered as locally homogeneous. That is why this approximation is called local density approximation. The exact form of the exchange energy of the homogeneous electron gas is known [6], and it is given by;

$$\varepsilon_x(\rho) = -\frac{3e^2}{4}\left(\frac{3}{\pi}\right)^{1/3}\rho(\mathbf{r})^{1/3}.$$

The analytic form of correlation energy is not known and has been simulated for the homogeneous electron gas numerically using Monte-Carlo calculation which in turn gives exact results [7]. The resultant exchange correlation energy has been fitted by a number of analytic forms [8, 9, 10] all of which yield similar results in practice and are collectively referred to as LDA functionals. In spite of huge simplification, LDA works surprisingly well in many cases. It also gives chemical trend quite well. However there exists a number of cases where it fails in representing the correct ground state.

Since in the LDA the variation of density in space is ignored, in the next level of improvement the gradient variation of density over the spatial distribution is incorporated, and it is commonly known as *Generalized Gradient Approximation* (GGA) [11]. The general form of the exchange-correlation energy functional within GGA scheme can be written as;

$$E_{XC}^{GGA}[\rho] = \int f(\rho(\mathbf{r}), \bigtriangledown\rho(\mathbf{r}))\, d\mathbf{r}.$$

The functional form of non local functional is not unique and can be very complex involving different types of gradient contributions. The calculation presented in this thesis is mostly done within the functional form proposed by the Perdew, Burke and Ernzerhof in 1996, famously known as PBE [12]. Many other GGA functional forms are available in the literature [13, 14, 15, 16, 17, 18]. GGA provide some what better description over the LDA in most of the cases, like magnetic properties, binding energy, bond length etc.

In order to solve the eigen value problem using single particle Kohn-Sham equation, the single particle eigen states must be expanded in a set of predefined basis functions. Depending on the choice of basis function different schemes for the electronic structure calculation methods have been devised. In broad sense the basic set can be classified by the two categories, i) Energy independent basis set or fixed basis set, *e.g* tight binding linear combination of atomic orbitals (LCAO) [19] or plane wave basis

set [20] and ii) Energy dependent basis set, like cellular method [21], augmented plane wave method [22].

2.2 Different methods for electronic band structure calculations

In this thesis, the electronic structure calculations have been carried out using the three different types of methods based on three different basis sets, namely
i) Muffin tin orbital (MTO) based linear MTO (LMTO) or N-th order MTO (NMTO) method [28, 29].
ii) Plane wave based method described within the ultra-soft pseudopotentials (US-PP) [27, 26, 25] and the projector augmented wave (PAW) [38, 37] as implemented in the Vienna ab initio simulation package (VASP) [31, 32, 33], and,
iii) Full potential linear augmented plane wave based method [36, 34] as implemented in Wien2K code [39].
Brief descriptions of these methods are given below.

2.2.1 The Linear Muffin Tin orbital Method

The linear muffin tin orbital method (LMTO) [28] belongs to the class of energy independent basis set category. This method of calculating electronic structure is very elegant and computationally less expansive compared to the other methods which will be discussed in the next sections. This method is based on the *muffin tin* (MT) approximation. In this approximation the actual crystal potential is approximated by muffin tin potentials, as shown in the schematic figure (*c.f* Fig. (2.1)).

MT approximation involves dividing the crystal into two parts, a) atom centered sphere part which is commonly known as a MT sphere and b) the rest, known as interstitial. In this approximation it is assumed that inside muffin tin sphere (S_R), the potential is essentially *spherically symmetric*, whereas the potential in the interstitial region, *i.e* between the spheres is weakly varying and hence can be replaced by a constant potential. This approximation is called *"Muffin Tin Approximation"*. Mathematically it

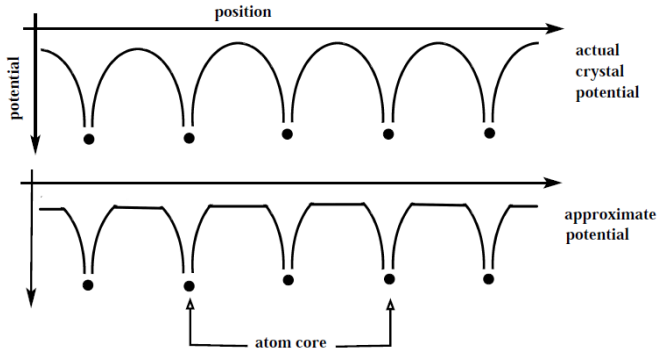

Figure 2.1 Schematic figure of actual crystal potential and the approximated potential used in LMTO formalism.

can be written as,

$$\upsilon(\mathbf{r_R}) = \begin{cases} \upsilon(r_R) & \text{for } r_R \leq S_R, \\ -\upsilon_0 & \text{for } r_R > S_R. \end{cases}$$

Within the MT sphere the radial Schrödinger equation looks like

$$\left[\frac{d^2}{dr_R^2} - \upsilon(r_R) + \frac{l(l+1)}{r_R^2} - \varepsilon\right] r_R\varphi(r_R) = 0 \tag{2.18}$$

The solution of Eq.(2.18) is partial wave , which is the product of radial part and the spherical harmonics, $\phi(\mathbf{r}_R) = \varphi(\mathbf{r}_R, \varepsilon)Y_L(r_R)$ where 'L' denotes the angular momentum labels (*l*,*m*), and $Y_L(r_R)$ is the spherical harmonic function.

Out side the MT sphere the potential is constant (-υ_0), therefore the radial part becomes

$$\left[\frac{d^2}{dr_R^2} + \frac{l(l+1)}{r_R^2} - \kappa^2\right] r_R\varphi(r_R) = 0, \tag{2.19}$$

where, $\kappa^2 = \varepsilon - \upsilon_0$. Hence in the interstitial region the solution is plane wave, which can be expanded in terms of Neumann and Bessel functions.The solutions inside and outside the MT sphere must match continuously and smoothly at the sphere boundary in order to have a well behaved wave function. The matching of two wave functions at the boundary leads to the energy dependent Korringa-Kohn-Rostoker (KKR) equation.

Though this kind of approach is quite accurate, but the energy dependence in the basis set makes the approach computationally heavy. Anderson proposed a way [23] for linearization of the energy dependent partial wave. The idea is following, use a set of reference energies (ε_v) and the basis set is constructed out of the solution of radial Schrödinger equation and its first energy derivative evaluated at the reference energies. The linearized radial basis function looks like $\phi_{RL}(\varepsilon) = \phi_{RL}(\varepsilon_v) + (\varepsilon - \varepsilon_v)\dot{\phi}_{RL}(\varepsilon_v)$ This linearization makes the basis energy independent. Finally following Andersen's approach of linearization [23], the LMTO basis functions within atomic sphere approximation (ASA) are obtained, which replaces the MT spheres by space filling atomic spheres which can be expressed as:

$$\chi^{\alpha}_{RL} = \phi_{RL}(r_R) + \sum_{R'L'} \dot{\phi}^{\alpha}_{R'L'}(r_{R'}) h^{\alpha}_{R'L',RL}, \tag{2.20}$$

where, L denotes collective angular momentum index (lm). $\dot{\phi}^{\alpha}$ is the linear combination of ϕ and its energy derivatives $\dot{\phi}$, given by $\dot{\phi}^{\alpha}_{R'L'} = \dot{\phi}_{R'L'} + \phi_{R'L'}O^{\alpha}$, O^{α} is the non-diagonal overlap matrix, r_R is defined as $\mathbf{r_R} = \mathbf{r} - \mathbf{R}$, where atomic sites are given by the position vectors $\mathbf{R}$. ϕ is the partial wave inside the sphere centered at $\mathbf{R}$ evaluated at energy of linearization ε_{vRL}. The matrix h^{α} is given by

$$h^{\alpha} = C^{\alpha} - \varepsilon_v + (\Delta^{\alpha})^{1/2} S^{\alpha} (\Delta^{\alpha})^{1/2}, \tag{2.21}$$

where C and Δ are the diagonal potential matrices. They depend on the potential inside the sphere, α (parameter choosen in such a way that it ensures the exponential decay of S^{α}), and on sphere radii. C and Δ are commonly known as *band center* and *band width* parameters and S is the structure matrix which depends on the representation and the geometrical arrangement of the atomic sites.

2.2.2 Nth Order Muffin Tin Orbital (NMTO)- a downfolding method

In order to calculate the single electron part of a correlated Hamiltonian, in an ab-initio way, hopping integrals or on-site terms, one needs to extract low energy, few band Hamiltonian out of the full DFT Hamiltonian. Downfolding technique is the way to achieve this [30]. In this technique, the space of a basis set is divided into two subsets, lower $|l\rangle$ and $|s\rangle$. The reduction of the full Hamiltonian H into the lower subset Hamiltonian $\tilde{H}_{ll}$ is carried out in such a manner that lower l eigenvalues of the original H and eigenvalues of $\tilde{H}_{ll}$ are same. The formation of $\tilde{H}_{ll}$ introduces additional energy dependence through the expression

$$\tilde{H}_{ll} = H_{ll} - H_{lh} (H_{hh} - \varepsilon)^{-1} H_{hl} \tag{2.22}$$

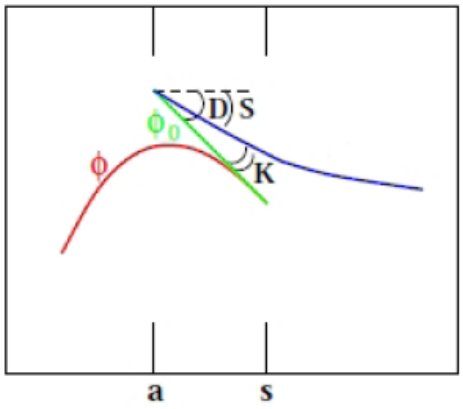

Figure 2.2 Construction of Kink partial wave

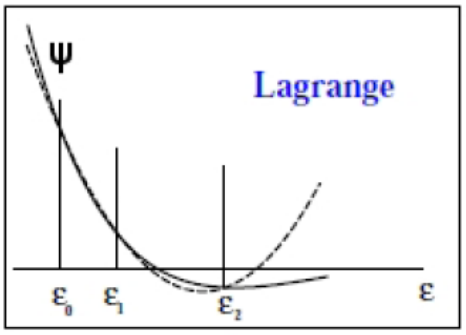

Figure 2.3 N^{th} order approximation to the energy dependence of the partial wave

which is removed through linearization or N-inazation via LMTO or NMTO method.

The implementation of downfolding technique in LMTO does not provide an accurate way to do a massive downfolding, where the downfolded bands span in a very narrow energy window. The primary disadvantages of LMTO method are the following,

(i) The basis is complete to $(\varepsilon - \varepsilon_v)$ (*i.e.* 1^{st} order) inside the sphere while it is only complete to $(\varepsilon - \varepsilon_v)^0 = 1$ (0^{th} order) in the interstitial, which is inconsistent. This inconsistency can be corrected by removing the interstitial region through introduction of atomic sphere approximation, but it makes the formalism heavy.

(ii) The expansion of the Hamiltonian H in the orthogonal representation as a power series in the two

centred tight-binding Hamiltonian h :

$$\langle\chi|\,(H-\varepsilon_v)\,|\chi\rangle = h - hoh + ... \tag{2.23}$$

is obtained only within ASA and excludes downfolding.

All these shortcomings have been taken care of in NMTO method. This is a more consistent formalism, which overcomes the above mentioned shortcomings and provides a way to describe the downfolded band structure with better accuracy within a chosen energy range. This method treats the interstitial region accurately and goes beyond the linear approximation. NMTO, like LMTO method uses the partial waves, $\phi_{RL}(\varepsilon, r_R)$ within the atomic spheres. Instead of Neumann function, in this method screened spherical waves (SSWs)are considered in the interstitial region. The central idea behind the NMTO method may be summarized in the following way.

It introduces a hard sphere of radius a and a phase shifted partial wave solution $\phi^{\alpha 0}_{RL}(\varepsilon, r_R)$ (green line in Fig. (2.2)), which matches the value and slope of ϕ at S_R, but their curvatures differ. At the hard sphere, $\phi^{\alpha 0}_{RL}(\varepsilon, r_R)$ is joined continuously but with a kink to the SSW, $\phi^{\alpha}_{RL}(\varepsilon, r_R)$, shown by blue line in Fig. (2.2). The combined form of these contributions is known as Kink Partial Waves(KPWs), which is given as

$$\psi^{\alpha}_{RL}(\varepsilon, r_R) = \left[\phi^{\alpha}_{RL}(\varepsilon, r_R) - \phi^{\alpha 0}_{RL}(\varepsilon, r_R)\right] Y_L(\hat{r}_R) + \phi^{\alpha}_{RL}(\varepsilon, r_R). \tag{2.24}$$

The member of NMTO basis set $\chi^{N}_{R'L'}$ is constructed by Lagrange interpolation of $\phi^{\alpha}_{RL}(\varepsilon, r_R)$ evaluated at the energy points $\varepsilon_0, ..., \varepsilon_N$,

$$\chi^{N}_{R'L'} = \sum_{n=0}^{N} \sum_{RL} \psi^{N}_{RL}(\varepsilon_n, r_R) L^{N}_{n,RL,R'L'} \tag{2.25}$$

Thus the construction of basis set is energy selective, as well as localized in nature. The energy selective nature of the basis set provides the way to select a narrow energy window from full LDA band structure accurately. This procedure naturally takes into account the re-normalization effect due to the integrated-out orbitals by defining energy-selected, effective orbitals which serve as Wannier-like orbitals for the few-orbital Hamiltonian in the downfolded representation. The real-space representation of the downfolded Hamiltonian in the basis of downfolded NMTOs provide information on effective hopping, which we have used extensively in our first-principle study.

2.2.3 The Pseudopotential Method

Electrons at the outermost shell in an atom mostly take part in chemical bonding, and thereby control chemical and physical properties of the system. This leads to the idea behind the pseudopotential theory. Let us denote core and valance state of single-particle Kohn-Sham equation as ψ^c and ψ^v, respectively. A new set of single- particle valence states $\tilde{\phi}^v$ can be defined as,

$$\psi^v(\mathbf{r}) = \tilde{\phi}^v + \sum_c \alpha_c \psi^c(\mathbf{r}). \tag{2.26}$$

The coefficient α_cs are determined using the condition that ψ^c and ψ^v are orthogonal to each other. Using Eq. (2.26), one can write the Eq. (2.14) in a different form:

$$\left[-\frac{\hbar^2}{2m_e}\nabla^2 + V_{KS} + \sum_c (\varepsilon^v - \varepsilon^c)\,|\psi^c\rangle\langle\psi^c|\right]\tilde{\phi}^v = \varepsilon^v\tilde{\phi}^v. \tag{2.27}$$

The operator $V_{PS} \equiv V_{KS} + \sum_c (\varepsilon^v - \varepsilon^c)\,|\psi^c\rangle\langle\psi^c|$, represents a weak attractive potential and is called a pseudopotential. The new states $\tilde{\phi}^v$ obey a single-particle equation with a modified potential, but have the same eigenvalues ε^v as the original valence state ψ^v. This new set of valance states experience a weaker potential near the atomic nucleus, but the proper ionic potential away from the core region. Since it is the latter region in which the valence electrons interact to form bonds that hold the solid together, the pseudo- wavefunctions preserve all the important physics relevant to the behavior of the solid. The pictorial representation of construction of pseudo potential is shown in Fig. (2.4)

Since last few decades several attempts have been made to generate more accurate as well as more efficient pseudo-potentials, keeping the basic principles same. In norm-conserving pseudopotential [17] scheme, inside some core radius, the all electron (AE) wave function is replaced by a soft nodeless pseudo (PS) wave function, subject to the condition that within the chosen core radius the norm of the PS wave function has to be the same with the AE wave function and outside the core radius both the wave functions are identical. However, the charge distribution and moments of AE wave function are well reproduced by the PS wave function only when the core radius is taken around the outer most maximum of AE wave function. This in practice makes the situation for strongly localized orbitals like $3d$ and rare-earth elements, complicated as the resulting pseudopotentials require a large plane-wave basis set. This situation was remarkably improved by Vanderbilt [26] by introduction of ultra-soft pseudopotential. According to this scheme the norm conservation constraint was relaxed and a localized

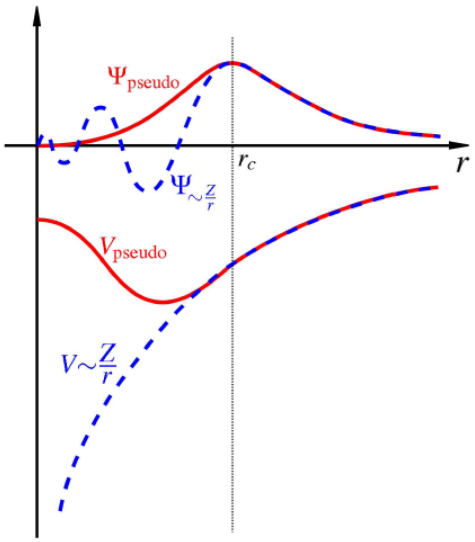

Figure 2.4 Construction of pseudo potential and pseudo wavefuction (red lines) out of full coulomb potential. Figure adapter from web:*http://en.wikipedia.org/wiki/Pseudopotential*

atom centered augmentation charge was introduced to make up the charge deficit. The augmentation charge is defined as the charge density difference between the AE and the PS wavefunction. Only for the augmentation charges, a small cutoff radius must be used to restore the moments and the charge distribution of the AE wavefunction accurately. The success of this particular approach is partly hampered by rather difficult construction of the pseudopotential.

2.2.4 The Linearized Augmented Plane Wave + local orbital method

The linearized version of Augmented Plane Wave (LAPW) basis, following the Anderson's linearization approach is, expressed as:

$$\chi_q(\mathbf{r},\varepsilon) = \begin{cases} \sum_{l,m}\left(A^q_{lm,R}\phi_{LR}(r_R,\varepsilon_v) + B^q_{lm,R}\dot{\phi}_{LR}(r_R,\varepsilon_v)\right) & \text{for } r_R \leq S_R, \\ e^{i(\mathbf{q}.\mathbf{r})} & \text{for } r_R > S_R \end{cases}$$

where the coefficients $A^q_{lm,R}$ and $B^q_{lm,R}$ can be determined by matching these two solutions in magnitude and slope at the sphere boundary. To do this, the plane wave solution in the interstitial is required to be expanded in terms of Bessel function $j_l(r_R,q)$. In principle a large number of l values are required for exact matching, but to keep the problem tractable one truncates this number at some value l_{max}.

Therefore in band structure calculations based on LAPW basis set a crucial parameter is l_{max}, for which a reasonable choice is needed. The condition that allows good choice of l_{max} is:

$$R_i K_{max} = l_{max} \tag{2.28}$$

where R_i is the the radius of i^{th} MT sphere and K_{max} determines the cut off for the plane wave. The accuracy of the basis is controlled by the quantity $R_i^{min} K_{max}$, where R_i^{min} is the smallest MT sphere radius in the unit cell.

In the original version of LAPW method the core states, those which do not participate in the chemical bonding, are treated as in free atom, but subject to the potential due to the valence states. The problem arises in order to treat semi core states, which lie in the boarder line between core and valence state. In order to solve this problem an additional set of basis functions is added. They are called "local orbital" [34] and consist of a linear combination of two radial functions at two different energies and one energy derivation at one of these energies:

$$\phi_{lm}^{LO} = \left[A_{lm,R}\phi_{LR}(r_R, \varepsilon_{v1}) + B_{lm,R}\dot{\phi}_{LR}(r_R, \varepsilon_{v1}) + C_{lm,R}\phi_{LR}(r_R, \varepsilon_v)\right]. \tag{2.29}$$

The coefficients are determined by the requirements that ϕ^{LO} should be normalized and should have zero value and vanishing slope at the sphere boundary. Though adding local orbitals increase the LAPW basis set size, still their number is quite small compared to typical LAPW basis set size of a few hundred functions.

The problem with the APW method was the energy dependence of basis set, which is removed in LAPW+LO method, but at the cost of somewhat larger basis set. Sjöstedt, Nordstrom and Singh [35] proposed the so called APW+lo method, in which the basis set is energy independent though still have the same size as in the APW method. In this sense, APW+lo combines the good features of APW and LAPW+LO method. The APW+lo basis set contains two kind of functions. The first kind is the standard APW basis with the partial wave evaluated at fixed energy ε_v. The other part of the basis is local orbital, which is defined differently from that used in connection with the LAPW method. We abbreviate this local orbital as 'lo' instead of 'LO' used in connection with LAPW. The local orbitals

are defined as;

$$\phi_{lm}^{lo} = \left[A_{lm,R}^{lo}\phi_{LR}(r_R,\varepsilon_{v1}) + B_{lm,R}^{lo}\dot{\phi}_{LR}(r_R,\varepsilon_{v1})\right]. \tag{2.30}$$

The coefficients are determined by normalization and by requiring that the local orbital has zero value at MT boundary and not zero slope. Hence, both the APW and the local orbital are continuous at the sphere boundary, but the first derivatives of both functions are discontinuous at the sphere boundary. This new scheme converges practically to identical result as LAPW method [36], but allows to reduce "$R_i^{min}K_{max}$" drastically, thus the corresponding computational time. The LAPW based computer code that has been used in the present study is Wien2k code [39].

2.2.5 The Projector-Augmented-Wave Formalism

P. E. Blöchl in 1994, developed the projector-augmented- wave (PAW) method, which combines the linear augmented plane wave method with the plane wave pseudopotential approach. This method turned out to be computationally elegant, transferable and accurate method for electronic structure calculation. Later Kresse and Joubert [37] modified this PAW method and implemented in plane wave based code of Vienna Ab initio Simulation Package (VASP) [31, 32, 33].

In this formalism, the AE wavefunction Ψ_n is derived from the PS wavefunction $\tilde{\Psi}_n$ by means of a linear transformation:

$$|\Psi_n\rangle = |\tilde{\Psi}_n\rangle + \sum_i \left(|\phi_i\rangle - |\tilde{\phi}_i\rangle\right)\langle\tilde{p}_i|\tilde{\Psi}_n\rangle. \tag{2.31}$$

The index i is a shorthand for the atomic site at $\mathbf{R_i}$. The all electron partial waves ϕ_i are the solutions of the radial Schrödinger equation for the isolated atom. The PS partial waves $\tilde{\phi}_i$ are equivalent to the AE partial waves outside a core radius r_c^l. These two wavefunctions match both in value and slope at the boundary r_c^l. The projector function $\tilde{p}_i$ for each PS partial wave localized within the core radius, obeys the relation $\langle\tilde{p}_i|\tilde{\phi}_j\rangle = \delta_{ij}$. From Eq. (2.31), the AE charge density in PAW method can be written as,

$$\rho(\mathbf{r}) = \tilde{\rho}(\mathbf{r}) + \rho^1(\mathbf{r}) - \tilde{\rho}^1(\mathbf{r}) \tag{2.32}$$

where $\tilde{\rho}$ is the soft pseudo-charge density calculated directly from the pseudo wavefunctions on a plane wave grid. The on-site charge densities ρ^1 and $\tilde{\rho}^1$ are treated on radial support grids that are localized around each atom. It should be mentioned that the charge density $\tilde{\rho}^1$ is exactly the same as ρ^1 within the augmentation spheres around each atom. In PAW approach, an additional density, called compensation

charge density is added to both auxiliary densities ρ^1 and $\tilde{\rho}^1$ so that the multi-pole moments of the terms $\rho^1 - \tilde{\rho}^1$ in Eq. (2.32) vanish. Thus the electrostatic potential due to these terms vanishes outside the augmentation spheres around each atom, just as is accomplished in LAPW method. Like density, the energy can also be written as a sum of three terms and by functional derivatives of the total energy, one can derive the expressions of Kohn-Sham equations. In the present thesis, the plane wave based results are obtained using PAW potentials.

2.3 Other advanced supporting techniques

The conventional DFT formalism has some shortcomings. For example, it can not take care of time variation, *i.e*, the dynamics, the strong electron-electron correlation effect which are some times very important in describing the system properties. Therefore apart from above mentioned basic electronic structure methods, in the present thesis we have employed some of the more advanced techniques. The descriptions of these techniques are given below.

2.3.1 Ab-initio Molecular Dynamics

Molecular Dynamics (MD) of many body system is a method which describe the dynamical evolution of the system in a microscopic level. For the solid state system molecular dynamics method generate configurations from dynamical evolution of atoms. The prime objective of any molecular dynamics is to solve the equations of motion, mainly Newton's equation of motion which of the form; $M_I\ddot{R}(t) = F_I(t) = -\nabla_I V(R_I(t))$, where $\ddot{R}(t)$ is the time derivative of coordinates, which can be related to the gradient of effective potential field in which the system evolves. In the last few decades enormous number of studies have been done on how to describe more efficiently and reliably the potential for the many atom systems. In principle, potential energy landscape can be calculated from full quantum mechanical calculations. In practice, it is not possible as discussed before. The classic and traditional way of approximating the potential is to determine the potential in advance. In this route the full many body interaction can be split into different parts in different ways depending on 2-body term, 3-body term etc. and also on the basis of long range-short range interaction. Taking into account these intuitive information, the potentials are represented by suitable empirical functional forms. Using this empirical

potential energy landscape the dynamics of the system is determined. In spite of huge success [40] of the empirical potential MD method in various cases like liquids, gas phases etc, it fails in a number of cases [41, 42]. These predefined empirical model potentials MD fails where electronic degrees of freedom plays very crucial role in the description of the system. Therefore a new route has been devised to handle the above mentioned shortcomings, by coupling the traditional MD with the ab-initio electronic structure calculation named as *"Ab-initio Molecular Dynamics"* (AIMD). The basic idea of ab-initio MD is to compute force on the nuclei from the electronic structure calculations for the generated dynamical configurations of nuclei, by treating electronic degrees of freedom quantum mechanically and nuclei degrees of freedom classically.

Therefore in this method the electronic degrees of freedom are treated actively, which capture the details of all electronic behavior as well as all sort of chemical complexity derived by electronic level. In the literature mainly three types of AIMD have been reported based on the way of generating the quantum many body potential by solving quantum electronic structure calculation. These methods are i) Ehrenfest MD, ii) Born-Oppenheimer MD and iii) Car-Parrinello MD.

2.3.1.1 Ehrenfest Molecular Dynamics

The full many body Hamiltonian contains both ionic and electronic degrees of freedom. In this scheme [43] using separation of variable technique the ionic and electronic degrees of freedom are separated out. For the electronic part we solve the time dependent Schrödinger equation for a particular configuration of nuclei, which can be expressed as,

$$i\hbar\frac{\partial\psi}{\partial t} = \mathscr{H}_e(r_i,R_I)\psi(r_i,R_I;t), \tag{2.33}$$

where, $\mathscr{H}_e$ is the full many body Hamiltonian with the K.E part of nuclei and $\psi(r_i,R_I;t)$ is the electronic part of the full wave function. The nuclear motion is treated classically in the field created by the quantum mechanical dynamics of electron and it can take the form as,

$$M_I\ddot{R}_I(t) = -\nabla_I\langle\mathscr{H}_e\rangle = -\nabla_I V_e^E. \tag{2.34}$$

Therefore Ehrenfest MD method can be summarized as follows ::

a) The electronic Hamiltonian $\mathscr{H}_e$ is depends parametrically on the instantaneous nuclear position R_I

and t and it is time dependent via nuclear propagation $R_I(t)$.

b) The connection between classical and quantum mechanical degrees of freedom are established in a mean field way.

c) Time evolution of nuclei are dictated by Newtons law of motion in a mean field created by the electron whereas the electrons evolves according to time dependent Schrödinger equation.

d) It is a hybrid method of classical and quantum mechanical approach.

2.3.1.2 Born-Oppenheimer Molecular Dynamics

Born and Oppenheimer proposed an alternative way [1] to solve coupled electron-nuclei wave equation by treating electron completely time independently at each time configuration of nuclei. That means we have to solve the time independent Schrödinger equation for electrons at each molecular dynamics step of time varying nuclear positions. Mathematically it can be written as;

$$\mathscr{H}_e\psi_0 = E_0\psi_0; E_0 \equiv E_0(R_I), \tag{2.35}$$

$$M_I\ddot{R}_I(t) = -\nabla_I \min_{\psi_0}\langle\psi_0|\mathscr{H}_e|\psi_0\rangle. \tag{2.36}$$

So in summary ::

a) The effective potential energy is obtained from the time independent electronic part for a particular nuclei configuration.

b) Here ψ is no longer intrinsically time dependent. It is assumed that electronic degrees of freedom follow adiabatically the classical nuclear motion.

2.3.1.3 Car-Parrinello Molecular Dynamics

Car-Parrinello MD (CP-MD) [44, 45] is a combined approach of both Ehrenfest MD and B-O MD scheme. In CP-MD we have to solve the nuclear motion classically over large time scale set by the nuclear motion time. On top of that we have to take into account evolution of intrinsic quantum mechanical electronic part. In order to handle this mixed quantum/classical mixed problem the route is to map this two component problem into one component problem with two different energy scales. Instead of Hamiltonian in the previous cases, in this method we deal with the corresponding Lagrangian

involving both nuclear and electronic part ;

$$\pounds^{CP} = \sum_I \frac{1}{2} M_I \dot{R}_I^2 + \sum_i \mu_i \langle \dot{\psi}_i | \dot{\psi}_i \rangle - \langle \Psi_0 | \mathscr{H}_e | \Psi_0 \rangle + \sum_{ij} \Lambda_{ij} (\langle \psi_i | \psi_i \rangle - \delta_{ij}), \tag{2.37}$$

where, the first two term of Eq. (2.37) are the K.E of nuclei and electronic part respectively. 3rd term is the potential energy and the 4th term is the constraint involved in the Lagrangian. μ is the fictitious mass involving with electronic degrees of freedom. The corresponding Lagrange equation of motion for nuclei;

$$M_I \ddot{R}_I(t) = -\frac{\partial}{\partial R_I} \langle \Psi | \mathscr{H}_e | \Psi \rangle, \tag{2.38}$$

and for the electronic part;

$$\mu_i \ddot{\psi}_i(t) = -\frac{\delta}{\delta \langle \psi_i |} \langle \Psi_0 | \mathscr{H}_e | \Psi_0 \rangle + \sum_j \Lambda_{ij} \psi_j. \tag{2.39}$$

2.3.2 AIMD followed in this study

The main disadvantage of CP-MD scheme lies in the fact that the calculation of force acting on the nuclei os taken into account. The force acting on the nuclei can be calculated by *Hellmann-Feynman* [46] force theorem of the form; $F_I^{HF} = -\langle \Psi_0 | \nabla_I \mathscr{H}_e | \Psi_0 \rangle$, where, Ψ_0 is an exact eigen function corresponding to the Hamiltonian $\mathscr{H}_e$. In both CP-MD and Ehrenfest MD method the expectation values of the Hamiltonian $\mathscr{H}_e$ are not minimized with respect to the wave function. Therefore in both of these cases the force is calculated with respect to the non self consistent wave function, which leads to some additional non self consistent force terms in the calculation. Whereas in the case of Born-Oppenheimer MD the electronic wave function of the Schrödinger equation is calculated at each ionic configuration and the force at each step is calculated by minimizing the $\mathscr{H}_e$ with respect to the exact eigen function. Therefore the unwanted contribution in the force are eliminated automatically in Born-Oppenheimer MD. Moreover in both Ehrnfest MD and CP-MD one have to simultaneously integrate the coupled equation of motion of electrons and nuclei, whereas in the case of Born-Oppenheimer case there are no explicit electron dynamics, so one needs to integrate over one time scale dictated by the nuclear motion. This is a huge advantages of Born-Oppenheimer method over CP-MD method. In respect of computational time, this Born-Oppenheimer MD can be made as fast as that of CP-MD at the expense of energy conservation [47]. However by suitable choice of ensemble the problem of energy conservation can be

avoided and as far as the convergence of wave function and energy is concerned this problem is not so serious.

Therefore in the present thesis we adopted the Born-Oppenheimer approach to include the finite temperature effect in the calculation. In the case of DFT based AIMD within the formalism given by Born-Oppenheimer the Eq. (2.35) and Eq.(2.36) takes the following form;

$$\mathscr{H}_e^{KS}\psi_0 = E_0^{KS}\psi_0; E_0^{KS} \equiv E_0^{KS}(R_I), \tag{2.40}$$

$$M_I\ddot{R}_I(t) = -\nabla_I \min_{\psi_0}\langle\psi_0|\mathscr{H}_e^{KS}|\psi_0\rangle, \tag{2.41}$$

where, H_e^{KS} is the Kohn-Sham energy functional and ϕ is the Kohn-Sham orbitals.
Therefore in the implementation of the above scheme in practice, main task is to separate the nuclear and electronic motion. The basic requirements are that the fictitious temperature associated with the electronic motion should remain low compared to the nuclear motion. These above requirements can be achieved by proper choice of time step and thermostat in the simulation.

2.3.3 Dynamical Mean Field Theory

The other short coming of DFT is the treatment of electron-electron correlation, which is treated in average manner in DFT. Although such a prescription is highly successful for most of the cases, but it fails when electron-electron correlation become strong as for d and f electron systems. Therefore the most obvious choice to deal with this problem is to couple the LDA low energy Hamiltonian with the missing correlation part, which defines many body Hamiltonian, such as Hubbard model [48], Heisenberg Model, t-J model etc but now derived in an ab-initio way. The constructed model then can be solved with *Dynamical Mean Field Theory* (DMFT) [49]. DMFT is non-perturbative method to take care of the electronic interaction beyond the independent electron approximation. It maps the non-tractable many body lattice model to the local quantum impurity model which can be solved by Quantum Monte Carlo, Exact Diagonalization methods.

The effective self consistent quantum impurity model, deals with a set of local quantum mechanical

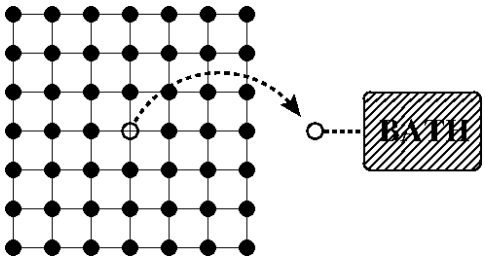

Figure 2.5 Schematic representation of: full many body lattice problem is mapped onto single impurity problem attached with the self consistent bath.

degree of freedom that interacts with a bath created by all other degree of freedom on other site as shown in Fig. (2.5). This approximation is exact in infinite dimension. In the combined LDA+DMFT approach the one particle input of DMFT Hamiltonian comes from LDA band structure calculations, which is an useful methodology to take care of material specific aspect. The corresponding local Green's function is calculated via the Dyson equation, which has the form,

$$G(\omega_n) = \sum_k \left[(\omega_n + \mu)I - H^{LDA}(k) - \Sigma(\omega_n)\right]^{-1}, \tag{2.42}$$

where, $H^{LDA}(k)$ is the LDA few band Hamiltonian defined in Wannier function basis. μ is the chemical potential calculated self consistently via total number of electron. ω_n are the Matsubara frequencies related to the temperature ($\beta = 1/T$) via the relation $\omega_n = \frac{(2n+1)\pi}{\beta}$. Σ is the self energy matrix related to local and bath green's function via the following relation;

$$\Sigma = g^{-1} - G^{-1} \tag{2.43}$$

The local Green's function therefore has to be calculated self consistently with the condition that implies the local Green's function to be the same as the corresponding solution of the quantum impurity problem.

The LDA+DFMT self consistent flowchart is shown in Fig. (2.6). The first step is to guess the value of the input Σ and then calculate g from Eq. (2.42) and (2.43). The next step is the main part of the self consistent cycle, *i.e* to get the solution of the quantum impurity problem. Once the impurity problem

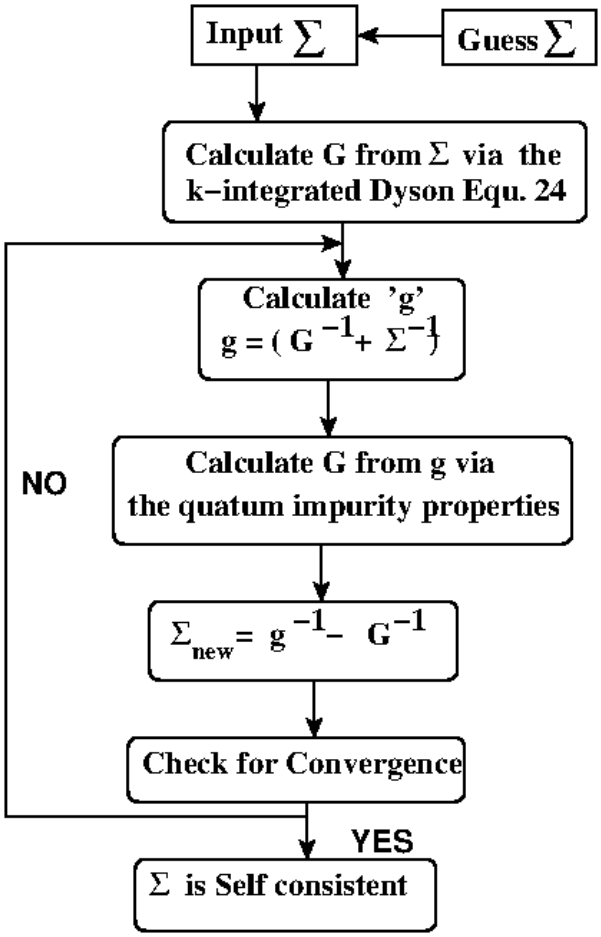

Figure 2.6 Schematic flow chart of self consistent cycle of DMFT.

is solved, we get G, together with yields a new Σ from Eq.(2.43). In the present thesis we have used Quantum Monte Carlo as the impurity solver which is numerically an exact method.

Bibliography

[1] M. Born, and J. R. Oppenheimer, Zur Quantentheorie der Molekeln, Ann. Physik **84**, 457 (1927).

[2] D. R. Hartree, The wave mechanics of an atom with non-coulombic central field: parts I, II, III, Proc. Cambridge Phil. Soc. **24**, 89, 111, 426 (1928).

[3] V. Fock, Naherungsmethode zur Losung des quanten-mechanischen Mehrkorperprobleme, Z. Phys. **61**, 126 (1930).

[4] P. Hohenberg and W. Kohn, Phys. Rev. **136**, B864 (1964).

[5] W. Kohn and L. J. Sham, Phys. Rev. **140**, A1133 (1965).

[6] R. G. Parr and W. Yang, Density-Functional Theory of Atoms and Molecules (Oxford University Press, Oxford, (1989), R. M. Dreizler and E. K. U. Gross, Density Functional Theory (Springer, Berlin, 1990).

[7] D. M. Ceperley and B. J. Alder, Phys. Rev. Lett. **45**, 566-569 (1980).

[8] J. P. Perdew and A. Zunger, Phys. Rev. B **23**, 5048-5079 (1981).

[9] U. v. Barth and L. Hedin, J. Phys. C: Solid State Phys. **5**, 1629-1642 (1972).

[10] S. H. Vosko, L. Wilk, and M. Nusair, Canadian Journal of Physics **58**, 1200-1211 (1980).

[11] J. P. Perdew and W. Yue, Phys. Rev. B **33**, 8800-8802 (1986).

[12] J. P. Perdew, K. Burke, and M. Ernzerhof, Phys. Rev. Lett. **77**, 3865-3868 (1996).

[13] A. D. Becke, Phys. Rev. A **38**, 3098-3100 (1988).

[14] C. Lee, W. Yang, and R. G. Parr, Phys. Rev. B **37**, 785-789 (1988).

[15] J. P. Perdew, J. A. Chevary, S. H. Vosko, K. A. Jackson, M. R. Pederson, D. J. Singh, and C. Fiolhais, Phys. Rev. B **46**, 6671-6687 (1992).

[16] B. Hammer, L. B. Hansen, and J. K. Nörskov, Phys. Rev. B **59**, 7413-7421 (1999).

[17] D. R. Hamann, M. Schlüter, and C. Chiang, Phys. Rev. Lett. **43**, 1494-1497 (1979).

[18] Z. Wu and R. E. Cohen, Phys. Rev. B **73**, 235116 (2006).

[19] J. C. Slater and G. F. Koster, Phys. Rev. **94**, 1498 (1954).

[20] J. C. Phillips and L. Kleinman, Phys. Rev. **116**, 287 (1959).

[21] E. P. Wigner and F. Seitz, Phys. Rev. **46**, 509 (1934).

[22] T. L. Loucks, Augmented Plane Wave Methods, (Benjamin, New York, 1967).

[23] O. K. Andersen, Phys. Rev. B **12**, 3060-3083 (1975).

[24] J. Korringa, Physica **13**, 392 (1947); J. Korringa, Phys. Rev. **238**, 341 (1994).

[25] A. Kasten, P.H. Müller, M. Schienle, Solid State Comm. **51**, 919 (1984).

[26] D. Vanderbilt, Phys. Rev. B **41**, 7892 (1990).

[27] G. Kresse and J. Hafner, J. Phys.: Condens. Matter **6**, 8245 (1994).

[28] O. K. Andersen and O. Jepsen, Phys. Rev. Lett. **53**, 2571-2574 (1984).

[29] O. Andersen, Phys. Rev. B **8**, 3060 (1975).

[30] O. K. Andersen and T. Saha-Dasgupta, Phys. Rev. B **62**, R16219 (2000).

[31] G. Kresse and J. Hafner, Phys. Rev. B **47**, 558 (1993).

[32] G. Kresse and J. Hafner, Phys. Rev. B **49**, 14251 (1994).

[33] G. Kresse and J. Furthmüller, Phys. Rev. B **54**, 11169 (1996).

[34] D. Singh, Phys. Rev. B **43**, 6388-6392 (1991).

[35] Sjöstedt, Nordstrom and Singh, Solid State Commun, **114**, 6388 (1991).

[36] O. Jepsen, J. Madsen, and O. K. Andersen, Phys. Rev. B **18**, 605-615 (1978).

[37] G. Kresse and D. Joubert, Phys. Rev. B **59**, 1758 (1999).

[38] P. E. Blöchl, Phys. Rev. B **50**, 17953 (1994).

[39] P. Blaha, K. Schwarz, G. Madsen, D. Kvasnicka, and J. Luitz, in WIEN2k, An Augmented Plane Wave + Local Orbitals Program for Calculating Crystal Properties.

[40] G. C. Schatz, Rev. Mod. Phys. **61**, 669 (1989), C. G. Gray and K. E. Gubbins, Theory of Molecular Fluids Vol. 1 (Oxford, Clarendon, 1984), M. Sprik, in Computer Simulation in Chemical Physics, eds. M. P. Allen and D. J. Tildesley (Kluwer, Dordrecht, 1993).

[41] D. K. Remler and P. A. Madden, Molec. Phys. 70, 921 (1990).

[42] M. C. Payne, M. P. Teter, D. C. Allan, T. A. Arias, and J. D. Joannopoulos, Rev. Mod. Phys. **64**, 1045 (1992).

[43] P. Ehrenfest, Z. Phys. **45**, 455 (1927).

[44] R. Car and M. Parrinello, Phys. Rev. Lett. **55**, 2471 (1985), R. Car and M. Parrinello, Solid State Commun. **62**, 403 (1987).

[45] R. Car, M. Parrinello, and M. Payne, J. Phys.: Condens. Matter **3**, 9539 (1991), R. Car, in Monte Carlo and Molecular Dynamics of Condensed Matter Systems, Chapt. 23, p. 601, eds. K. Binder and G. Ciccotti (Italien Physical Society SIF, Bologna, 1996).

[46] R. P. Feynman, Phys. Rev. **56**, 340 (1939); H. Hellmann, Z. Phys. **85**, 180 (1933).

[47] D. A. Gibson, I. V. Ionova, and E. A. Carter, Chem. Phys. Lett. **240**, 261 (1995).

[48] J. Hubbard, "Electron Correlations in Narrow Energy Bands". Proceedings of the Royal Society of London **276**, 238-257 (1963).

[49] A. Georges, G. Kotliar, W. Krauth and M. Rozenberg, Rev. of Mod. Phys. **68**, (13) (1996).

Chapter 3

First principle study of 4-*d* perovskite ruthenates*

3.1 Back ground and Motivation of the present study

Complex perovskite ruthenates form fascinating field of research in recent times. These perovskite ruthenates are part of a larger interesting class of materials, known as Ruddlesden-Popper Series [1], which is an infinite layer system of general formula $Sr_{n+1}Ru_nO_{3n+1}$ (n=∞). $SrRuO_3$ is a member of this huge class of materials and it first attracted attention of the research community by its unusual itinerant ferromagnetism, observed in 1959 by Randall and Ward [2]. Very recently $SrRuO_3$ has become a very interesting topic of research because of the discovery of unusual superconductivity in the layered ruthenates, Sr_2RuO_4 which is also a member of this series [7, 8]. Recent studies show that at low temperature $SrRuO_3$ is a Fermi liquid while at high temperate it shows bad metallic behavior. $SrRuO_3$ is the only ferromagnetic metal among 4-*d* oxides [9, 10]. Alloy of this system, substituted Ca in place of Sr, $Sr_xCa_{1-x}RuO_3$ also attracts attention due to the paramagnetic nature of $CaRuO_3$ [12, 14] and the intriguing properties of $CaRuO_3$ which at low temperature shows non-Fermi liquid [15, 17] like behavior.

It is a puzzle that $SrRuO_3$ (SRO) is a metallic compound exhibiting long range ferromagnetic ordering with curie temperature T_c=165 K [9, 10], whereas $CaRuO_3$ (CRO) is a similar isostructural,

*This chapter is based on *Phys. Rev. B* **82**, *094440 (2010)* and *Phys. Rev. B 83, 041103(R) (2011)*

isovalent compound but shows huge difference in the physical properties. $CaRuO_3$ is metallic with, similar room temperature conductivity, similar high temperature magnetic moment as $SrRuO_3$, but no long range ordering have been found down to lowest temperature of 1.8 K [15]. These system have been probed by various experimental techniques such as x-ray and ultraviolet photoemission spectroscopy (PES) [18, 19], transport measurements, [13] optical conductivity measurements [20] and specific-heat measurements [21]. The photoemission measurements show temperature induced structural modifications in $CaRuO_3$ but an insignificant one in case of $SrRuO_3$. Electron-phonon coupling is found to be weaker for $SrRuO_3$ than $CaRuO_3$. The experimental results point to the role of A-site element in the properties of these perovskites as well as some role of electron-electron correlation, though the strength and the extent of its importance still remains debatable and unclear.

The motivation of the present study is two fold. First of all the observed varied magnetic ground states of $SrRuO_3$ and $CaRuO_3$ do not follow the common wisdom. The electronic and magnetic properties of these transition metal oxide systems are believed to be governed by the transition metal units, which is Ru in the present case. The nonmagnetic A-cation such as Sr/Ca is believed to give stability of the crystal structure with out taking part directly in the determination of physical properties of these systems. The case of $SrRuO_3$ and $CaRuO_3$, shows exception to this common thinking where Sr/Ca plays crucial role in the determining the ground state magnetic properties. Though there exists some hints of structural modification happening as one goes from Sr to Ca compound, but direct study probing the role that of Sr in the magnetic transition does not exist. Secondly, the role and impact of any electron-electron correlation effect in the 4-*d* Ru based transition metal systems needs to be explored. In the present chapter we wish to understand the role of A site cation and its coupling to magnetism as well as the effect of electron-electron correlation from microscopic point of view, using density functional theory based band structure calculations in conjunction with dynamical mean theory for the later investigation.

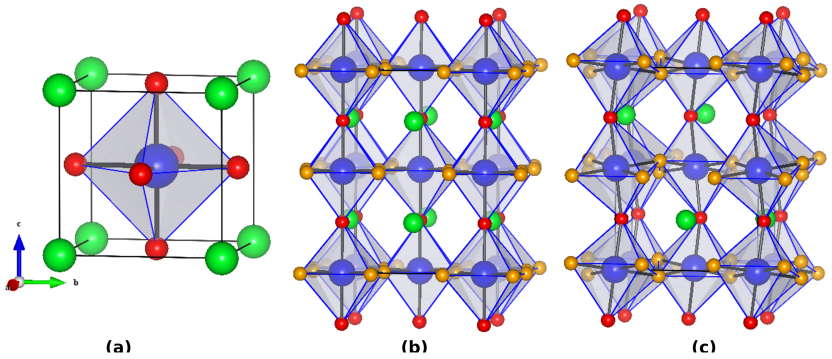

Figure 3.1 Crystal structure of $SrRuO_3$ forming in perovskite structure. (a) Cubic phase, (b) tetragonal phase and (c) orthorombic phase. RuO_6 (blue ball) units are shown by shaded octahedra. Sr (green ball) atoms sit in the hollow formed by corner-shared RuO_6 units. The oxygen atoms at the apical positions of the RuO_6 octahedra are labeled as O1 (red ball) and those at the plane are labeled as O2 (orange ball).

3.2 Results and Discussions

3.2.1 Crystal Structural

Experimental studies suggest that starting from low temperature to high temperature $SrRuO_3$ (SRO) exists in three different crystal structures. At room temperature $SrRuO_3$ crystallizes in a orthorhombic structure of space group *Pnma*. On increasing the temperature further, the structure goes to tetragonal structure of space group *I4/mcm* around 550 K followed by the cubic structure of space group *Pm3m* at around 680 K. The three crystallographic phases are shown in Fig. (3.1). In the present study we are interested particularly in the room temperature phase *i.e* the orthorhombic phase. Both $SrRuO_3$ and $CaRuO_3$ (CRO) at room temperature crystallize in a distorted orthorhombic structure with four formula unit per cell. The basic building block of the structure are the RuO_6 octahedral units connected by sharing the corners and Sr/Ca sit in the void position of the structure giving stability to the structure. The distortion of the structure is $GdFeO_3$ type distortion which is characterized by the tilting and rotation of the octahedral unit as shown in Fig. (3.2). The selected bond lengths and bond angles of $SrRuO_3$ and $CaRuO_3$ are shown in Table. 3.1. From the structural information it is evident that both $SrRuO_3$ and $CaRuO_3$ not only have the $GdFeO_3$ type distortion, in addition to this it has the Jahn-Taller distortion characterized by difference in bond lengths and bond angles which deviate from ideal

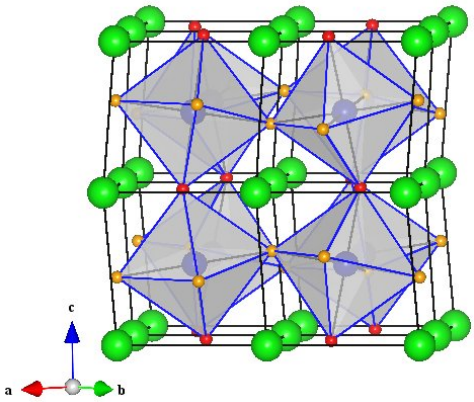

Figure 3.2 Representative figure of orthorhombic distortion, namely $GdFeO_3$ type distortion, characterized by tilting and rotation of RuO_6 (shaded polyhedra) octahedral unit. Color conventions are same as that of previous figure.

Table 3.1 Selected bond lengths and bond angles for $SrRuO_3$ and $CaRuO_3$

	$SrRuO_3$	$CaRuO_3$
Bong Lengths	Ru-O1=1.97 Å	Ru-O1=2.05 Å
	Ru-O2=2.03 Å	Ru-O2=1.98 Å
	Ru-O2=1.94 Å	Ru-O2=1.97 Å
	Sr-O1=2.63 Å	Ca-O1=3.66 Å
	Sr-O2=3.10 Å	Ca-O2=3.39 Å
Bond Angles	$\angle$O2-Ru-O2=90.9^o	$\angle$O2-Ru-O2=90.5^o
	$\angle$O1-Ru-O2=89.9^o	$\angle$O1-Ru-O2=79.7^o
	$\angle$Ru-O2-Ru=161.1^o	$\angle$Ru-O2-Ru=151.1^o
	$\angle$Ru-O1-Ru=164.9^o	$\angle$Ru-O1-Ru=137.6^o

180^o. In the $GdFeO_3$ kind of orthorhombic distortion A site cation (Sr/Ca) pulls each O1(O2) closer to one(two) of its four nearest 'A' neighbors. This introduces four nearest neighbors to 'A' out of 12 oxygen neighbors in the cubic phase, as shown in the Fig. (3.2). In addition, the Sr/Ca cube gets distorted making one body diagonal shortest. The distortion around Ru, reflected in the differences of Ru-O bond lengths, includes the difference of in plane, Ru-O2 and out of plane, Ru-O1 bond lengths as well as the in-plane Jahn-Teller distortion which makes four of the Ru-O2 bond lengths divided into two groups. If we further analyze the crystal structure of both $SrRuO_3$ and $CaRuO_3$, we find that the for $SrRuO_3$, the in-plane ∠Ru-O2-Ru is 161.1^o and the out-of-plane ∠Ru-O1-Ru is 164.9^o. When the Sr ion is replaced by smaller size cation Ca, the structure gets modified due to the changed A-O covalency, leading to further reduction in the in plane and out of plane ∠Ru-O-Ru, viz. 151.1^o and 167.6^o respectively. The larger distortion in case of $CaRuO_3$ compared to $SrRuO_3$, leads to modification of the electronic structure. We will discuss this structural distortion in more details in the subsequent sections.

3.2.2 Electronic Structure

In order to analyze the electronic behavior of this system we carried out DFT based calculation within the spin polarized Generalized Gradient Approximation (GGA) [3] by employing linear muffin tin orbital (LMTO) method [4, 5, 6]. The calculated density of states (DOS) of spin polarized $SrRuO_3$ is shown in the Fig. (3.3). The plotted DOS are projected onto Sr-*d*, Ru-*d* and O-*p* states. The well-studied electronic structure of SRO, consists of O-*p* Ru-*d* hybridized band structure that extends from about -8 eV below the Fermi level (E_f) to about 6 eV above E_f. The empty Sr bands lie higher up, above 6 eV. The Ru-*d* dominated states, separated by a dip-like feature from O-*p* dominated states in the density of states (DOS), give rise to a *d* band width of about 8.5 eV. Replacement of Sr by Ca, causing a reduction of the Ru-O-Ru angle, results in a clear gap between O-*p* dominated states and Ru-*d* dominated states as well as a reduction of width associated with Ru-*d* dominated states to about 7.5 eV. The obtained spin magnetic moments centered at different sites for SRO and CRO are listed in Table. 3.2. The octahedral coordination of Ru ions by oxygens, leads to splitting of five fold degenerate Ru-*d* bands into t_{2g} and e_g levels for both SRO and CRO. The positive and negative values of density of states in each panels in DOS plots denotes majority and minority spin channels. For the case of SRO

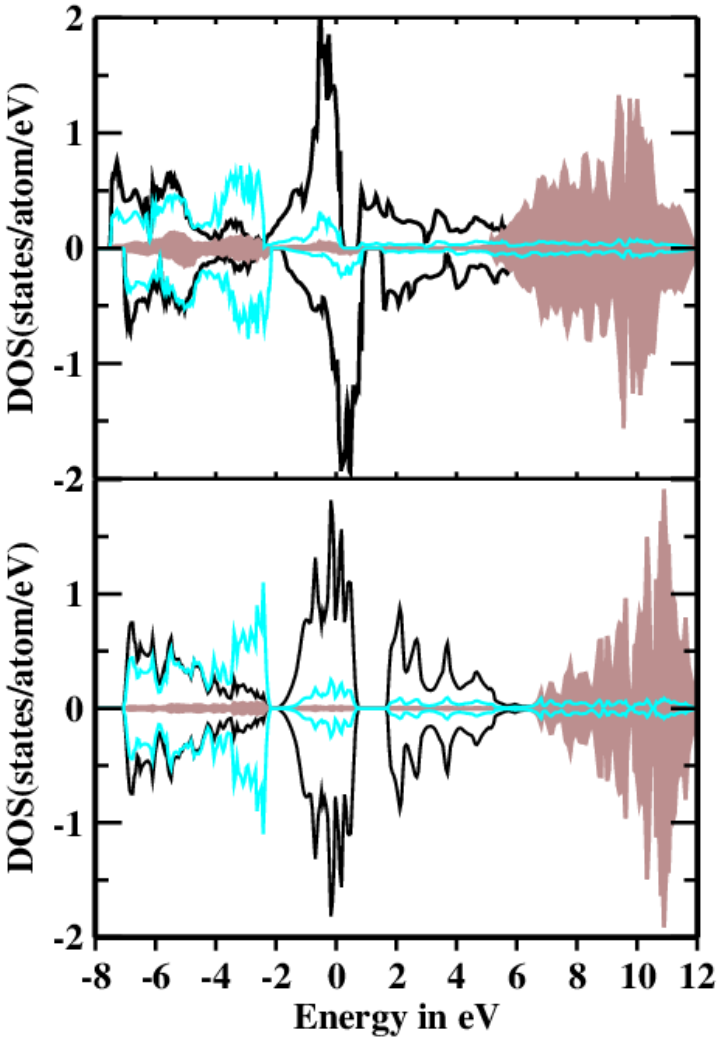

Figure 3.3 LDA density of states of $SrRuO_3$ (upper panel) and $CaRuO_3$ (lower panel). The DOS projected onto O-*p*, Ru-*d* and Sr/Ca-*d* are shown with cyan, black and shaded lines. For CRO this leads to a nonmagnetic solution with identical DOS between spin-up and spin-down channels.

Table 3.2 Magnetic moments at different sites for $SrRuO_3$ and $CaRuO_3$ from LDA calculations

	$SrRuO_3$	$CaRuO_3$
Sr/Ca	0.02 μ_B	0 μ_B
Ru	1.18 μ_B	0 μ_B
O1	0.13 μ_B	0 μ_B
O2	0.12 μ_B	0 μ_B
Total/formula unit	1.62 μ_B	0 μ_B

(upper panel of Fig. (3.3)) the majority spin channel of the Ru-t_{2g} are completely filled and minority spin channel of the Ru-t_{2g} are partially filled, whereas the Ru-e_g states are totally empty in both the spin channels. Therefore electronic configuration of low spin Ru^{+4} is $t^3_{2g} \uparrow t^1_{2g} \downarrow$. The spin magnetic moment at Ru sites is found to be about 1.18 μ_B which is substantially small compared to the spin only value of 2 μ_B corresponding to four electrons in the t_{2g} orbital in the low spin configuration of Ru^{4+}. The induced spin moment at the oxygen sites are found to be significantly large being 0.13 μ_B for O1 and 0.12 μ_B for O2. Thus, the total spin magnetic moment per formula unit is found to be about 1.6 μ_B and is very close to the experimental estimation from various measurements [10]. The reduction of local moment from the spin only value of 2 μ_B can be justified by the large O-*p* Ru-*d* bandwidth, which may reduce the magnetic moment. On the other hand for CRO case, the DFT calculation converges to the nonmagnetic solution with zero magnetic moment at all sites as is evident from the density of sates plots (bottom panel of Fig. (3.3). This is in agreement with the paramagnetic behavior with no long range magnetic ordering observed in the experimental measurements [15].

3.2.3 Structural Optimization

To understand the role of nonmagnetic A site element Sr/Ca in influencing the magnetic property via the magneto-structural coupling, which has been pointed out before, [25] we carried out structural optimization in presence and absence of magnetic ordering in terms of non spin-polarized and spin-polarized calculations using Vienna ab initio simulation package (VASP) [22]. The exchange-correlation functional was chosen to be that of generalized gradient approximation [3]. The optimized

Table 3.3 Relative changes in the distortion of Sr-O, Sr-Sr, and Ru-O bonds in absence and presence of magnetic ordering.

Environment	Stru. with mag. off (Å)	Stru. with mag. on (Å)	Relative change %
Δ(Sr-O1)	0.37	0.33	11.4
Δ(Sr-O2)	0.35	0.31	12.1
$\Delta(Sr-Sr)_{diag}$	0.27	0.29	6
$\Delta(Sr-Sr)_{edge}$	0.07	0.08	13
Δ(Ru-O)	0.01	0.01	0

geometries were obtained by full relaxation of the atomic positions and the lattice constants. The spin-orbit interaction at Ru site was included in the calculations in scalar relativistic form as a perturbation to the original Hamiltonian. The positions of the ions were relaxed toward equilibrium until the Hellmann-Feynman forces become less than 0.001 eV/Å.

In Table. 3.3, we list the calculated distortion of Sr-O bond lengths, $\Delta(Sr-O)$, Sr-Sr bond lengths, $\Delta(Sr-Sr)$ and Ru-O bond lengths, $\Delta(Ru-O)$ for the optimized geometries obtained in absence and presence of magnetic ordering. The relative change is the change in Δ's between two optimized geometries has been also listed. Δ(Sr-O) were measured by shortening of the shortest Sr-O bond relative to the average. The $\Delta(Sr-Sr)_{diag}$ is measured by shortening of the shortest Sr-Ru-Sr body diagonal of the Sr cube from the average and $\Delta(Sr-Sr)_{edge}$ is the difference between the shortest and longest Sr-Sr bond lengths along the cube edge. Δ(Ru-O) is defined by the difference between Ru-O2 and Ru-O1 bond lengths.

It is evident that while the changes in $\Delta(Sr-O1)$ and $\Delta(Sr-O2)$ are as big as 11-12% and that of $\Delta(Sr-Sr)$ are 6-13%, the distortion of the RuO_6 octahedra remains unchanged upon switching the magnetism on and off. This clearly suggests that the effect of magnetism is felt mostly by the nonmagnetic A site elements, Sr or Ca, not by the transition metal Ru. To understand this magneto-structural coupling derived covalency effect between A site with oxygen further, we calculate localized Wannier function for occupied part of O-2p, by NMTO downfolding technique [5], keeping only the O-p states active and integrating out all other Ru and Sr degrees of freedom, so that we can get truly minimal basis set that spans only the O-2p bands. In Fig. (3.4), we show the plot of such Wannier

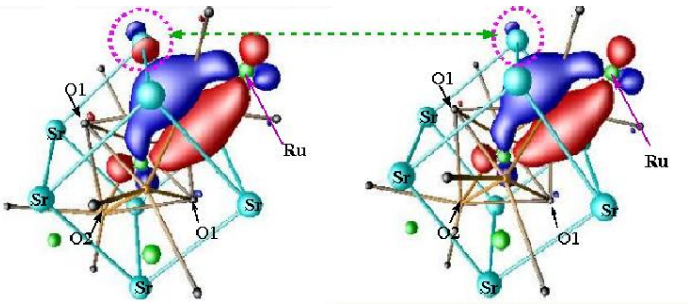

Figure 3.4 Wannier functions of the O-*2p* NMTO's calculated for optimized geometries with magnetization off (left panel) and magnetization on (right panel). The orbital shapes (constant amplitude surfaces) with lobes of opposite signs are labeled by red and blue colors respectively.

functions centered at one of the O2 oxygen in the two optimized geometries; one obtained in absence of magnetism and another in its presence. The central part of the Wannier functions has p_y character while the tails exhibit the covalency effect with the neighboring Ru atoms and Sr atoms. The relatively strong covalency effect between 4-*d* element Ru and O is seen in tails shaped as Ru t_{2g} residing at two neighboring Ru sites, which remain practically unchanged between two Wannier functions. The tail sitting at the Sr position with shortest O2-Sr bond length, however, shows significant changes in its relative weight between the two Wannier functions (shown by encircled region). It is to be stressed here that one should focus on the relative changes rather than the absolute magnitudes. While the magnitude of Ru-O covalency is much larger than that of Sr-O covalency, it is the Sr-O covalency that changes upon switching on/off the magnetic ordering.

3.2.4 Experimental Evidence

Our theoretical finding has been verified in terms of experimental measurements. For that, the evolution of the structural parameters of $SrRuO_3$ and associated disorder as a function of temperature was measured using x-ray absorption fine structure (XAFS). XAFS is one of the best known method for probing the element specific local environments, such as magnetic Ru, non-magnetic Sr. XAFS data at Sr K edge (16.105 keV) and Ru K edge (22.117 keV) were collected. For details see Ref. [26].

The measured bond length variation as well as Debye Waller Factors (DWFs) are shown in Fig.

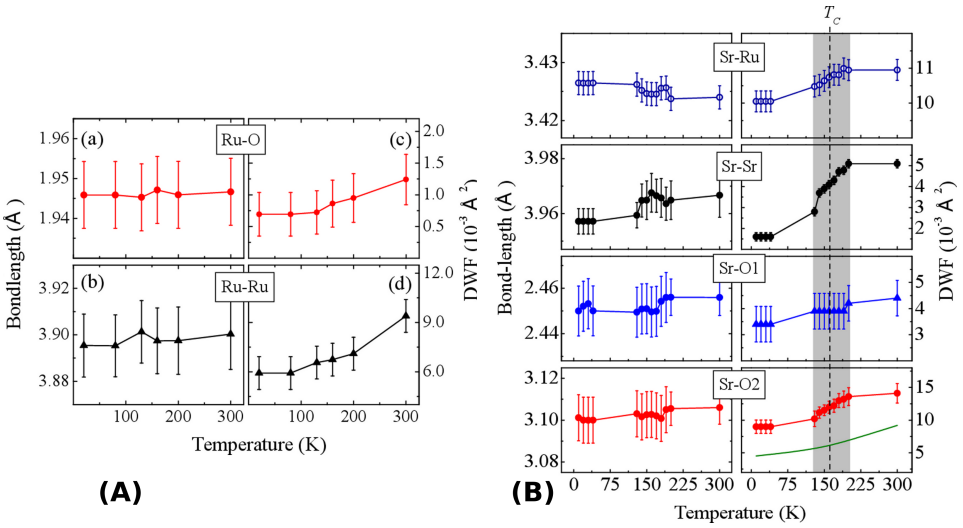

Figure 3.5 Temperature dependence of the bond lengths and corresponding Debye-Waller factors for the structural units around (A) Ru sites; (B) Sr site.

(3.5). The left panel of Fig. (3.5)(A) show that the Ru-O bond length does not exhibit significant change with temperature, the average values being about 1.94 Å, and the small increase may be related to the thermal expansion. The DWF corresponding to Ru-O bonds are shown in right panel of Fig. (3.5)(A), which show a very low static value. Increase in temperature leads to a small and gradual rise in magnitude of DWF demonstrating rigidity of the Ru-O octahedra. On the other hand the results obtained from Sr *K*-edge data as shown in the Fig. (3.5)(B), show opposite trend. The different Sr related bond lengths with the surrounding atoms, such as nearest neighbor O1 and O2, Ru show strong variation across the scanned temperature region. More over the DWF shows large variation with temperature for all the Sr related bond lengths exactly in the neighborhood of magnetic transition temperature which is 165 K, as marked by the shaded region of the Fig. (3.5)(B). Therefore experimental results also suggest that across the magnetic transition the changes in the Sr related structural environments are much more pronounced than that of the Ru related structural environments.

The above theoretical and experimental results, put together, clearly suggest that the Sr plays a very crucial role in magnetism via the change in Sr-O covalency effect, which in turn is the key factor in determining the Ru-O-Ru bond angle and the $GdFeO_3$ kind of distortion observed in these classes of materials, pointed out by Goodenough long ago [23]. Since the Ru-Ru exchange coupling depends

strongly on Ru-O-Ru bond angle, it is expected to be influenced by the Sr-O covalency. The DFT optimization shows Ru-O-Ru angle to changes by about 3^o upon switching on the magnetism. Individual RuO_6 octahedra, on the other hand, plays the role of magnetic centers and not the mediator of inter-site magnetic couplings, and presumably, is insensitive to magnetic ordering. This finding indicates that the magneto-structural coupling is mediated by the Sr ion, while normally one would expect Sr to play the role of a spectator.

3.2.5 Electron-electron correlation effect in Sr/CaRuO$_3$

Our motivation for the second part of the study on ruthenates is to explore the importance of electron-electron correlation in 4*d* transition metal oxides like $SrRuO_3$ and $CaRuO_3$. A possible scheme to take into account correlations beyond the conventional density functional exchange correlations such as LDA and GGA, is that of LDA+U [24]. This prescription however only takes care of the static part of correlation effect. It is an almost perfect scheme for describing the insulators, where only the static correlation effect is important. Since $SrRuO_3$ and $CaRuO_3$ are metals, the dynamical part of correlation effect is important for describing these systems. The LDA+U method fails to describe such system properly. For example, the LDA+U method with $U > 2$ eV predicts a half-metallic ground state with orbital ordering for $SrRuO_3$, which is not observed experimentally. In this situation, within the available tools in the community, the dynamical mean field theory (DMFT) [7] would be the natural choice to deal with the correlation effect in these ruthenates. Further to take care of the material specific aspect of SRO and CRO correctly, we adopted the combined LDA+DMFT approach for the description of these systems.

3.2.6 Model Hamiltonian for LDA+DMFT calculation

In order to interface the DMFT calculation, with LDA, we employed the Nth-order muffin-tin orbital (NMTO) based downfolding method, which reduces the all-band LDA Hamiltonian to a low-energy, few-band Hamiltonian described on effective Wannier-function basis. This is achieved by integrating out the degrees of freedom that are not of interest. For the present study, we kept active Ru-*d* orbitals, including both t_{2g} and e_g, and integrated out all the rest involving O and Sr degrees of freedom. This defines the effective Ru t_{2g} and e_g Wannier functions. The representative functions are shown in the Fig.

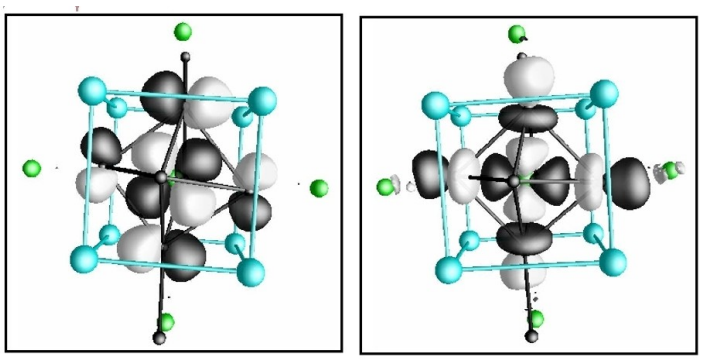

Figure 3.6 Effective Wannier functions corresponding to Ru-d_{xy} (left) and Ru-$dx^2 - y^2$ (right) for $SrRuO_3$. Plotted are the orbital shapes (constant-amplitude surfaces) with lobes of opposite signs colored black and white.

(3.6). In these plots the central parts of the Wannier functions are shaped according to the symmetry of atomic Ru-*d* orbitals, while the tails sitting at the O or A sites are shaped according to O-*p* or Sr/Ca symmetries.

The multiorbital Hubbard model defined on the basis of NMTO-downfolding constructed Ru-*d* Wannier functions is given by H = $H_{LDA} + \frac{1}{2}\sum_{i,m,n,o,p,\sigma,\sigma'} \hat{c}\dagger_{im\sigma}\, \hat{c}\dagger_{in\sigma'}\, \hat{c}_{io\sigma'}\hat{c}_{ip\sigma}U_{mnop}$ with $\hat{c}\dagger_x$ and $\hat{c}_x$ defined as creation and annihilation operators, respectively. The atomic sites (Ru-only sublattice) are denoted by indices *i*; the orbital indices *m,n,* . . . run over five *d* orbitals of Ru, and σ, σ' are spin indices.

Since the strength and extent of interaction is the main issue of our study, we scanned over a range of U values and calculated the mass enhancement factor (m*) for Sr as well as Ca compound. m* is related with real part of self energy via $m^* = 1/Z = (1 - \frac{\partial Re\Sigma}{\partial \omega})$. From our calculation we find that, m* increases as U increases. As is seen in Fig. (3.7), for choice of U value of about 3.5 eV, the value of m* turned out be to in good agreement with the optical conductivity measurements [20]. At U=3.5 eV, m* for SRO turned out to be 2.5 and that of CRO is found to be approximately 1.5 larger than that of SRO. The LDA+DMFT calculations for the Sr compound resulted in a ferromagnetically ordered solution, while CRO did not order. At U=3.5 eV the magnetic moment of $SrRO_3$ turned out to be 0.5 μ_B. Keeping in mind that the present LDA+DMFT calculation implemented in the basis of effective Ru-*d* Wannier function gives only the magnetic moment at the Ru site and that the large Ru-O

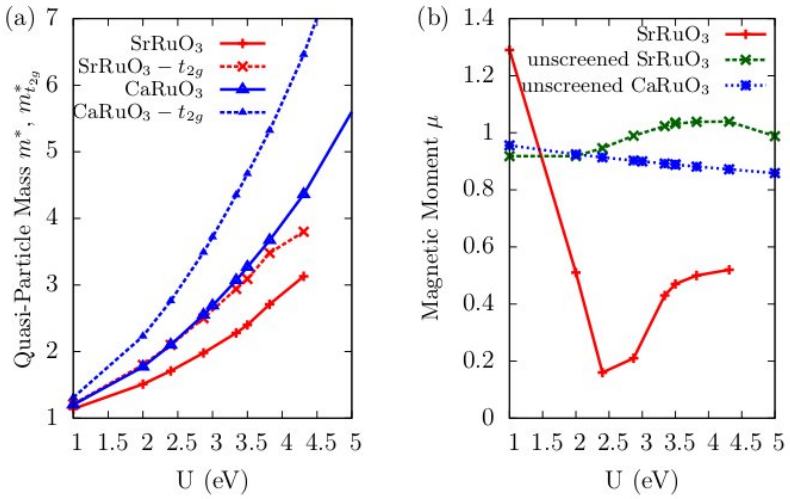

Figure 3.7 (a) Mass enhancement factor obtained within the LDA+DMFT calculations for $SrRuO_3$ and $CaRuO_3$. (a) FM moment of SRO and CRO plotted as a function of strength of electron-electron correlation, U. Panel (b) also shows the unscreened local moments for SRO and CRO.

covalency leads to substantial moments sitting at O sites, the obtained magnetic moment may not be an unreasonable estimate. Considering the LDA estimates of magnetic moment at O sites ($\simeq 0.5\mu_B$ per formula unit) this would amount to a total magnetic moment of about 1.0 μ_B per formula unit.

The plot of LDA+DMFT spectral function in comparison to the effective Ru-*d* LDA downfolded density of states for SRO and CRO, is shown in Fig. (3.8). We chose U=3.5 eV and temperature were set equal to 73 K. We found that the formation of Hubbard-like subbands upon application of the correlation effect in the calculated spectral function. For the sake of comparison we preset the spin-integrated LDA+DMFT spectra for SRO with photoemission data. We found that the calculated spectral function agrees quite well with the experimental data apart from the higher energy side which represents the oxygen contribution, and are missing in our effective Ru-*d* basis. We also calculated the full k-resolved spectral function A(k,ω) for the up and down-spin channels of the ferromagnetically ordered SRO and for CRO. Fig. (3.9) shows the comparison to the LDA band structure with this k-resolved spectral function. We found the formation of Hubbard band like signature, hinting towards correlated metallic picture.

Finally, in Fig. (3.10), we present the temperature evolution of m^* for both SRO and CRO. As

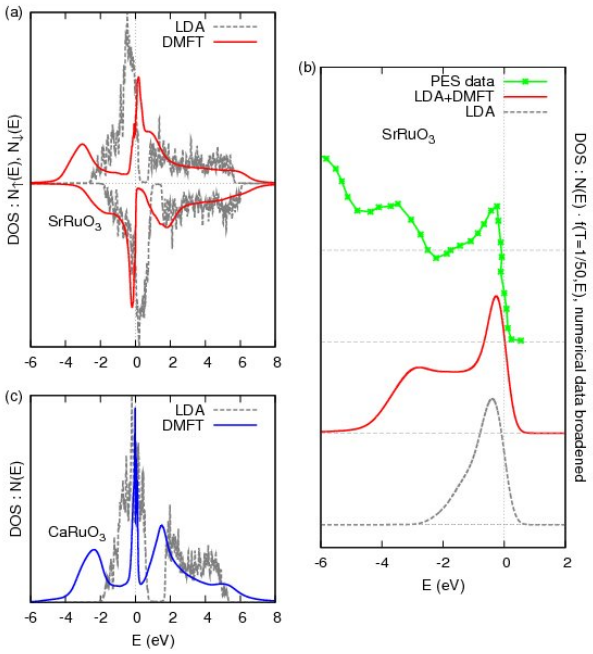

Figure 3.8 LDA+DMFT spectral functions of (a) SRO and (c) CRO in comparison with LDA DOS. Only one of the spin channels is plotted for CRO since there is no net magnetic moment. (b) The spin-integrated LDA+DMFT spectral function and LDA DOS of SRO in comparison with photoemission data from Ref. [18].

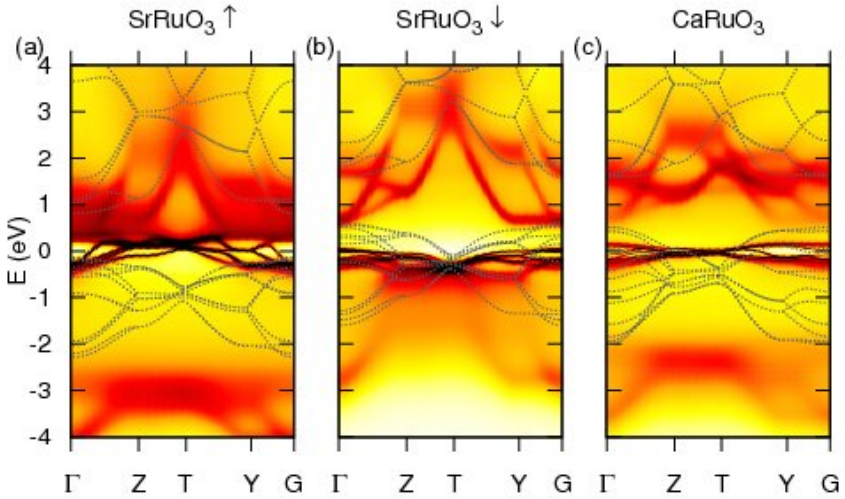

Figure 3.9 Intensity plot of the k-resolved spectral function A(k,ω) calculated within the LDA+DMFT formalism. The LDA band structure, shown with dots, has been superimposed for comparison.

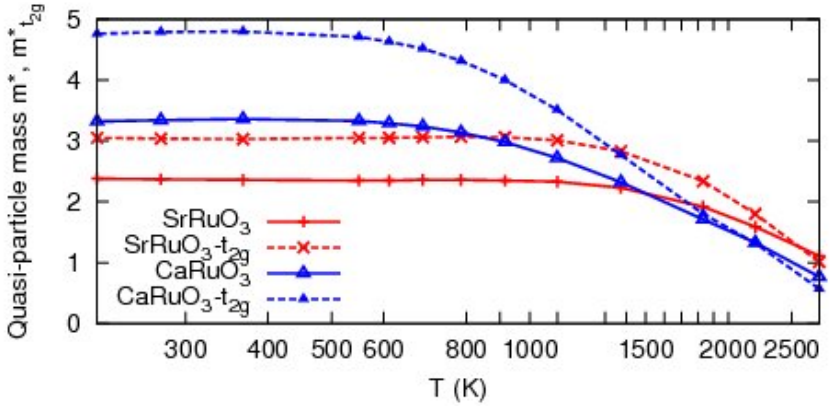

Figure 3.10 The temperature evolution of the mass enhancement factors for SRO and CRO.

temperature is increased, the m*s deviate from their saturation values at some specific temperature, called *coherence temperature* indicating the deviation from the pure Fermi liquid behavior. From the result one would expect a coherence temperature of about 900 K for SRO and about 550 K for CRO. This might explain the observation of non Fermi liquid like behavior in the case of CRO and not in the case of SRO.

3.3 Conclusions

We have studied the different aspects of perovskite ruthenate compounds. We found the evidence of magneto-structural coupling mediated by A cation (e.g Sr) Our obtained results are in agreement with the experimental findings. We also discussed the correlated nature of these 4-*d* ruthenates using combined LDA+DMFT calculations. Our calculations show both SRO and CRO to be correlated metals with reasonably high mass enhancements. The coherence temperature for CRO is found to be substantially lower than that for SRO, providing a possible explanation for the observed non-FL-like behavior in CRO and its absence in SRO. Our calculated k-resolved spectral functions can be compared with future ARPES data.

Bibliography

[1] S. N. Ruddlesden and P. Popper, Acta. Cryst. **10**, 538 (1957); S. N. Ruddlesden and P. Popper, Acta. Cryst. **11**, 54 (1958).

[2] J. J. Randall, and R. Ward, J. Am. Chem. Soc.**81**, 2629 (1959).

[3] J. P. Perdew, K. Burke, and M. Ernzerhof, Phys. Rev. Lett. **77**, 3865 (1996).

[4] O. K. Andersen and O. Jepsen, Phys. Rev. B **12**, 3060 (1975).

[5] O. K. Andersen and T. Saha-Dasgupta, Phys. Rev. B **62**, R16219 (2000).

[6] O. K. Andersen and O. Jepsen, Phys. Rev. Lett. **53**, 2571 (1984).

[7] A. Georges, G. Kotliar, W. Krauth, and M.J. Rozenberg, Rev. Mod. Phys. **68**, 13 (1996).

[8] M. Imada, A. fujimori, and Y. Tokura, Rev. Mod. Phys. **70**, 1039 (1998).

[9] J. J. Randall and R. Ward, J. Am. Chem. Soc. **81**, 2629 (1959).

[10] A. Callaghan, C. W. Moeller and R. Ward, Inorg. Chem. **5**, 1572 (1966); J. M. Longo, P. M. Raccah and J. B. Goodenough, J. Appl. Phys. **39**, 1327 (1966); A. Kanbayasi, J. Phys. Soc. Jpn. **44**, 108 (1978).

[11] M. Takizawa, D. Toyota, H. Wadati, A. Chikamatsu, H. Kumigashira, A. Fujimori, M. Oshima, Z. Fang, M. Lippmaa, M. Kawasaki, and H. Koinuma, Phys. Rev. B **72**, 060404(R) (2005); K. Maiti and R. S. Singh, Phys. Rev. B **71**, 161102(R) (2005).

[12] K. Maiti, Phys. Rev. B **73**, 235110 (2006), *ibid.* **77**, 212407 (2008).

[13] G. Cao, S. McCall, M. Shepard, J. E. Crow, and R. P. Guertin, Phys. Rev. B **56**, 321 (1997).

[14] P. Khalifah, I. Ohkubo, H. M. Christen, and D. G. Mandrus, Phys. Rev. B **70**, 134426 (2004).

[15] L. Klein, L. Antognazza, T. H. Geballe, M. R. Beasley, and A. Kapitulnik, Phys. Rev. B **60** 1448 (1999).

[16] K. Maiti, R. S. Singh and V. R. R. Medicherla, Europhys. Lett. **78**, 17002 (2007).

[17] G. Cao, O. Korneta, S. Chikara, L. E. DeLong, and P. Schlottmann, Solid State Commun. **148**, 305 (2008).

[18] D. Toyota *et. al.*, Appl. Phys. Lett. **87**, 162508 (2005).

[19] R. S. Singh, V. R. R. Medicherla and Kalobaran Maiti, Appl. Phys. Lett. **91**, 132503 (2007); J. Park, S. J. Oh, J. H. Park, D. M. Kim and C. B. Eom, Phys. Rev. B **69**, 085108 (2004).

[20] J. S. Ahn, J. Bak, H. S. Choi, T. W. Noh, J. E. Han, Y. Bang, J. H. Cho, and Q. X. Jia, Phys. Rev. Lett. **82**, 5321 (1999).

[21] P. B. Allen, H. Berger, O. Chauvet, L. Forro, T. Jarlborg, A. Junod, B. Revaz and G. Santi, Phys. Rev. B **53**, 4393 (1996).

[22] G. Kresse and J. Hafner, Phys. Rev. B **47**, R558 (1993); G. Kresse and J. Furthmuller, *ibid.* **54**, 11169 (1996).

[23] J. B. Goodenough, Prog. Solid State Chem. **5**, 145 (1971).

[24] V. I. Anisimov, I. V. Solovyev, M. A. Korotin, M. T. Czyzyk and G. A. Sawatzky, Phys. Rev. B **48**, 16929 (1993).

[25] D. J. Singh, J. Appl. Phys. **79**, 4818 (1996).

[26] Debdutta Lahiri, T. Shibata, S. Chattopadhyay, Sudipta Kanungo, T. Saha-Dasgupta, R. S. Singh, Surinder M. Sharma, and Kalobaran Maiti ; Phys. Rev B **82**, 094440 (2010).

Chapter 4

Pressure driven changes in electronic structure of $BiCoO_3$ *

4.1 Back ground and Motivation of the present study

Multiferroic compounds with co-existing magnetic and ferroelectric order[1] are in focus of current attention due to the potential technological applications [2]. Perovskite type materials of general formula ABO_3 and related materials have been discussed extensively for this purpose. Apart from improper multiferroics [3] most of known magnetic ferroelectrics have lone pair active Pb or Bi ion at A site and a transition metal ion having unpaired *d* electron at B site. The ferroelectricity is primarily driven by A site cation, magnetism being driven by B site cation. Following this idea, compounds like $BiFeO_3$ [4], $PbVO_3$ [5] have been synthesized which show large polarization as well as large transition temperature together with antiferromagnetic ordering of spins at B site. Along the same line of thought, high pressure synthesis [6] of $BiCoO_3$ has been carried out. The presence of Co ion in $BiCoO_3$ which is well known for its spin-state transition, is expected to add another aspect to the multiferroic aspect of the compound.

In ambient pressure (AP), $BiCoO_3$ is in polar tetragonal structure with a high tetragonal ratio of c/a=1.27. In this AP phase, $BiCoO_3$ is in high spin (HS) state of Co^{3+} with a large calculated [7] polarization (170 $\mu C/cm^2$). This HS of Co is found to be retained down to the lowest temperature, pre-

*This chapter is based on *Phys. Rev. B 83, 104104 (2011)*

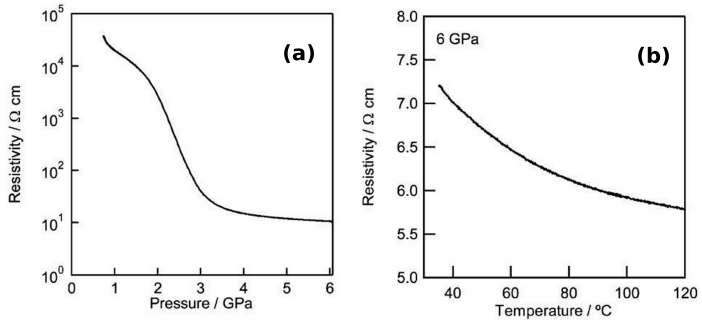

Figure 4.1 (a) Pressure dependence of the resistivity at 300 K and (b)temperature dependence of the resistivity at 6 GPa of $BiCoO_3$. Figures are reproduced from Ref. [10]

venting the temperature driven route of spin state transition, unlike in case of $LaCoO_3$ [8]. Therefore attempts have been made drive the spin state transition of Co in $BiCoO_3$ through the pressure driven route. Theoretical predictions have been made by Ravindran *et. al.* [7] as well as by Ming *et. al.* [9] based on density functional theory (DFT) calculations. Both the calculations report a high spin (HS) to low spin (LS) transition with associated volume collapse at a critical pressure. However, these two studies, arrived at two different crystallographic symmetries of $BiCoO_3$ at high pressure (HP) phase. The study by Ravindran *et. al.* predicted HP phase to be cubic paraelectric phase which is metallic. Ming *et. al.*, on the other hand, found no evidence of tetragonal to cubic phase transition, though isostructural HS to LS transition was found to occur with reduction in c/a ratio in HP phase, the LS phase being of semi-metallic nature. However, after these theoretical reports, the high pressure phase has been synthesized and pressure dependent resistivity measurement [10] has been carried out. Experimentally, the theoretically predicted semi metal or metallic behavior for the high pressure phase has not been observed, instead a resistivity jump of three order of magnitude has been observed upon varying pressure as shown in Fig. (4.1). The crystal structure of the HP phase is also characterized as orthorhombic phase, in contradiction to the theoretical predictions.

In the present study, we therefore re-investigate the issue related to the changes in the electronic structure of $BiCoO_3$ under pressure based on the experimentally determined crystal structure. Our calculations have been carried out within the framework of generalized gradient approximation (GGA) of DFT. We have carried out calculations in two different choices of basis sets, in muffin tin orbital

(MTO) based basis as well as in the plane wave basis in order to check the robustness of our obtained results.

4.2 Results and Discussions

4.2.1 Crystal Structure at ambient pressure and high pressure

The crystal structures of $BiCoO_3$ at ambient pressure as well as high pressure have been determined [10] using synchrotron X-ray and neutron powder diffraction measurements. Based on that a structural transition from the ambient pressure tetragonal phase to the orthorhombic phase characterized with $GdFeO_3$ kind of distortion has been predicted between 2-3 GPa pressure, accompanied by 13 % volume compression. The local co-ordination of oxygen atoms around Co^{3+} ion in the ambient pressure phase is observed to be polar pyramidal co-ordination with a short apical oxygen (O1)-Co bond and four equal basal oxygen (O2)-Co bonds, as shown in upper, left panel of Fig. (4.2). The reduction of local co-ordination from normally expected octahedral to pyramidal symmetry has been argued [11] to be caused by the high spin state of Co. The HS state of Co in Co^{3+} valence would lead to orbital degeneracy in perfect octahedral symmetry which is prevented by adopting to polar pyramidal co-ordination. This adds onto the distortion caused by the lone-pair active Bi ion. Upon application of pressure, beyond a critical pressure, change of crystal symmetry from tetragonal to orthorhombic occurs. In the high pressure phase, the local co-ordination of oxygen atoms around Co is restored [cf. upper, right panel of Fig. (4.2)] to octahedral symmetry. The CoO_6 octahedra is slightly distorted with the longest oxygen-Co bond length deviating by about 0.2% from the average value. This leads to a large volume contraction in the HP phase compared to the AP phase, primarily due to the shortening of the long oxygen-Co bond length lying outside the pyramidal co-ordination in the AP phase. The CoO_6 octahedra in the HP orthorhombic phase rotates and tilts, leading to $GdFeO_3$ kind of distortion with in plane Co-O-Co angle of 153.9^o and out of plane Co-O-Co angle of 154.8^o. The local oxygen environment around Bi is distorted both in AP and in HP phase, as shown in lower panels of Fig. (4.2). In the AP phase, four out of eight O2 oxygens are pulled out giving rise to polar distortion around Bi ion. In the HP phase, each Bi ion has four out of twelve near oxygens, involving both O1 and O2 pulled closer in. This causes each O1 and O2 atoms pulled closer to one and two of its four nearest Bi

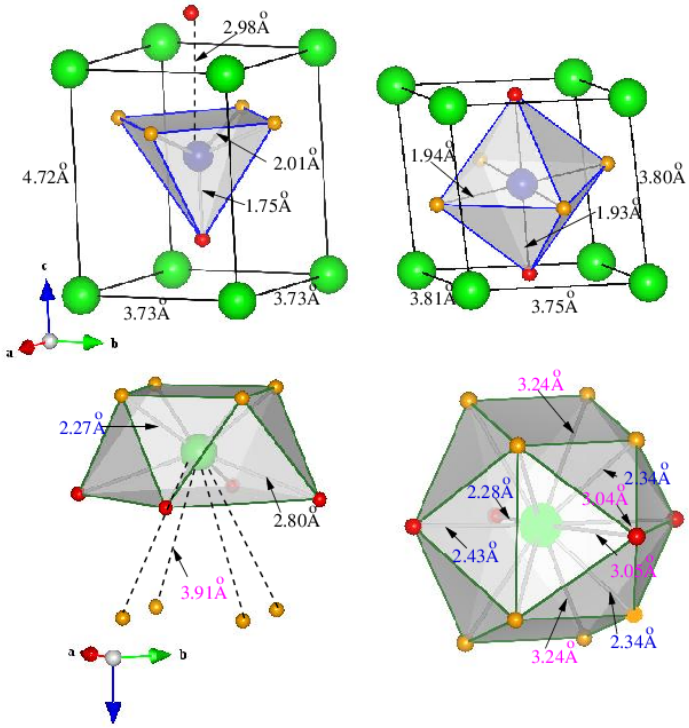

Figure 4.2 Crystal structure of $BiCoO_3$ in AP phase (left panels) and in HP phase (right panels). The large sized (green color) and medium sized (blue color) balls represent Bi and Co atoms respectively. The red and yellow colored small balls represent the O1 and O2 oxygens respectively. The local oxygen environment around Co atom is indicated with shaded polyhedra. The bottom panels show the local oxygen environment around the isolated Bi atoms.

neighbors, respectively, giving rise to $GdFeO_3$-type distortion.

4.2.2 Electronic Structure of $BiCo_3$ in AP and HP phase

Fig. (4.3) shows the non spin-polarized density of states (DOS) of $BiCoO_3$ for the AP and HP phases. Reported density of states are calculated using the muffin-tin orbital (MTO) based linear muffin tin orbital (LMTO) [12] as implemented in Stuttgart code [13]. Results have been cross checked via the plane wave based pseudopotential calculations as implemented in the Vienna ab initio Simulation Package (VASP) [14]. We used GGA approximation for the exchange correlation functional. Details of the methods are discussed in chapter 2. The Co-*d* O-*p* hybridized electronic states extend from an energy range of about -8 eV below Fermi energy (E_f) to about 1 eV above E_f for AP phase and to

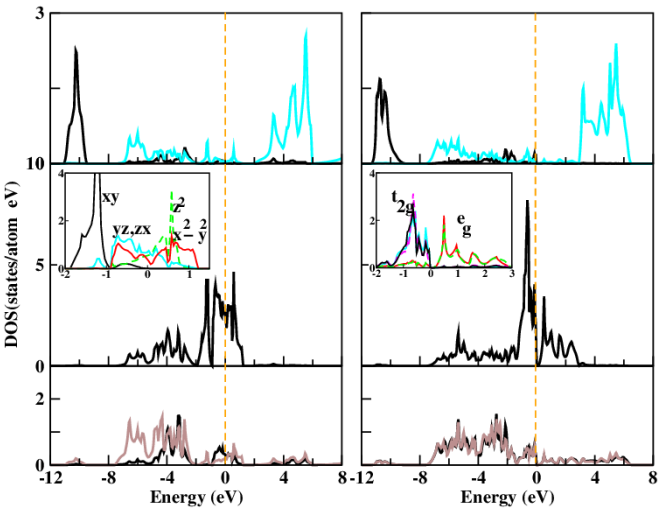

Figure 4.3 Non spin-polarized density of states computed for $BiCoO_3$ at AP (left panels) and at HP (right panels). DOS are projected on to Bi (top panels), Co-*d* (middle panels) and O-*p* (bottom panels) states. The black and cyan colored lines in the top panels represent projections on to Bi *s* and Bi *p* states respectively. The black and brown colored lines in the bottom panels represent projections on to O1 and O2 states respectively. The insets in the middle panels represent partial DOS projected on to different *d* characters of Co. The zero of the energy, marked by a dashed vertical line, is set at E_F.

about 3 eV above E_f for the HP phase. The states in the energy interval -8 eV to -2 eV are dominated by O-*p* character, while the states close to E_f are dominated by Co-*d* character. The occupied Bi-6*s* states lye far below E_f, beyond the energy -9 eV and the empty Bi-6*p* states lye far above E_f from 2 eV to 6 eV. The insets in the middle panels in Fig. (4.3) show the Co-*d* partial DOS projected onto different *d* characters. For the AP phase, the lowest Co-*d* state is of d_{xy} character, followed by the degenerate Co-d_{yz} and d_{xz} states, followed by Co-$d_{3z^2-r^2}$ and the topmost state is of Co-$d_{x^2-y^2}$ character. The non spin polarized electronic structure gives rise to a metallic solution with states of $d_{xz,yz}$, $d_{3z^2-r^2}$ and $d_{x^2-y^2}$ character crossing the Fermi level. For the HP phase, due to the change in symmetry of the ligand field, the splitting pattern changes to broadly divided t_{2g} states and e_g states. The presence of small distortion in CoO_6 octahedra in terms of slightly different Co-O bond lengths lifts the strict degeneracy of three (two) t_{2g} (e_g) states, as in evident from the plot. The deviation of Co-O-Co bond angles from 180^o due to the presence of $GdFeO_3$ kind distortion narrows down the respective Co-t_{2g} and Co-e_g band widths opening up a small gap of about 0.06 eV.

Fig. (4.4) shows the spin polarized DOS computed for the AP phase, for the ferromagnetic (FM)

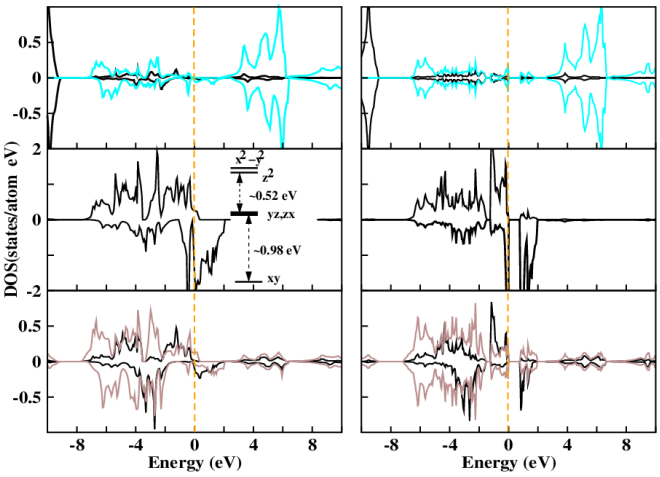

Figure 4.4 Spin-polarized density of states of $BiCoO_3$ at AP, computed considering the ferromagnetic spin alignment of Co (left panels) and C-type antiferromagnetic spin alignment of Co (right panels). DOS are projected on to Bi (top panels), Co-*d* (middle panels) and O-*p* (bottom panels) states. The black and cyan colored lines in the top panels represent projections on to Bi-*s* and Bi-*p* states respectively. The black and brown colored lines in the bottom panels represent projections on to O1 and O2 states respectively. The inset in the left, middle panel represent the energy level splitting of different *d* levels of Co.

alignment of Co spins (left panel) and experimentally observed [6] C-type antiferromagnetic (C-AFM) alignment of Co spins (right panel). The C-type antiferromagnetic alignment involves antiparallel alignment of Co spins within the *ab* plane which are coupled ferromagnetically along the *c*-axis as shown in Fig. (4.5). The spin polarized calculation leads to a finite spin splitting within the Co-*d* states. The magnetic moments listed in the Table. 4.1 show a rather large moment at O1 oxygen site, due to large Co-O covalency driven by short Co-O1 bond length. The total moment per formula unit for the FM state is found to be 3.7 μ_B (in LMTO calculation) 3.5 μ_B (in plane wave calculation) indicating the high spin state of Co. The inset of Fig. (4.4) in left panel shows the energy level splittings of Co-*d* levels taking into account the O covalency in the polar pyramidal environment. The results are obtained from the NMTO downfolding calculations [16] keeping only the Co-*d* states active and downfolding all the other states, including O-*p* states, and considering the on site block of the real space Hamiltonian in the downfolded Co-*d* basis. While the d_{xy} level lies well below the degenerate d_{xz} and d_{yz}, separated by about 1 eV, $d_{xz,yz}$, $d_{3z^2-r^2}$ and $d_{x^2-y^2}$ are closely spaced. $d_{3z^2-r^2}$ and $d_{x^2-y^2}$ levels are separated by an energy difference of less than 0.1 eV, the energy difference between $d_{xz,yz}$ and $d_{3z^2-r^2}$ being about 0.5

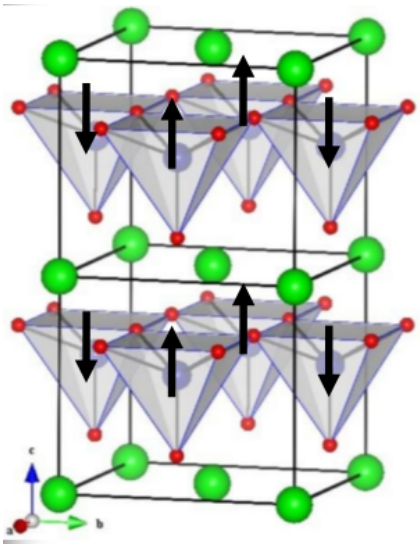

Figure 4.5 Spin arrangements of C type antiferromagnetic configuration of Co site. Color conventions are same as Fig. 4.2

eV. All these energy difference are less than half of the band width of $d_{xz,yz}$, $d_{3z^2-r^2}$ and $d_{x^2-y^2}$ which are around 2 eV, as is seen from the inset in left panel of Fig. (4.3). This causes a pseudo gap between d_{xy} dominated states and other d states which are overlapping with each other. The FM alignment of Co spins, therefore gives rise to a metallic solution with a hole pocket in the up spin channel and an electron pocket in the down spin channel. The C-type antiferromagnetic spin arrangement of Co spin reduces the band widths significantly due to the increase of the lattice constant in the magnetic lattice, which opens a gap of about 0.7-0.6 eV. The plane wave calculation gave rise to a gap of 0.6 eV, while LMTO calculation gave rise to a gap of 0.73 eV. The antiferromagnetic phase is found to be energetically favorable over the FM spin configuration by a rather large energy difference of 0.335 eV per formula unit in LMTO calculation and 0.313 eV per formula unit in plane wave calculation. The results are in agreement with previously reported [17] electronic structure calculation for $BiCoO_3$ in AP phase, carried out in linear augmented plane wave (LAPW) basis.

The spin polarized calculation carried out for HP phase, converged to non magnetic solution with zero magnetic moment at each site as shown in Fig. (4.6). This leads us to conclude that the Co is in low spin state in HP phase, as opposed to the suggestion from X-ray emission spectra of the intermediate spin state [10]. The low spin state is driven by the rather large crystal field splitting of about 2 eV.

Table 4.1 Magnetic Moments at Co, O1 and O2 sites for $BiCoO_3$ at AP, as obtained in spin-polarized GGA calculations in LMTO basis for FM and C-AFM spin arrangements. The entries within the bracket denote the numbers obtained in plane wave basis.

	Magnetic moment in μ_B	
	FM	C-AFM
Co	2.66 (2.66)	2.54 (2.54)
O1	0.52 (0.44)	0.45 (0.40)
O2	0.18 (0.18)	0.00 (0.00)

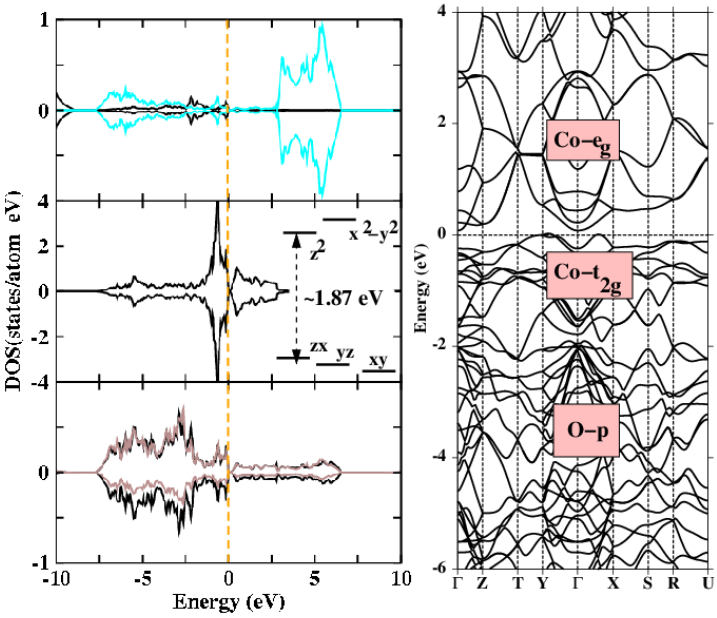

Figure 4.6 Spin-polarized density of states, projected on to Bi (top, left panel), Co-*d* (middle, left panel) and O-*p* (bottom, left panel), and band structure of $BiCoO_3$ at HP (right panel). The color convention for the DOS plot is same as in Figs. (4.3) and (4.4). The inset in the left, middle panel represent the energy level splitting of different *d* levels of Co. The band structure plot shows opening of an indirect gap of about 0.06 eV between Γ point and the Y point.

Table 4.2 Total energies (in eV) per formula unit calculated for the discussed HP phases in literature, orthorhombic phase as predicted in the experimental study of Ref.[10], the cubic phase predicted in theoretical study in Ref.[7] and the tetragonal phase predicted in the theoretical study in Ref.[9].

Considered phase	Total energy
Cubic	-30.246
Tetragonal	-30.779
Orthorombic	-31.066

We have checked our conclusion by repeating the calculation within the framework of GGA+U with a choice of U=4 eV and J=1 eV applied at Co site. The result was found to remain unchanged with convergence to non magnetic solution. In absence of magnetism, the insulating state is therefore driven by the $GdFeO_3$ kind of structural distortion, leading to a tiny gap of about 0.06 eV. The existence of the gap is checked by calculations in two basis sets, LMTO and plane wave. Both lead to a tiny gap at E_F, with a precise value of 0.055 eV for calculation in LMTO basis and 0.060 eV for calculation in plane wave basis [18]. This explains the semiconducting behavior of the HP phase observed experimentally as opposed to theoretically predicted metallic or semi-metallic behavior. We note at this stage, the obtained energy gap in HP phase is an order of magnitude smaller compared to that obtained for the AP phase in presence of C-AFM spin ordering. This presumably explains the three order of magnitude jump in the resistivity observed in experiment [10].

Turning back to electronic structure at HP phase, as is seen from the inset of Fig. (4.6), the crystal field splitting separating the t_{2g} and e_g blocks turns out to be 1.92 eV considering the average energy position of t_{2g} states and that of e_g states. The band widths of t_{2g} and e_g states turn to about 1.5 eV and 2.5 eV respectively, giving rise to a situation where t_{2g} and e_g derived bands just fall short of overlapping with each other. The presence of $GdFeO_3$ kind of distortion responsible for the narrowing down of the bands is therefore, essential for the explanation of the non metallic behavior observed experimentally. We have checked the stability of the orthorhombic phase, characterized with $GdFeO_3$-type distortion, over the previous theoretically predicted tetragonal or cubic HP phases through total energy calculations. The results of total energy calculations are summarized in Table. 4.2. It shows that

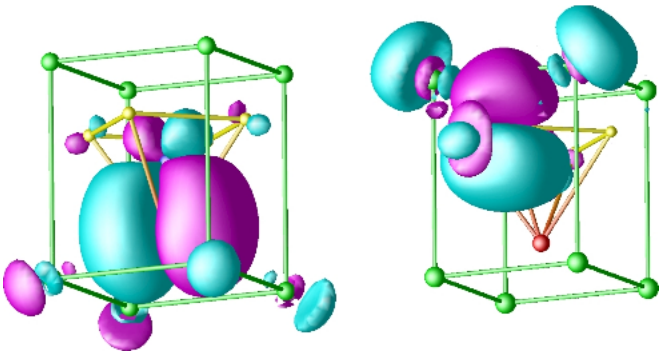

Figure 4.7 Plot of the effective O-*2p* Wannier functions for $BiCoO_3$ at AP, placed within the unit cell formed by Bi atoms at the corners and CoO_5 pyramid at the center. The left panel and right panels show one of the O1 and O2 *p* Wannier functions, respectively. Constant amplitude surfaces are shown with lobes of opposite signs colored with cyan and magenta. The central parts of the Wannier functions are shaped according to O1 p_y (left panel)and O2 p_z (right panel) while the tails extending to Co and Bi are shaped according to Co-*d* and Bi degrees of freedom. The pdσ bonds with Co and the covalency with Bi lone pair are visible.

the orthorhombic symmetry is favoured over the tetragonal symmetry by 0.287 eV per formula unit and over cubic symmetry by a very large value of 0.820 eV per formula unit.

4.2.3 Bi-O covalency and distortion

Covalency between occupied O-*p* and cation A states is believed to be responsible for the $GdFeO_3$ kind of distortion, speculated by Goodenough about 40 years back [19] and demonstrated in an elaborate fashion in recent work [20] in the context of d^1 perovskites. This section, we investigate this aspect in terms of construction of effective Wannier functions for the occupied O-2*p* bands and the analysis of crystal orbital Hamiltonian populations.

The valence electron configuration of Bi is $6s^2\ 6p^3$. Therefore, the formally trivalent Bi in $BiCoO_3$ contains a lone pair of 6*s* electrons. $6s^2$ lone pair plays an important role in the activity of Bi ion. The stereochemical activity of the Bi lone pairs has been found to have a major contribution from Bi 6*s*-O2*p* mixing [21]. The off centric, polar movement in the AP phase is believed to be caused by this effect. This causes Bi to be pulled closer to eight of the surrounding twelve oxygen atoms, causing four of the oxygen atoms residing out of the neighbor shell of Bi, as discussed already and shown in Fig. (4.2). This off-centric movement of Bi with respect to its oxygen cage, together with that of Co, gives rise

to the non centrosymmetric, polar structure in the AP phase. The Bi-O covalent interactions can be visualized in terms of effective Wannier functions constructed for the occupied O 2*p* bands, as shown in Ref. [20]. Fig. (4.7) show the plots of such Wannier functions, the one in the left being that for O1 and the one in the right for O2. These functions are constructed using NMTO-downfolding technique by keeping active O-2*p* degrees of freedom and downfolding the rest. The obtained downfolded bands, therefore, pick up only the O-2*p* bands out of the full DFT band structure. The underlying NMTO basis corresponding to the downfolded, occupied O-2*p* bands, defines the effective Wannier functions. The central part of these Wannier functions has either oxygen p_x or p_y or p_z symmetry while their tails extending to Co and Bi sites are shaped according to integrated out Co and Bi degrees of freedom. We find signature of Co-O bonding characters in terms of presence of finite weights at Co sites, shaped like Co-*d*. Significant amount of weights are also found at the Bi sites. The weight at Bi site is primarily of Bi-*6s* character, which is antibonding to the central O-*p* function. The finite mixing between Bi-6*s* and O 2*p* gives rise to the lobe like structure of Bi-6*s* tails, which has been pointed out by Watson and Parker [21] to be responsible for its stereochemical activity. The Bi-*6s* - O-*2p* mixed state further hybridizes with empty Bi-*6p* state lowering the energy of the system, as is seen in terms of presence of Bi-*6p* like shapes in the tails sitting at Bi sites. Lone pairs in Bi or Pb containing oxides have been visualized with the aid of electron localization function in literature [22]. Plot of effective Wannier functions for occupied oxygen *p* bands provides an alternative approach for such visualization due the finite mixing between lone pair and the anion *p* degrees of freedom.

In Fig. (4.8), we show again the plots of effective O Wannier functions, but now plotted for the HP phase. Apart from the presence of Co-O bonds, the finite mixing between Bi-*s* (and Bi-*p*) and O *p* continues to be present, though its precise nature changes. For the O1 Wannier functions at AP phase, four tails are observed at four bottom corner Bi atoms which are equally strong while for HP phase, the tails are found to be of varying strength with one of the tails being much stronger than the others. The strongest tail in HP phase has more weight compared to the AP case. For the O2 Wannier function, two tails of equal strength at the nearest Bi sites are observed for AP phase, while for the HP phase, three tails are observed of varying strength. The precise shape of the tails also changes between the AP and HP phases.

In order to further understand the covalency properties and their changes between the AP and HP

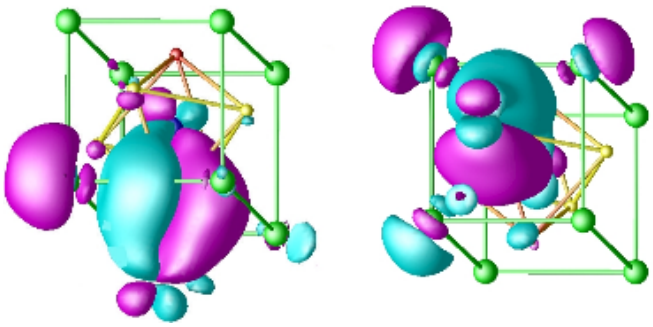

Figure 4.8 Same as in Fig. 4.7, but for $BiCoO_3$ at HP. The Wannier functions are placed within the unit cell formed by the Bi atoms at the corners and CoO_6 octahedra at the center.

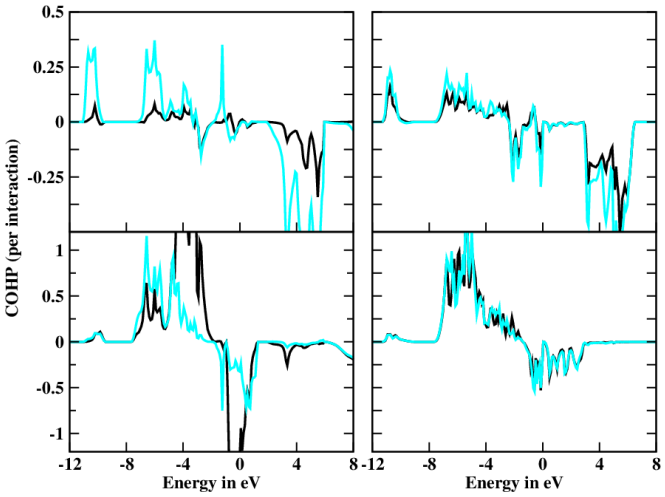

Figure 4.9 Crystal orbital Hamiltonian populations (COHPs) between Bi and O (top panels), that between Co and O (bottom panels) in AP (left panels) and HP (right panels) phases of $BiCoO_3$. The black and cyan colored lines represent COHP defined for O1 and O2 respectively. The Bi-O COHP's are scaled to 4 nearest Bi-O1 interactions and Bi-O2 interactions, and Co-O COHPs are scaled to one (two) nearest Co-O1 interactions for AP (HP) phases, and four nearest Co-O2 interactions. Zero of the energy is set at E_F.

phases, we computed the Bi-O and Co-O crystal orbital Hamiltonian populations [23] (COHPs). COHP is the density of states weighted by the corresponding Hamiltonian matrix element. COHPs indicate the strength as well as the nature of interaction, the bonding (antibonding) interaction being indicated by positive (negative) values of COHP. Fig. (4.9) shows the Bi-O and Co-O COHPs plotted for the AP and HP phases of $BiCoO_3$. The COHPs have been resolved into contributions from O1 and O2 oxygens. The contributions from O1 and O2 differ significantly for the AP phase while they are similar for the HP phase, as expected from the distinctly different and similar environment of O1 and O2 for the AP and HP phase crystal structures of $BiCoO_3$, respectively.

The contribution of O2 in Co-O COHP is rather similar in between AP and HP phases, while the strength of Co-O1 COHP is much larger in AP phase compared to HP phase due to the presence of short Co-O1 bond length. Focusing on Bi-O COHPs and comparing between AP and HP phases, we find that the strength of COHPs to be larger for AP phase considering the O2 contribution while they are somewhat more dispersed for the HP phase. The nature of the antibonding states close to E_F also changes between AP phase and HP phase, indicating the change in the localization of the Bi-$6s^2$ lone pair state between the AP phase and HP phase, hinting in turn, to the change in the details of covalency between Bi and O. One of them drives the polar distortion and the other drives the $GdFeO_3$ kind of distortion.

4.3 Conclusion

To summarize, we have investigated the electronic structure of $BiCoO_3$ at the ambient pressure and high pressure phases, based on recently measured crystal structure data [10]. While the obtained results for the ambient pressure are in agreement with previous reports,[17] the electronic structure at high pressure phase shows presence of a finite energy gap at Fermi energy in contrast with previously reported metallic or semi-metallic character at high pressure. This semiconducting behavior in the non magnetic $BiCoO_3$ with low spin state of Co, is found to be driven by the presence of $GdFeO_3$ kind of distortion which arises due to finite mixing of Bi lone pair state with O-p states. The electronic structure of the ambient pressure phase shows an energy gap arising due to the antiferromagnetic alignment of Co in high spin state, which is an order of magnitude larger than the energy gap at the high pressure

phase. This explains the three order of magnitude jump in resistivity observed experimentally obtained by varying pressure [10].

Bibliography

[1] N. Hill, J. Phys. Chem. B **104**, 6694 (2000).

[2] J. F. Scott, Nat. Mat. **6** 256 (2007).

[3] S. Picozzi, K. Yamauchi, I. Sergienho, B. Sanyal and E. Dagatoo, J. Phys. Condens. Matt. **20**, 434208 (2008).

[4] J. B. Neaton, C. Ederer, U. V. Waghmare, N. A. Spaldin and K. M. Rabe, Phys. Rev. B **71**, 014113 (2005).

[5] A. A. Belik, M. Azuma, T. Saito, Y. Shimakawa and M. Takano, Chem. Mater. **17**, 269 (2005).

[6] A. A. Belik, S. Iikubo, K. Kodama, N. Igawa, S. Shamoto, S. Niitaka, M. Azuma, Y. Shimakawa, M. Takano, F. Izumi, and E. Takayama-Muromachi, Chem. Mater. **18**, 798 (2006).

[7] P. Ravindran, R. Vidya, O. Eriksson and H. Fjellvag, Adv. Mater. **20**, 1353 (2008).

[8] Y. Tokura, Y. Okimoto, S. Yamaguchi, H. Taniguchi, T. Kimura and H. Takagi, Phys. Rev. B **58**, 1699 (1998).

[9] X. Ming, X. Meng, F. Hu, C. Wang, Z. Huang, H. Fan and G. Chen, J. Phys.: Condens. Matter **21**, 295902 (2009).

[10] K. Oka, M. Azuma, W. Chen, H. Yusa, A. A. Belik, E. Takayama-Muromachi, M. Mizumaki, N. Ishimatsu, N. Hiraoka, M. Tsujimoto, M. G. Tucker, J. Attfield and Y. Shimakawa, J. Am. Chem. Soc. **132**, 9438 (2010).

[11] K. Oka, I. Yamada, M. Azuma, S. Takeshita, K. H. Satoh, A. Koda, R. Kadono, M. Takano, and Y. Shimakawa, Inorg. Chem. 47, 7355 (2008).

[12] O. K. Andersen, Phys. Rev. B **12**, 3060 (1975).

[13] Stuttgart TBLMTO-47 code; O. K. Andersen and O. Jepsen, Phys. Rev. Lett. **53**, 2571 (1984).

[14] G. Kresse and J. Hafner, Phys. Rev. B **47**, R558 (1993); G. Kresse and J. Furthmuller, Phys. Rev. B **54**, 11169 (1996).

[15] J. P. Perdew, K. Burke, and M. Ernzerhof, Phys. Rev. Lett. **77**, 3865 (1996).

[16] O. K. Andersen and T. Saha-Dasgupta, Phys. Rev. B **62**, R16219 (2000).

[17] M. Q. Cai, J. C. Liu, G. W. Yang, Y. L. Cao, X. Tan, X. Y. Chen, Y. G. Wang, L. L. Wang, and W. Y. Hu, J. Chem. Phys. **126**, 154708 (2007).

[18] We note that this gap is driven by structural distortion rather than the correlation effect. Since the discussed material is a transition metal oxide, correlation effect necessarily arises, and will act on top on the structural effect in enhancing the gap size. Since choice of U is not unique, gap of different sizes can be predicted considering different choice of U values. We therefore refrained from quoting the gap values calculated with GGA+U and presented the GGA calculated gap consistently for AP and HP phases.

[19] J. B. Goodenough, Prog. Solid State Chem. **5**, 145 (1971).

[20] E. Pavarini, A. Yamasaki, J. Nuss, and O. K. Andersen, New J. Phys, **7**, 188 (2005).

[21] G. W. Watson and S. C. Parker, J. Phys. Chem. B **103**, 1258 (1999).

[22] R. Seshadri and N. A. Hill, Chem. Mater. **13**, 2892 (2001); R. Seshadri, G. Baldinozzi, C. Felsera and W. Tremel, J. Mater. Chem. **9**, 2463 (1999).

[23] R. Dronskowski, P. E. Blöchl, J. Phys. Chem. **97**, 8617 (1993).

Chapter 5

Ab-initio study of low dimensional quantum spin systems Sr_3NiPtO_6, Sr_3CuPtO_6 and Sr_3NiIrO_6 *

5.1 Background and motivation of the present work

Transition metal oxide (TMO) based low dimensional quantum spin systems (QSS) form an active field of research in condensed matter physics. Though this class of systems have 3-D crystal structure but the effective electronic or magnetic dimensionality of the systems is reduced to lower dimensions such as 1-D or 2-D. The details of the low dimensional aspects and importance of the anisotropic interactions have already been discussed in the section. III of chapter 1. A pertinent question in this connection has been, given a compound what is the underlying spin model. Often the extracted spin model by considering the crystal structure only or by fitting experimental data such as magnetic susceptibility, may give rise to non-unique answers. Therefore microscopic understanding is needed for the sake of uniqueness.

In this present study, we choose compounds of general formula $A_3BB'O_6$ where A is an alkaline earth Sr/Ca, and B and B$'$ are transition metal elements. It might be possible that both B and B$'$ are magnetic ions or one is magnetic and another is non-magnetic. There exist huge literature on different

*This chapter is based on *Phys. Rev. B* **82**, *235122 (2010)*

compounds in this family. Various elements in the periodic table can be chosen as a possible candidates for B and B′ ions, starting from 3-*d* to 5-*d* transition metal ions, both of magnetic and non-magnetic type. One of the most well studied compound in this family is $Ca_3Co_2O_6$,[2] where B and B′ both are occupied by Co ions, but one Co is in low spin state and another in high spin state. Recent studies on this system show very unusual and complicated magnetic phases [3, 4, 5]. Among the other Co based compounds in this series, the compound Ca_3CoRhO_6 [4, 6, 7] and Ca_3CoMnO_6 [8, 9] have been studied in the context of multiferroic behavior and spin-orbit coupling. A review of the synthesized compounds may be found in Ref. [11], showing variety of interesting properties [10].

In the present study, we focus on three such compounds, namely Sr_3NiPtO_6, Sr_3CuPtO_6 and Sr_3NiIrO_6. One can notice that in the first two compounds, the B′ sites are occupied by the same 5-*d* element, Pt, whereas the B sites are occupied by two neighboring 3-*d* elements in the periodic table, Ni and Cu in the two cases. For the first and third compounds, the B sites are occupied by same 3-*d* element, namely Ni while the B′ sites are occupied by two neighboring 5-*d* elements in the periodic table, Pt and Ir in the two cases. Therefore it provides a nice possibility to have a comparative study between different compounds within this interesting family whose components differ in their electronic configurations in terms of addition or subtraction of one electron only. Experimentally, it was observed that Sr_3NiPtO_6 shows no evidence of long- range magnetic ordering down to 1.8 K temperature [12, 13] along with large single-ion anisotropy, while Sr_3CuPtO_6 was reported to exhibit S=$\frac{1}{2}$ Heisenberg chain-like behavior with substantially large inter-chain coupling [12] and possible existence of a gap in the spin excitation spectra [14]. Sr_3NiIrO_6, on the other hand, was reported to show disordered antiferromagnetic ground state [15] with signatures of significant ferromagnetic interactions [16].

We have carried out density functional theory (DFT) analysis in terms of construction of effective Wannier functions and the low energy model Hamiltonians, and the calculation of magnetic exchange interactions. We have also carried out calculations in presence of spin-orbit coupling (SOC) to know its importance in three compounds which also provide us with the information of magnetic anisotropic energy.

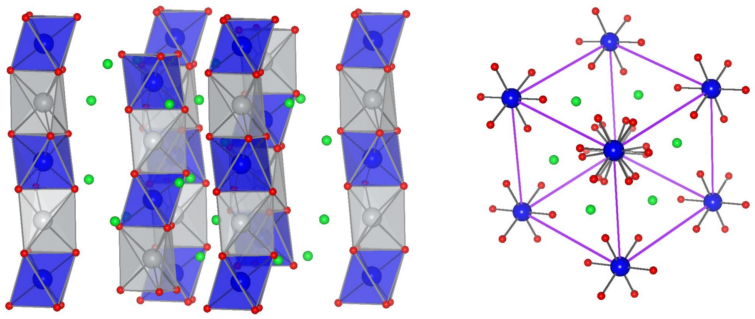

Figure 5.1 Left Panel: Crystal structure of $A_3BB'O_6$ compounds, showing the chains running along the vertical direction. Right Panel: Hexagonal packing of chains viewed along the chain direction. The blue and grey colored balls denote B′ and B atoms, while red colored, small balls denote the shared oxygen atoms. A atoms, sitting in the hollows in between the chains are indicated as green colored balls.

5.2 Results and Discussions

5.2.1 Crystal Structure

These compounds form K_4CdCl_6-type structures consisting of $(BB'O_6)^{-6}$ chains formed by alternating face sharing BO_6 trigonal prism and $B'O_6$ octahedra. The chains are separated from each other by the A^{2+} cations and form a hexagonal arrangement while viewed along the chain direction as shown in Fig. (5.1). Both Sr_3NiPtO_6 and Sr_3NiIrO_6 crystallize in rhombohedral crystal structure [12] with space group $R\bar{3}c$ consisting of perfectly linear Ni-B′-Ni (where B′=Pt, Ir) chains with 180^o ∠Ni-B′-Ni as shown in Fig. (5.2). Sr_3CuPtO_6 shows deviation from this general structure. It consists of zig-zag Cu-Pt-Cu chains with Cu-Pt-Cu angle deviating significantly from 180^o, as shown in Fig. (5.2). This also destroys the perfect hexagonal arrangement of the chains in plane perpendicular to chain direction. The distortion causes lowering of the space group symmetry from rhombohedral to monoclinic space group [12] of C*12*/c1.

Since the positions of light atoms are often not well characterized by X-ray diffraction, we have carried out the structural optimization of all three compounds relaxing the internal positions and keeping the lattice parameters fixed at the experimental values [12, 24, 16]. Table. 5.1 lists the optimized coordinates.

Table 5.1 Energy-minimized structural parameters of Sr_3NiPtO_6, Sr_3CuPtO_6 and Sr_3NiIrO_6. Lattice constants have been kept fixed at the experimental values [12, 24, 16].

Sr_3NiPtO_6							
a(Å)	c(Å)				x	y	z
9.583	11.196			Sr	0.364	0.0	0.25
				Ni	0.0	0.0	0.25
				Pt	0.0	0.0	0.0
				O	0.175	0.023	0.114
Sr_3CuPtO_6							
a(Å)	b(Å)	c (Å)	β		x	y	z
9.324	9.729	6.696	90.918°	Sr1	0.314	0.073	0.622
				Sr2	0.0	0.105	0.25
				Cu	0.5	0.202	0.25
				Pt	0.25	0.25	0.0
				O1	0.213	0.314	0.714
				O2	0.356	0.428	0.073
				O3	0.055	0.339	0.050
Sr_3NiIrO_6							
a(Å)	c(Å)				x	y	z
9.586	11.132			Sr	0.364	0.0	0.25
				Ni	0.0	0.0	0.25
				Pt	0.0	0.0	0.0
				O	0.172	0.022	0.116

It was found that, the relaxed parameters associated with oxygen positions change by at most 3%, compared to experimentally measured parameters. Table. 5.2 lists selected bond lengths and bond angle for the three compounds. For both Sr_3NiPtO_6 and Sr_3NiIrO_6 the trigonal prism is perfect with equal Ni-O bond lengths and O-Ni-O angles, while the octahedra has trigonal distortion with $\angle$O-B′-O (B′=Pt, Ir) deviating from 90^o. For Sr_3CuPtO_6 both the trigonal prism as well as the octahedra are

Table 5.2 Selected bond lengths and bond angles for the optimized crystal structure of Sr_3NiPtO_6, Sr_3CuPtO_6 and Sr_3NiIrO_6.

	Sr_3NiPtO_6	Sr_3CuPtO_6	Sr_3NiIrO_6
$B'O_6$ octahedron			
∠ O-B′-O	84.52°, 95.34° 84.52°, 95.34° 84.52°, 95.34°	80.63°, 99.36° 87.69°, 92.30° 87.11°, 92.88°	84.65°, 95.34° 84.65°,95.34° 84.65°, 95.34°
B′-O distance (Å)	2.02	2.03,2.02,2.04	2.00
O-O distance (Å)	2.72, 3.00	2.93, 2.81 2.94, 3.09 2.80, 2.62	2.70 , 2.96
BO_6 trigonal prism			
∠ O-O-O	60.0°	62.48°, 61.83° 55.68°	60.0°
B-O distance (Å)	2.19	2.80, 2.02, 1.99	2.18
O-O distance (Å)	2.72 3.06	2.80,2.81,2.62 3.52, 3.50, 3.50	2.70 3.06
B-B′ chain			
∠ B′-B-B′	180°	161.37°	180°

highly distorted. In addition to trigonal distortion, the PtO_6 octahedra shows signature of small further distortions resulting in slightly different pairs of Pt-O bond lengths. The trigonal prism is also highly distorted with Cu atom not being at the centre of the prism and ∠O-O-O being different from 60^o.

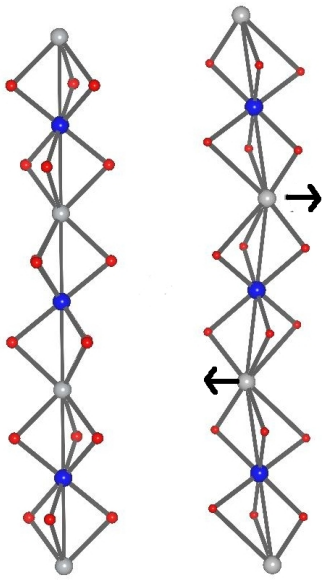

Figure 5.2 Comparison of $BB'O_6^{-6}$ chains in Sr_3NiPtO_6 and Sr_3NiIrO_6 compounds (left panel) and in Sr_3CuPtO_6 compound (right panel). The color convention is same as in Fig. (5.1).

5.2.2 Electronic Structure

Fig. (5.3) and Fig. (5.4) show the non-spin polarized GGA [25] density of states (DOS) and band structure for the three compounds, computed in linear muffin-tin orbital (LMTO) basis [17, 18]. Self consistency was achieved through Brillouin zone (BZ) integrations over $8 \times 8 \times 8$ k-points. The density of states consist of hybridized states ranging from -6 eV below to 7 eV above of the Fermi level (E_f) which is set at zero. The Sr dominated states for all three compounds are empty, lying far away from the Fermi level (E_f) with very little contribution to states close to E_f, in conformity with the nominal Sr^{+2} valence. For Sr_3NiPtO_6 and Sr_3CuPtO_6 compounds, the states at E_f are dominated by Ni and Cu d states respectively, while for Sr_3NiIrO_6 the states at E_f are contributed by both Ni and Ir d character. In case of Sr_3NiPtO_6 and Sr_3CuPtO_6, Pt dominated states are mainly divided in completely filled t_{2g} states and completely empty e_g states. Ni, Cu and Ir-d states show significant mixing with oxygen character. The band structure plots show the m-decomposed contribution of d-levels at B and B$'$ sites, as well as O-p and Sr dominated characters. B$'$ site being in octahedral environment, the d states are broadly split into B$'$-t_{2g} and B$'$-e_g while the splitting of d-levels at B site is different due to trigonal

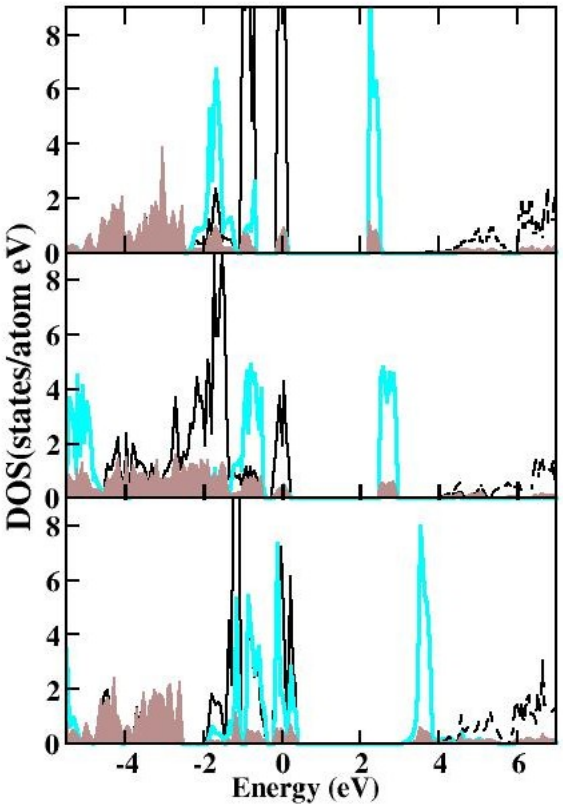

Figure 5.3 Non-spin polarized DOS calculated within GGA. B′-*d* states, B-*d* states, Sr-*s* and O-*p* states are presented by solid black lines, cyan lines, broken black lines and filled brown lines respectively. The zero of the energy is set at E_f. From top to bottom, the three panels correspond to plots for Sr_3NiPtO_6, Sr_3CuPtO_6 and Sr_3NiIrO_6 compounds respectively.

prismatic environment of the surrounding oxygen atoms [26]. The orbital characters as marked in Fig. (5.4), are obtained in the local co-ordinate systems with local z-axis pointing along the B′ to apical O and the local y-axis pointing approximately along the B′-inplane O direction for the B′ site. For the B site, the local z-axis is chosen to point along the chain direction and the local y-axis is chosen to point along approximately in plane B-B direction. For the case of Sr_3NiPtO_6, four half-filled bands cross E_f which consist of Ni-d_{yz} and Ni- d_{xz} and contributed by two Ni atoms in the unit cell. The Pt-t_{2g} levels appear below all the Ni-*d* dominated states completely occupied, while Pt-e_g states remain empty with large crystal field splittings of about 4 eV. On the other hand for Sr_3CuPtO_6, two bands cross E_f contributed by Cu-d_{xz} character and two Cu atoms in the unit cell. Pt t_{2g} dominated bands unlike Sr_3NiPtO_6 appear in between the crystal field split levels of Cu-*d* with Pt e_g states being empty

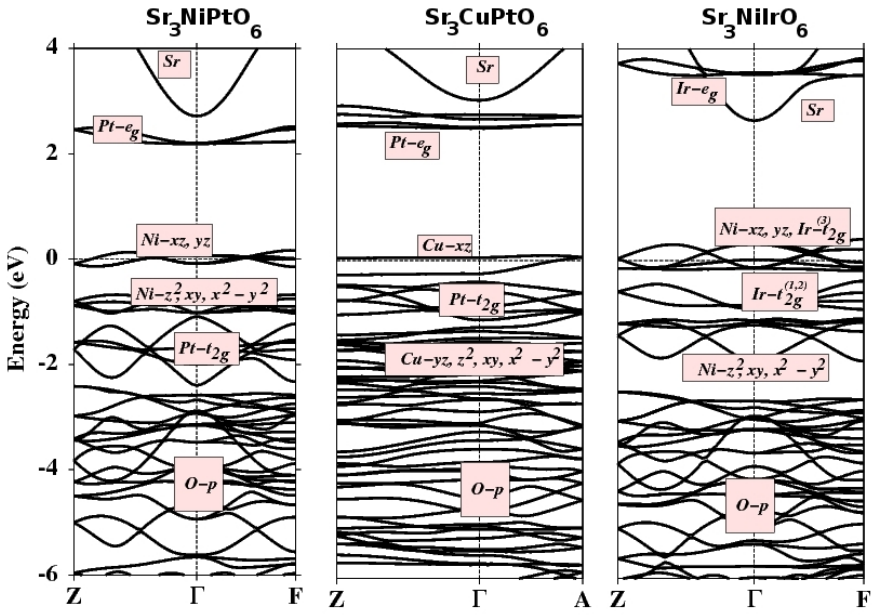

Figure 5.4 Non-spin polarized band-structure calculated within GGA. The dominant orbital characters for the bands are indicated. Zero of the energy is set at E_f. From left to right, the three panels correspond to plots for Sr_3NiPtO_6, Sr_3CuPtO_6 and Sr_3NiIrO_6 respectively.

and with a t_{2g}-e_g crystal field splitting of about 4 eV. For Sr_3NiIrO_6, six bands cross E_f, four of them are contributed by Ni-d_{yz} and Ni-d_{xz} character and two contributed by Ir-t_{2g} character. The rest of the Ir-t_{2g} dominated bands appear in between the crystal field split Ni-d levels. Ir t_{2g}-e_g splitting turn out to be about 4 eV. Note that within ordinary non spin polarized electronic structure calculation the three compounds turn out to be metallic, which is due to insufficient treatment of electron-electron correlation in the GGA approximation. Interestingly, within the GGA spin-polarized calculations the three systems turn out to be insulator.

5.2.3 Magnetic Property

The ground state magnetic structure in these compounds are very controversial [13, 27, 14] and form one of the most interesting parts of the study of these systems. The spin-polarized electronic structure calculations are helpful to decide on the spin state of the component ions. Table. 5.3 shows the calculated magnetic moments at B, B′ and O sites, as obtained in spin- polarized GGA calculations. From our calculated magnetic moment we find that both Pt^{4+} with $d^{\,6}$ configuration and Ir^{+4} ion with $d^{\,5}$

Table 5.3 Magnetic Moments at B, B′ and O sites, as obtained in spin-polarized GGA calculations.

	Magnetic moment in μ_B		
	Sr_3NiPtO_6	Sr_3CuPtO_6	Sr_3NiIrO_6
B	1.43	0.50	1.34
B′	0.02	0.02	0.81
O	0.08	0.06	0.14

configuration are in low spin states, giving rise to S=0 and S=1/2 spin states respectively. The magnetic moments at Ni^{2+} with $d^{\,8}$ configuration and Cu^{2+} with $d^{\,9}$ configuration suggest S=1 and S=1/2 spin states respectively. Non negligible moments at oxygen sites indicate substantial hybridization between oxygen and Ni or Cu or Ir degrees of freedom, as has been pointed out already. Sr_3NiPtO_6 and Sr_3CuPtO_6 compounds therefore represent the case with B being occupied by the magnetic ion, B′ being non-magnetic while Sr_3NiIrO_6 gives rise to a situation where both B and B′ are magnetic.These results indicate that Sr_3NiPtO_6 compound behaves like 1-0-1-0-1-0 type of spin chain structure, whereas $\frac{1}{2}$-0-$\frac{1}{2}$-0-$\frac{1}{2}$-0 type spin chain structure in case of Sr_3CuPtO_6 compound and 1-$\frac{1}{2}$-1-$\frac{1}{2}$-1-$\frac{1}{2}$ type spin chain structure in case of Sr_3NiIrO_6 compound.

5.2.4 Low Energy Hamiltonians and Hopping Interactions

Fig. (5.5) shows the energy level diagram and their occupancies for both B and B′ sites as obtained in the NMTO downfolding [19] calculation for the three compounds. Due to the presence of finite distortion, the levels are not of pure character but are of mixed character. What is indicated for each level is the dominated character. Since the $B'O_6$ octahedra for Sr_3NiPtO_6 and Sr_3NiIrO_6 compounds have trigonal distortion, the three t_{2g} states get mixed and one should designate them by double degenerate e_g^{π} and singly degenerate a_{1g} symmetries. Here we prefer to designate them as $t_{2g}^{(1)}$, $t_{2g}^{(2)}$ and $t_{2g}^{(3)}$, and the similarly, $e_g^{(1)}$ and $e_g^{(2)}$, for the e_g^{σ} levels. In case of Sr_3CuPtO_6 compound, due to additional distortion, the degeneracies get completely lifted. The spin models for the Sr_3NiPtO_6, Sr_3CuPtO_6, Sr_3NiIrO_6 compounds therefore can be constituted in terms of Ni- d_{yz} and d_{xz} degrees of freedom, Cu-d_{xz} degree of freedom, and Ni-d_{yz} and Ni-d_{xz} degrees of freedom combined with Ir-$t_{2g}^{(3)}$ degrees of freedom,

Table 5.4 List of dominant hopping interactions for the three compounds. In case of Sr_3NiPtO_6, hoppings are defined between Ni-d_{xz}/d_{yz} and Ni-d_{xz}/d_{yz}. In case of Sr_3CuPtO_6, hoppings are defined between Cu-d_{xz} and Cu-d_{xz}.

Sr_3NiPtO_6				
Distance(Å)	(connecting vector)			
Hopping Int. (meV)				
5.60	$(0\ 0\ 1)$	$(0\ 0\ -1)$	...	...
t_1 (Intra chain)	$\begin{pmatrix} 37.9 & 0.0 \\ 0.0 & 37.9 \end{pmatrix}$	$\begin{pmatrix} 37.9 & 0.0 \\ 0.0 & 37.9 \end{pmatrix}$		
6.67	$(-1\ 0\ -.68)$	$(1\ 0\ .68)$	...	...
t_2 (Inter chain)	$\begin{pmatrix} 15.4 & -8.9 \\ 8.9 & -2.7 \end{pmatrix}$	$\begin{pmatrix} 15.4 & 8.9 \\ -8.9 & -2.7 \end{pmatrix}$		
6.67	$(.5\ -.87\ -.68)$	$(.5\ .87\ .68)$	$(-.5\ -.87\ .68)$	$(-.5\ .87\ .68)$
t_3 (Inter chain)	$\begin{pmatrix} 1.8 & -1.1 \\ 16.7 & 10.8 \end{pmatrix}$	$\begin{pmatrix} 1.8 & -16.7 \\ 1.1 & 10.8 \end{pmatrix}$	$\begin{pmatrix} 1.8 & 1.1 \\ -16.7 & 10.8 \end{pmatrix}$	$\begin{pmatrix} 1.8 & 16.7 \\ -1.1 & 10.8 \end{pmatrix}$
Sr_3CuPtO_6				
Distance (Å)	(connecting vector)			
Hopping Int. (meV)				
5.77	$(-.48\ -.1\ -.34)$	$(.48\ -.1\ .34)$		
t_1 (Intra Chain)	68.5	68.5		
6.69	$(0\ 0\ -.69)$	$(0\ 0\ .69)$		
t_2 (Inter chain)	31.1	-31.1		
9.32	$(0\ 0\ -.69)$	$(0\ 0\ .69)$		
t_3 (Inter chain)	12.5	-12.5		

Table 5.5 List of dominant hopping interactions for Sr_3NiIrO_6. Hoppings are defined between Ni-d_{xz}/d_{yz} and Ir-$t_{2g}^{(3)}$ (t_1)as well as between Ni-d_{xz}/d_{yz} and Ni-d_{xz}/d_{yz} (t_5), and between Ir-$t_{2g}^{(3)}$ and Ir-$t_{2g}^{(3)}$ (t_2,t_3, t_4).

Sr_3NiIrO_6		
Distance (Å) Hopping Int. (meV)	(connecting vector)	
2.78	$(0\ 0\ -.5)$	$(0\ 0\ .5)$
t_1 (Intra chain)	$\begin{pmatrix} 39.8 \\ 56.9 \end{pmatrix}$	$\begin{pmatrix} 39.8 \\ -56.9 \end{pmatrix}$
5.56	$(0\ 0\ 1)$	$(0\ 0\ -1)$
t_2 (Inter chain)	-18.0	-18.0
5.83	$(-.5\ .87\ -.34)$	$(-.5\ -.87\ -.34)$
t_3(Inter chain)	8.4	8.4
6.66	$(.5\ -.87\ -.67)$	$(-.5\ .87\ .67)$
t_4(Inter chain)	13.8	13.8
5.56	$(0\ 0\ -1)$	$(0\ 0\ 1)$
t_5 (Intra chain)	$\begin{pmatrix} 92.9 & 5.9 \\ 5.9 & 85.3 \end{pmatrix}$	$\begin{pmatrix} 92.9 & -5.9 \\ -5.9 & 85.3 \end{pmatrix}$

respectively. For this purpose we carried out NMTO-downfolding calculation starting from full DFT calculations.

In the downfolding calculations, we have kept only Ni-d_{yz} and Ni-d_{xz} degrees of freedom active in case of Sr_3NiPtO_6, Cu-d_{xz} degrees of freedom active in case of Sr_3CuPtO_6 and Ni-d_{yz} and Ni-d_{xz} and Ir-$t_{2g}^{(3)}$ degrees of freedom active in case of Sr_3NiIrO_6 compound and downfolded all other degrees of freedom. Therefore the resultant low energy Hamiltonians become 4×4, 2×2 and 6×6 dimensional matrices in three cases respectively. Diagonalization of these Hamiltonians at various k-points produce the downfolded band structure which are in excellent agreement with full DFT band structure as shown in Fig. (5.6).

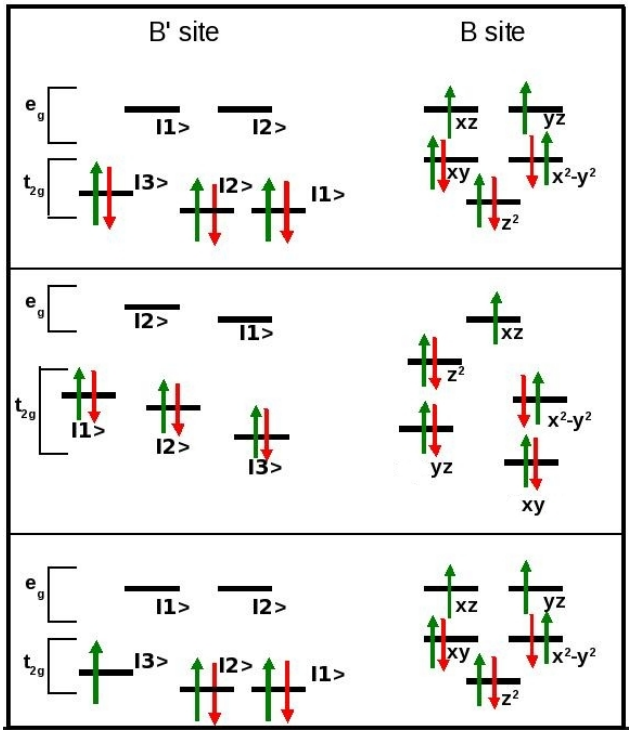

Figure 5.5 The energy levels of B and B′ *d* levels in eV unit and their occupancies. From top to bottom, the three panels correspond to plots for Sr_3NiPtO_6, Sr_3CuPtO_6 and Sr_3NiIrO_6 respectively.

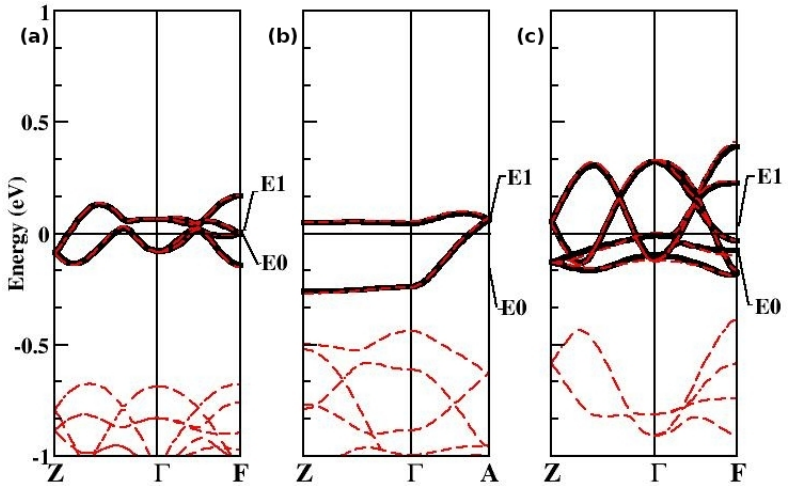

Figure 5.6 Bands obtained with downfolded basis (solid lines) compared to full DFT band structure (dashed lines). The energy points, marked as E_0 and E_1 in each panel, denote the energy points used in NMTO calculation. From left to right, the three panels correspond to plots for Sr_3NiPtO_6, Sr_3CuPtO_6 and Sr_3NiIrO_6 respectively.

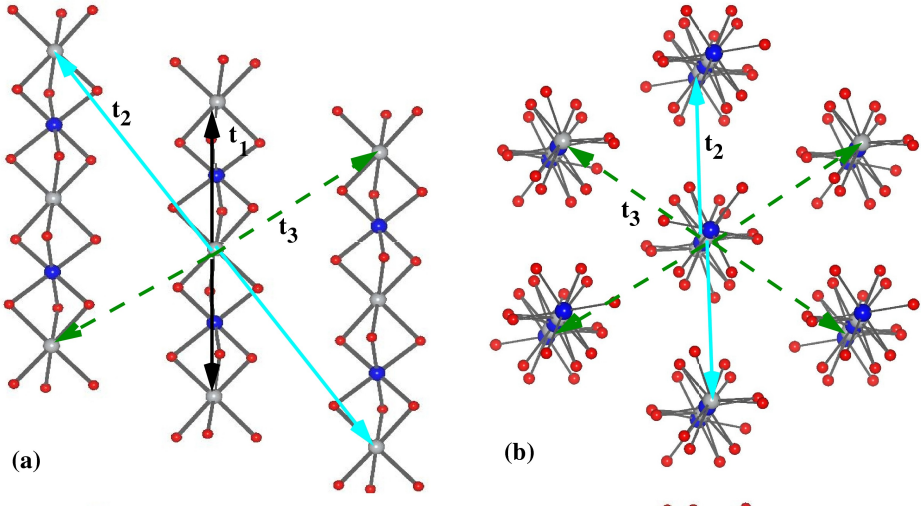

Figure 5.7 Panels (a) and (b): Ni-Ni hopping interaction paths, t_n in Sr_3NiPtO_6. Panels (a) and (b) show perspectives showing the chains and that viewed along the chain direction, showing the hexagonal packing. The color convention of atoms is same as in Fig. (5.1).

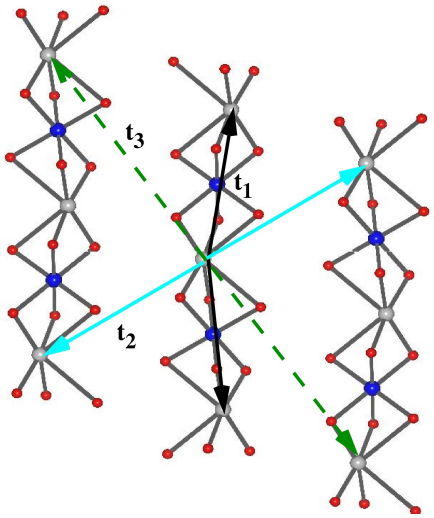

Figure 5.8 Cu-Cu interaction paths, t_n in Sr_3CuPtO_6. The color convention of atoms is same as in Fig. (5.1).

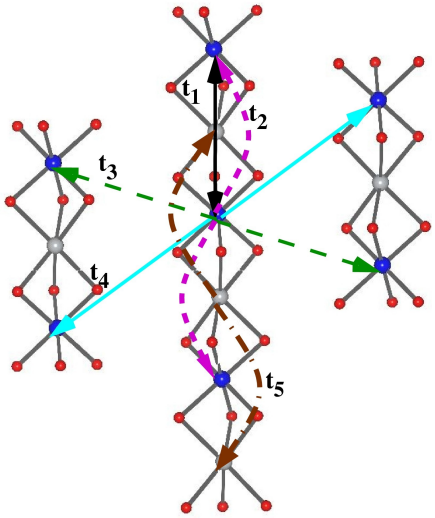

Figure 5.9 Ni-Ni, Ni-Ir and Ir-Ir interaction paths, t_n in Sr_3NiIrO_6. The color convention of atoms is same as in Fig. (5.1).

Table. 5.4 and 5.5 lists the dominant hopping interactions and Fig. (5.7), Fig. (5.8) and Fig. (5.9) show the corresponding hopping paths. Calculated results show that the strongest hopping interaction is the intra-chain interaction for all the three compounds.

Fig. (5.10) to Fig. (5.12) shows the overlap of effective Wannier functions, defining the exchange paths for the intra-chain interactions for the three compounds respectively. The central part of the Wannier functions are shaped according to Ni-d_{xz}/d_{yz} or Cu-d_{xz} or Ir-$t_{2g}^{(3)}$ symmetries and the tails sitting at neighboring sites are shaped according to integrated out degrees of freedom. In case of Sr_3NiPtO_6 and Sr_3CuPtO_6, as is evident from Fig. (5.10) and Fig. (5.11) the overlap of two neighboring Ni-d_{xz} or Ni-d_{yz} Wannier functions with each other and two Cu-d_{xz} Wannier functions respectively, the exchange paths are formed by Ni-O-O-Ni and Cu-O-O-Cu super- super-exchanges, respectively. Small but non-zero weights are seen at intervening Pt sites too, for both the cases. For Sr_3NiIrO_6 compound, the exchange path formed by the overlap of Ni-d_{xz}/d_{yz} Wannier functions with neighboring Ir-$t_{2g}^{(3)}$ Wannier function, is mediated through the connecting oxygens as well as through direct overlap of Ni-d_{xz}/d_{yz} with Ir-$t_{2g}^{(3)}$, evidenced by the presence of finite weights of the tails belonging to Ni(Ir) Wannier function at Ir(Ni) site, as shown in Fig. (5.12). Examination of hopping interactions indicate also presence of rather large Ni-Ni interactions (t_5) mediated by both oxygen and Ir.

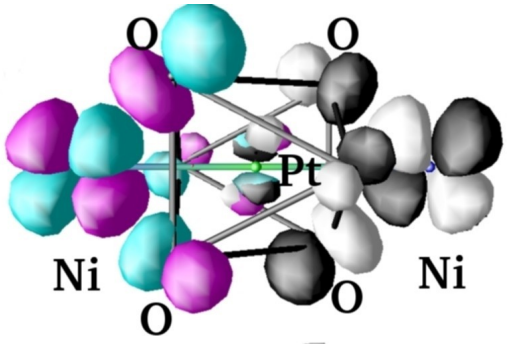

Figure 5.10 Effective orbitals corresponding to the downfolded d_{xz} NMTOs, placed at two Ni sites situated in a given chain. An equivalent super-exchange path exists, created by overlap of two Ni downfolded d_{yz} NMTOs. Lobes of orbitals placed at different sites are colored differently. Lobe colored black (white) at one site represents the same sign as that colored magenta (cyan) at other neighboring site.

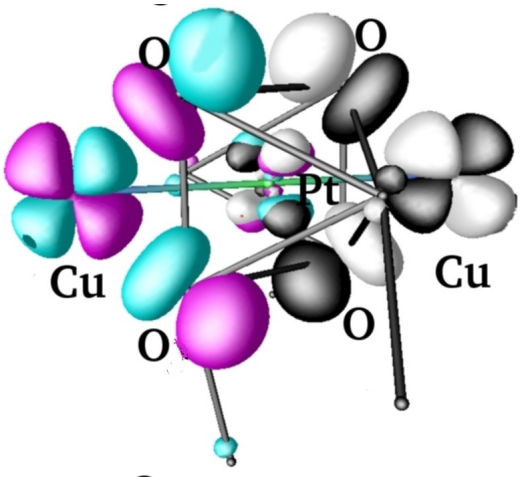

Figure 5.11 Effective orbitals corresponding to the downfolded d_{xz} NMTOs, placed at two Cu sites situated in a given chain. An equivalent super-exchange path exists, created by overlap of two Cu downfolded d_{yz} NMTOs. Lobes of orbitals placed at different sites are colored differently. Lobe colored black (white) at one site represents the same sign as that colored magenta (cyan) at other neighboring site.

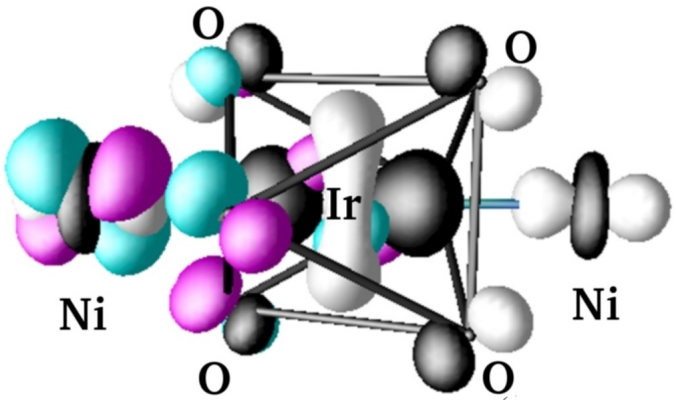

Figure 5.12 Overlap of effective orbital corresponding to the downfolded Ni-d_{xz} and Ir-$t_{2g}^{(3)}$ NMTOs placed at neighboring sites within a chain. Other intra-chain super-exchange paths involve overlap of Ni-d_{yz} with Ir-$t_{2g}^{(3)}$ and Ni-d_{xz}/d_{yz} with Ni-d_{xz}/d_{yz}. Lobes of orbitals placed at different sites are colored differently. Lobe colored black (white) at one site represents the same sign as that colored magenta (cyan) at other neighboring site.

For the Sr_3NiPtO_6 and Sr_3NiIrO_6 compounds, the inter-chain hoppings turn out to be considerably smaller compared to the intra-chain hoppings, while for Sr_3CuPtO_6 compound, the inter-chain interactions turn out to be significant fraction of the intra-chain interaction. The facts that the inter-chain interactions are significant and, that Sr_3CuPtO_6 should not be considered as magnetically one dimensional, have been pointed out in past studies [12, 14] using fitting of the susceptibility data.

5.2.5 Magnetic Interaction

Given the knowledge of hopping interactions, it is possible to calculate the magnetic interactions, employing the super-exchange expressions which requires knowledge of charge transfer energies. However, because of the complicated exchange paths, such charge transfer energies are not easy to estimate. We therefore attempted to estimate the magnetic interaction using the total energy calculation of various spin configurations and mapping the DFT total energy to corresponding Ising Model [28]. Calculations have been carried out within the framework of plane wave basis in VASP [20] within GGA. Though such a scheme is also faced with several difficulties like the choice of spin configurations, choice of basis set and exchange-correlation functional, it is expected to provide us with indicative estimates. The total energy calculations show the strongest intra-chain interaction, J, for Sr_3NiPtO_6 and Sr_3CuPtO_6 compounds to be of antiferromagnetic nature with values 1.12 meV and 2.25 meV respectively and of

ferromagnetic nature for Sr_3NiIrO_6 compound. For Sr_3NiIrO_6 compound, we failed to stabilize any other magnetic configuration, other than ferromagnetic alignment of Ni and Ir spins along a chain. Any other chosen configuration, converged to ferromagnetic solution, proving the robustness of the ferromagnetic alignment of Ni and Ir spins over other solutions. In order to check the influence of correlation effect beyond GGA approach on the magnetic interactions, we have repeated the calculations within GGA+U framework [29] as well. The calculations were carried out for two choice of U values at B site (U=3.5 eV and U=5 eV), keeping U value at B′ site to be fixed at 1.5 eV. The Hund's exchange J_H was chosen to be 0.8 eV. As expected, the values of the dominant intra- chain magnetic exchanges, which are of antiferromagnetic nature for Sr_3NiPtO_6 and Sr_3CuPtO_6 compounds, were found to decrease with increasing U values, with values 0.94 meV for U=3.5 eV and 0.61 meV for U=5eV for Sr_3NiPtO_6, and 2.12 meV for U=3.5 eV and 1.57 meV for U=5 eV for Sr_3CuPtO_6. For Sr_3NiIrO_6, even with application of U, we failed to stabilize any other configuration other than ferromagnetic arrangement between Ir and Ni spins.

The antiferro and ferromagnetic nature of intrachain interactions may be understood considering the energy level diagrams as shown in Fig. (5.5) and the exchange paths shown in Fig. (5.10) to Fig. (5.12). For Sr_3NiPtO_6 compound the intra-chain Ni-Ni interaction occurs between half filled Ni-$d_{xz}/_{yz}$ levels through the oxygen-mediated super-exchange paths as shown in Fig. (5.10), which according Kugel-Khomskii-like picture [30] would give rise to antiferromagnetic interaction. Similarly the intra-chain Cu-Cu interaction in case of Sr_3CuPtO_6 compound occurs between half filled Cu-d_{xz} levels through the super-exchange path shown in Fig. (5.11), giving rise to antiferromagnetic interaction. For Sr_3NiIrO_6 compound, while the exchange occurring between half filled Ni-$d_{xz}/_{yz}$ and Ir-$t_{2g}^{(3)}$ is of antiferromagnetic nature but there exist an another possible exchange interaction between half filled Ni-$d_{xz}/_{yz}$ and empty Ir-e_g^{σ} states which according to Kugel-Khomskii picture, would be ferromagnetic in nature. The later exchange, though, is expected to be weak due to large energy separation between Ni-$d_{xz}/_{yz}$ and Ir-e_g^{σ} levels. We, however, notice a direct exchange path between Ni-$d_{xz}/_{yz}$ and Ir-$t_{2g}^{(3)}$, as described previously, which would give rise to ferromagnetic contribution. Interestingly, intra-chain Ni-Ni interaction (the magnetic interaction, corresponding to the hopping t_5) also turned out to be ferromagnetic, presumably due to substantial contribution through path involving Ir. Our obtained result of ferromagnetic intra-chain interaction is in contradiction with that obtained in theoretical study of

Table 5.6 Spin and orbital moments in μ_B as obtained in GGA+SO calculations for the three compounds.[31] The magnetic anisotropy energies are also listed.

		Sr_3NiPtO_6		Sr_3CuPtO_6		Sr_3NiIrO_6	
Spin quantization axis		Direction with respect to B - B′ chain					
		∥	⊥	∥	⊥	∥	⊥
Orbital Moment	B	0.22	0.16	0.13	0.13	0.21	0.27
	B′	0.0	0.0	0.0	0.0	-0.01	-0.11
Spin Moment	B	1.46	1.46	0.53	0.50	1.39	1.46
	B′	0.02	0.02	0.02	0.03	0.41	0.42
Anisotropy energy $E = E_{\parallel} - E_{\perp}$		- 0.75 meV		- 0.12 meV		13.5 meV	

Ref. [23]. The conclusions inferred from the experimental data, are debated with some supporting ferromagnetic intra-chain interaction [16] and others proposing antiferromagnetic intra-chain interaction [15]. Further experiments are necessary to resolve this controversy. The small inter-chain interaction in case of Sr_3NiPtO_6 compound turned out to be ferromagnetic nature, with value 0.10 meV. The substantial inter-chain interaction (J′) in the case of Sr_3CuPtO_6 compound turned out to be antiferromagnetic nature, with value 0.65 meV, giving rise to a ratio of $J/J' \approx 3.5$, in good agreement with the estimates obtained from the analysis of magnetic measurements [12, 14]. The inter- chain interactions for Sr_3NiIrO_6, on the other hand, turned out to be antiferromagnetic, presumably explaining the signature of antiferromagnetic couplings observed in experiments [15].

5.2.6 Spin-Orbit Interaction

The importance of spin-orbit interaction and single-ion anisotropy in these compounds have been discussed in literature [12, 27]. In order to investigate that we carried out calculations within the framework of GGA+SO. The calculations have been carried out using the linear augmented plane wave (LAPW) basis as implemented within WIEN2K code [21]. The number of plane waves were restricted using the criteria muffin- tin radius multiplied k_{max} yielding a value of 7. The spin quantization axis

was chosen to be parallel to the direction of the chain as well as perpendicular to the chain direction. Table. 5.6 lists spin and orbital moments at B and B′ sites, as obtained within GGA+SO calculations. We find rather large orbital moments at Ni and Cu sites, pointing parallel to the spin moment due to more than half-filled nature of Ni or Cu *d* occupancies. The orbital moment at Pt site is negligibly small due to the completely filled t_{2g} occupancies, while that of Ir site is large which point opposite to the spin moment. The substantial orbital moment at Ni site is unexpected due to its d^8 configuration and the trigonal prismatic environment driven splitting of energy levels which results in complete quenching of the orbital degree of freedom. The presence of finite and substantially large orbital moment at Ni site [32] therefore needs to be justified as an induced mechanism due to the mixing of the ligand, namely O-*p* orbitals. Similar situation is expected to occur for Cu which is in d^9 state with quenched orbital degrees of freedom. The magneto-crystalline anisotropy obtained by taking the energy difference between calculations with spin quantization chosen along the chain direction and perpendicular to the chain direction yields values 0.75 meV per Ni ion for Sr_3NiPtO_6, 0.12 meV per Cu ion for Sr_3CuPtO_6 and 13.5 meV per formula unit for the Sr_3NiIrO_6 compound. In case of Sr_3NiPtO_6 and Sr_3CuPtO_6 compounds, the spin quantization is found to be favored along the chain direction, giving rise to an easy axis scenario while for Sr_3NiIrO_6 compound the spin quantization favors lying in the plane perpendicular to the chain direction giving rise to easy plane scenario. The magneto-crystalline anisotropy is large for Sr_3NiIrO_6 compound with both Ni and Ir contributing, comparatively smaller for Sr_3NiPtO_6 and a tiny one for Sr_3CuPtO_6 compound. In order to check the influence of missing correlation effect in magneto-crystalline anisotropy energy, as in case of magnetic interactions, we have repeated the calculations within the framework of GGA+U+SO. While the quantitative values were found to decrease upon application of U, the trend was found to remain intact. The experimental study carried out for Sr_3NiPtO_6 predicted [12] the easy plane scenario on the basis of susceptibility measurement and fit carried out with an assumed model. Our obtained parameters for Sr_3NiPtO_6, therefore will be important to resolve whether the experimental results should be interpreted in terms of a non-trivial spin liquid state of an easy axis magnet or a simple easy-plane single ion effect.

5.3 Conclusion

To conclude, using first-principles DFT calculations, we have investigated the electronic structure of three compounds, Sr_3NiPtO_6, Sr_3CuPtO_6 and Sr_3NiIrO_6, belonging to the class of low- dimensional quantum spin systems of general formula, $A_3BB'O_6$. Analyzing the results of electronic structure calculations in terms of formation of low-energy Hamiltonians defined in the basis of effective Wannier functions and calculation of magnetic interactions in terms of total energy calculations, we derived the underlying spin model for each of these compounds. The magneto-crystalline anisotropy energies were evaluated from calculations in presence of SOC. The intra-chain interactions are found to be the dominant interactions in all three cases, which turned out to be of antiferromagnetic nature for Sr_3NiPtO_6 and Sr_3CuPtO_6 compounds, and to be of ferromagnetic nature for Sr_3NiIrO_6 compound. The inter-chain interactions are found to be small and of ferromagnetic nature for Sr_3NiPtO_6 compound, substantially large and of antiferromagnetic nature for Sr_3CuPtO_6 compound, and of antiferromagnetic nature for Sr_3NiIrO_6 compound. Large anisotropy is found for Sr_3NiIrO_6 compound, with appreciable value for Sr_3NiPtO_6 compound and a small value for Sr_3CuPtO_6 compound. The magnetic anisotropy is found to be of easy axis in case of Sr_3NiPtO_6 and Sr_3CuPtO_6 compounds, while it is found to be of easy plane for Sr_3NiIrO_6 compound. While some of our results are in agreement with existing experimental observations, some are not [12, 14, 16, 15]. Our detailed investigation, therefore, form the basis for further experimental investigations. It also provides the basis for further theoretical studies in terms of solution of the proposed spin models which can give rise to a variety of properties in the parameter space of intra- and inter-chain interactions as well as easy axis versus easy plane situations.

Bibliography

[1] P. Lemmens, G. Guntherodt, and C. Gros, Phys. Rep. **375**, 1 (2003).

[2] Hua Wu, M. W. Haverkort, Z. Hu and D.I. Khomskii, L.H. Tjeng, Phys. Rev. Lett. **95**, 186401 (2005).

[3] Jiming An and C.-W. Nan, Solid State Communication **129**, 51-56 (2004).

[4] M.-H. Whangbo, D. Dai, H.-J. Koo and S. Jobic, Solid State Communication **125**, 413-417 (2003).

[5] Raymond Fresard, Christian Laschinger, Thilo Kopp and Volker Eyert, Phys. Rev. B **69**, 140405(R) (2004).

[6] Hua Wu, Z. Hu, I. Khomskii and L.H. Tjeng, Phys. Rev. B **75** 245118 (2007).

[7] E. V. Sampathkumaran and Asad Niazi, Phys. Rev. B **65**, 180401(R) (2002).

[8] Hua Wu, T. Burnus, Z. Hu, C. Martin, A. Maignan, J. C. Cezar, A. Tanaka, N. B. Brookes, D. I. Khomskii and L. H. Tjeng, Phys. Rev. Lett. **102**, 026404 (2009).

[9] Y.J. Choi, H. T. Yi, S. Lee, Q. Huang, V. Kiryukhin and S.-W. Cheong, Phys. Rev. Lett. **100**, 047601 (2008).

[10] C. Lampe-Onnerud, M. Sigrist and H. Loye, J. of Solid State Chemistry **127**, 25-30(1996); S. Rayaprol, K. Sengupta, E.V Sampathkumaran and Y.Matsushita J. of Solid State Chemistry **177**, 3270-3273 (2004); M. D. Smith and H. Loye, Chem. Mater. **12**, 2404-2410 (2004); V. Eyert, U. Schwingenschlögl, R. Fresard, A. Maignan, C. Martin, N. Nguyen, C. Hackenberger, and T. Kopp, Phy. Rev. B **75**, 115105 (2007); S. Kawasaki and M. Takano, J. of Solid State Chemistry **145**, 302-308 (1999).

[11] K.E. Stitzer, J. Darriet and H.-C. zur Loye, Current Opinian in Solid state and Materials Science, **5**, 535-544 (2001).

[12] John B. Claridge, Ralph C. Layland, W. Hampton Henley and Hans-Conrad zur Loye, Chem. Mater. **11**, 1376-1380 (1999).

[13] Niharika Mohapatra, Kartik K. Iyer, Sudhindra Rayaprol and E. V. Sampathkumaran, Phys. Rev. B **75**, 214422 (2007).

[14] S. Majumdar, V. Hardy, M. R. Lees and D. McK. Paul, Phys. Rev. B **69**, 024405 (2004).

[15] D. Flahaut, S. Hebert, A. Amignan, V. Hardy, C. Martin, M. Hervieu, M. Costes, B. Raquet and J.M. Broto, Euro. Phys. J. B . **35**, 317-323 (2003).

[16] T. N. Nguyen and H.-C. zur Loye, J. Solid State Chem. **117**, 300-308 (1995).

[17] O. K. Andersen, Phys. Rev. B **12**, 3060 (1975).

[18] O. K. Andersen and O. Jepsen, Phys. Rev. Lett. **53**, 2571 (1984).

[19] O. K. Andersen and T. Saha-Dasgupta, Phys. Rev. B **62**, R16 219 (2000).

[20] G. Kresse and J. Hafner, Phys. Rev. B **47**, R558 (1993); G. Kresse and J. Furthmuller, Phys. Rev. B **54**, 11169 (1996).

[21] P. Blaha, K. Schwartz, G. K. H. Madsen, D. Kvasnicka, and J. Luitz, WIEN2K, An Augmented Plane Wave + Local Orbitals Program for Calculating Crystal Properties, edited by K. Schwarz, Technische Universität Wien, Austria, 2001.

[22] Sudhir K. Pandey and Kalobaran Maiti. Euro physics. Lett. **88**, 27002 (2009).

[23] G. R. Zhang, X. L. Zhang, T. Jia, Z. Zeng and H. Q. Lin, J. Appl. Phys. **107**, 09E120 (2010).

[24] A. P. Wilkinson, A. K. Cheetham, W. Kunnmann and A. Kvick, European Journal of Solid State Inorganic Chemistry **28**, 453 (1991).

[25] J. P. Perdew, K. Burke, and M. Ernzerhof, Phys. Rev. Lett. **77**, 3865 (1996).

[26] C. J. Ballhausen, Introduction to Ligand Field Theory, McGraw-Hill, New York, (1962).

[27] T. N. Nguyen, D. M. Giaquinta and H.-C. zur Loye, Chem. Mater. **6(10)**, 1642-1646 (1994).

[28] C. Stephen Helberg, W. E. Pickett, L. L. Boyer, Harold T. Stokes and Michael J. Mehl, J. Phys. Soc. Jpn. **68(11)**, 3489-3492 (1999).

[29] V. I. Anisimov, I. V. Solovyev, and M. A. Korotin, Phys. Rev. B **48**, 16929 (1999).

[30] K. I. Kugel and D. I. Khomskii, Sov. Phys. Ups. **25** 231 (1982).

[31] The values of the spin moments, particularly for Ir differ between Table. 5.3 and the present one, due to choice different sphere radii between LMTO basis and LAPW basis. A large part of the moment was found to be residing in the interstitial for LAPW calculation.

[32] C. Jia, S. Onoda, N. Nagaosa and J. Han, Phys. Rev. B **76** 144424 (2007).

Chapter 6

Tuning of magnetic ground state of spin $\frac{1}{2}$ square lattice compound $Zn_2VO(PO_4)_2$ through chemical substitution*

6.1 Background and Motivation of the present study

In the present chapter, we focus on the effect of external perturbation such as doping, on a quantum spin system (QSS). An interesting aspect of the study of QSS is exploration of emergent phenomena by perturbing the system via external tunable parameters. Apart from temperature, the other possible external tuning parameters include magnetic field, [1, 2, 3] hydrostatic and uniaxial pressure, [4, 5, 6, 7] or the chemical perturbation, which is achieved by substitution bya magnetic or non-magnetic ions [8, 9, 10, 11, 12, 13]. For example, $(C_4H_{12}N_2)Cu_2Cl_6$ [2] (a S=$\frac{1}{2}$ antiferromagnet) show finite T crossover to a quasi 2D phase with 3D Bose-Einstein condensate state at lower T and high field value. IPA-$CuCl_3$ show magnetic field induced change in the spin ordering from spin liquid state to spin solid state [3]. $TlCuCl_3$ exhibit pressure induced quantum phase transition between dimerized quantum disordered phase to long range magnetic ordered phase [5] whereas $(CH_3)_2CHNH_3CuCl_3$ show pressure induced quantum phase transition at critical pressure P_c $\sim$4 GPa [7]. Among the doping induced magnetic phase transition, most common example is $CuGeO_3$. This compound shows a variety

*This chapter is based on *Phys. Rev. B* **87**, *054431 (2013)*

of magnetic phase transition for different doping element, such as Si, Zn etc.

In the present study we focused on QSS compound $Zn_2VO(PO_4)_2$. Based on magnetic susceptibility and neutron diffraction experiments [14, 15] it has been concluded that this system behaves as a spin $\frac{1}{2}$ Heisenberg antiferromagnetic (HAF) square lattice system, exhibiting long ranged magnetic ordering [14, 15]. The stability of this long ranged ordered ground state in such type of system has been in focus of attention, particularly, depletion of spins in destabilization of long range order have been studied. For example, spin ladder compounds were obtained by breaking the planes of copper oxide materials [16]. Depletion of $\frac{1}{4}$ spins in a triangular antiferromagnetic Heisenberg lattice leads to formation of kagome lattice [17]. By depletion, bonds between spin are weakened, thereby enhancing the importance of quantum fluctuation which may destroy the long range ordering opening up a finite spin gap. This has been observed in case of CaV_4O_9 compound,[18] which has been shown as $\frac{1}{5}$ depleted 2D S=$\frac{1}{2}$ Heisenberg AF. Along the same line of thought, we explored the chemical route of tuning the ground state of $Zn_2VO(PO_4)_2$, by substitution of one magnetic V ion by nonmagnetic Ti ion out of four V ions. This would lead to $\frac{1}{4}$ spin depleted situation. The reason behind of choosing $\frac{1}{4}$ substitution is that, it gives the simplest possible substitution with one missing spin in each plaquette of four nearest neighbor V spins. We are able to predict a destabilization of long range ordered ground state of $Zn_2VO(PO_4)_2$ upon Ti substitution, showing a spin gap behavior.

6.2 Results and Discussions

6.2.1 Crystal Structure

$Zn_2VO(PO_4)_2$ crystallizes in a tetragonal crystal structure [20] of space group *I4cm* with lattice parameters, a=8.93 Å, c=9.04 Å, and with two formula units in the unit cell. The structure consists of three basic building blocks, VO_5 square pyramid, ZnO_5 square pyramid and PO_4 tetrahedra as shown in Figs. (6.1)(a), (b) and (c) respectively. Within the *ab* layer the nearest neighbor (NN) VO_5 pyramids are connected via corner sharing PO_4 tetrahedral units while the next NN VO_5 are connected by two ZnO_5 pyramids which edge share with each other as shown in Fig. (6.1)(d). VO_5 and PO_4 units are pointing in the same direction while ZnO_5 units point in the opposite direction. Different layers are stacked above each other along the crystallographic c direction and they are connected via corner shared ZnO_5

Table 6.1 Various atomic positions of the pristine $Zn_2VO(PO_4)_2$ and Ti-substituted $Zn_8TiV_3O_4(PO_4)_8$ compounds.

Atom	Pristine compound			Atom	Ti-doped		
	x	y	z		x	y	z
Zn	0.618	0.118	0.264	Zn1	0.247	0.235	-.129
V	0.000	0.000	0.101	Zn2	0.131	0.237	0.249
P	0.307	0.193	0.120	Zn3	0.250	-.265	0.133
O1	0.827	0.135	0.155	Zn4	0.367	0.233	0.252
O2	0.652	0.152	0.469	V	0.000	-.095	0.000
O3	0.000	0.000	0.427	V1	0.000	0.384	0.000
O4	0.396	0.104	0.237	V2	0.500	-.141	0.000
				Ti	0.500	0.418	0.000
				P1	0.249	-.121	-.055
				P2	0.057	-.119	0.250
				P3	0.249	0.382	0.059
				P4	0.442	-.121	0.249
				O1	0.000	0.083	0.000
				O2	0.152	-.150	0.016
				O3	-.016	-.147	0.154
				O4	0.257	0.033	-.094
				O5	0.099	0.033	0.255
				O6	0.156	0.341	-.017
				O7	0.017	0.342	0.156
				O8	0.000	-.439	0.000
				O9	0.247	-.232	-.147
				O10	0.146	-.234	0.249
				O11	0.253	0.263	0.146
				O12	0.340	-.167	0.019
				O13	0.346	0.361	-.014
				O14	0.239	0.031	-.394
				O15	0.399	0.030	0.237

		O16	0.353	-.236	0.255
		O17	0.500	0.035	0.000
		O18	0.482	-.167	-.159
		O19	0.500	-.393	0.000
		O20	0.486	-.141	-.348

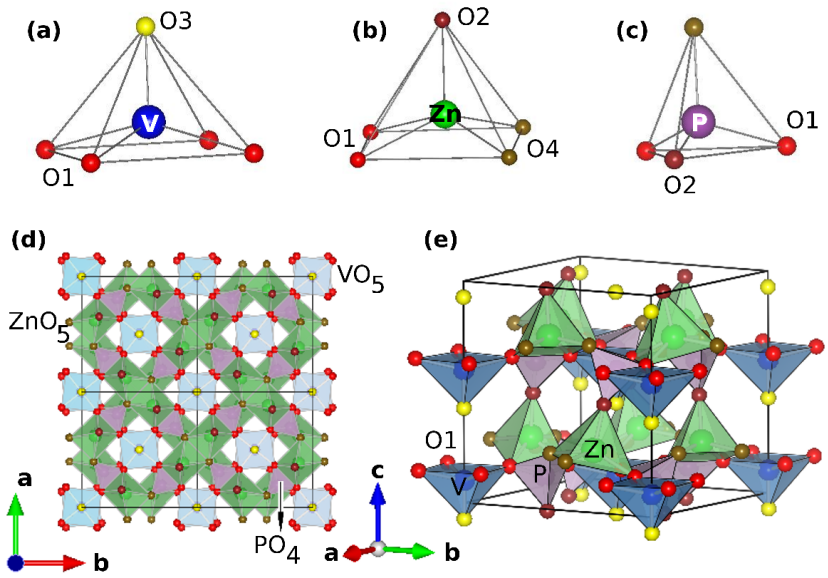

Figure 6.1 (a)-(c)VO_5, ZnO_5 and PO_4 structural units. The larger ball represents either V or Zn or P while the smaller balls represent O. Various in-equivalent O atoms have been marked. (d) The projection of the structure in *ab* plane, showing the square planar arrangement of VO_5 pyramids. (e) The three dimensional connected structure.

and PO_4 units, giving rise to the 3D connected network as shown in Fig. (6.1)(e). Substituting one V atom by Ti out of four V atoms in a $1 \times 1 \times 2$ supercell, as shown in Fig. (6.2), lowers the tetragonal *I4cm* symmetry to monoclinic A2 symmetry [21] with a = 12.851 Å, b = 9.180 Å, c = 12.852 Å and β = 90.02^o, and giving rise to the three nonequivalent classes of V atoms, V, V1 and V2 (see Fig. (6.2)). V1 is neighbor to Ti within the plane, V2 is neighbor to Ti both in plane and along out of plane direction while V does not have any Ti as neighbor. For V1, this gave rise to 2 V neighbors along one of the in plane direction and 2 V neighbor in the out of plane direction. For V, there are two V2 and two V1 neighbors along two in plane directions and 2 V1 neighbor in the out of plane direction. For V2 atom,

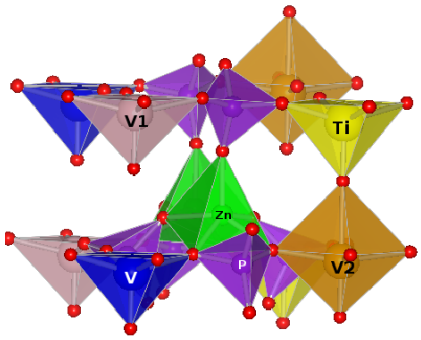

Figure 6.2 The crystal structure of $\frac{1}{4}$ Ti substituted $Zn_2VO(PO_4)_2$.

on the other hand, there is only 2 V neighbor along one of the in plane direction with no out of plane vanadium neighbor.

The structural degeneracy of Zn, P and various O atoms are also additionally lifted in the Ti substituted structure. The crystal structure data of Ti-substituted $Zn_2VO(PO_4)_2$ in comparison to pristine $Zn_2VO(PO_4)_2$, obtained through complete structural relaxation, is shown in Table. 6.1. The important structural parameters like V-O bond lengths and O-V-O bond angles are shown in Table. 6.2. We find that in the Ti substituted system the VO_5 pyramidal unit are more distorted in the sense that while the VO_5 pyramids in pristine compound are regular square pyramids with all V-O bond lengths in the basal plane being equal and with short V-O apical bond, for Ti substituted compound the V-O bond lengths even in basal plane become unequal.

6.2.2 Electronic Structure of Pristine Compound

The GGA non-spin polarized density of states (DOS) of the pristine compound, as shown in Fig. (6.3), are made up of *d*-*p* hybridized states starting from about 6 eV below the Fermi level (E_F) to about 4 eV above E_F. The states below -4 eV or so are dominated by O-*p* states, while the states close to Fermi level or above E_F are dominated by the different V-*d* states. Due to the square pyramidal crystal environment around V atom, the V-*d* states splits into low lying V-d_{xy} states, followed by other *d* states which are separated by a large energy gap of $\approx$ 1 eV. The energy level splitting of V-*d* states are obtained through NMTO downfolding calculation by keeping V-*d* states active and downfolding the rest (*i.e* Zn, P and O states) and considering the onsite block of the real space Hamiltonian in the

Table 6.2 The TM-O bond lengths and O-TM-O bond angles in pristine ($Zn_2VO(PO_4)_2$) and Ti-substituted ($Zn_8TiV_3O_4(PO_4)_8$) compounds.

Unit	Pristine compound	Ti-substituted
VO_5	V-O(basal)=2.01 Å	V-O(basal)=1.99 Å
		2.11 Å
	V-O(apical)= 1.56 Å	V-O(apical)= 1.63 Å
	O-V-O(basal)=86.7^o	O-V-O(basal)=86.1^o
		86.6^o
	O-V-O(apical)=103.9^o	O-V-O(apical)=104.3^o
		105.1^o
		V1-O(basal)= 2.02 Å
		2.02 Å
		V1-O(apical)= 1.62 Å
		O-V1-O(basal)=87.0^o
		87.4^o
		O-V1-O(apical)=102.6^o
		102.8^o
		V2-O(basal)= 2.03 Å
		2.03 Å
		V2-O(apical)= 1.62 Å
		O-V2-O(basal)=88.6^o
		88.9^o
		O-V2-O(apical)=98.2^o
		98.4^o
TiO_5		Ti-O(basal)= 2.03 Å
		2.01 Å
		Ti-O(apical)= 1.71 Å
		O-Ti-O(basal)=85.6^o
		85.8^o
		O-Ti-O(apical)=105.5^o
		106.2^o

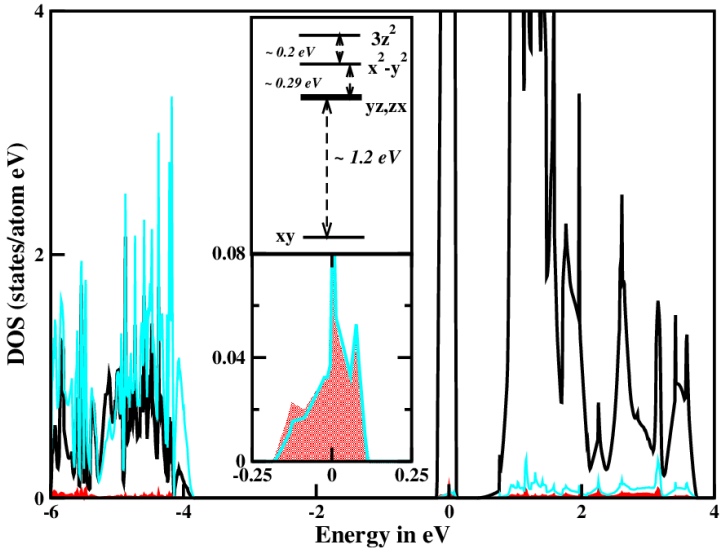

Figure 6.3 Non spin-polarized density of states of $Zn_2VO(PO_4)_2$ as obtained in GGA calculation. The zero of the energy is set at GGA Fermi energy. The black-solid line, cyan solid line and the shaded area represent the density of states projected on to V-*d*, O-*p* and P-*p* respectively. The upper inset shows the energy level positions of V-*d* level as obtained in NMTO downfolding calculation. The lower inset shows the zoomed plot showing the contribution of O-*p* and P-*p* states to the V-d_{xy} derived states that cross the Fermi energy.

downfolded V-*d* basis is shown in the upper inset of Fig. (6.3). The nominal valence states of V atom in $Zn_2VO(PO_4)_2$ is 4+ with d^1 occupancy. Therefore half filled V-d_{xy} states cross the Fermi level as shown in the band structure plot of Fig. (6.4)(a), which hybridizes with O-*p* and P-*p* states as shown in the lower inset in Fig. (6.3). Inclusion of correlation effect beyond GGA in the half filled V-d_{xy} gives rise to insulating solution through formation of lower and upper Hubbard bands, as has been checked through GGA+U calculations [19].

The low energy effective Hamiltonian of the system thus can be constructed in terms of V-d_{xy} only model. In order to construct the low energy Hamiltonian of the system in an ab-initio way, we carried out NMTO downfolding calculation, in which only V-d_{xy} degrees of freedom were kept active and rest all including other V-*d* states were downfolded. The downfolded V-d_{xy} band in comparison to full band is shown in Fig. (6.4)(b). This process led to construction of effective V-d_{xy} Wannier like function which has the central part shaped according to V-d_{xy} symmetry and tails shaped according to integrated out degrees of freedom, as shown in Fig. (6.4)(c). The real space Hamiltonian defined in the basis

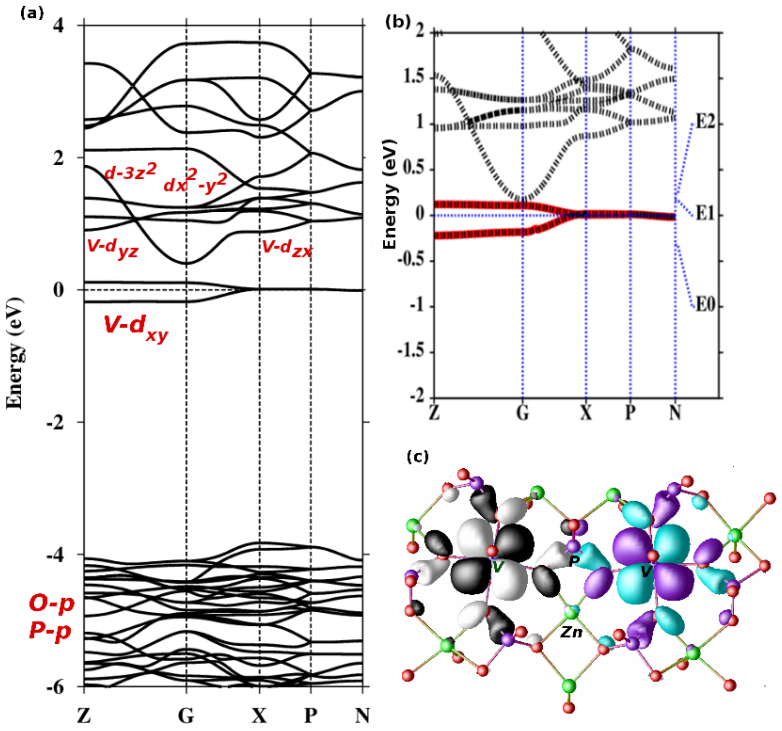

Figure 6.4 (a) The band structure of $Zn_2VO(PO_4)_2$ plotted along the high symmetry points of the tetragonal Brillouin zone. The dominant orbital characters of the bands have been marked. (b) The downfolded V-d_{xy} band (fat solid line) in comparison to full band structure (dashed line). The energy points indicate the energies about which the expansion has been made in NMTO downfolding calculation. (c) The overlap of V-d_{xy} Wannier functions placed at two NN, V sites in *ab* plane. Shown are the constant value surfaces with positive and negative lobes colored differently.

of effective V-d_{xy} Wannier function provides estimates of various V-V effective hopping interactions which are listed in Table. 6.3. The various dominant hoppings are shown in Fig. (6.5). The strongest hopping interaction is the in plane nearest neighbor interaction (t_1), between two V atoms at the centre and corner of the square in *ab* plane. Though the out of plane V-V distance is much shorter than that of in plane V-V distances, the corresponding hopping interaction (t_c) is found to be about factor of 8 weaker compared to that of the strongest in plane hopping interaction (t_1). The V-V hoping along the edge of the square (t_2) as shown in Fig. (6.5), is also weak, about a factor of 7 weaker compared to that of the strongest one (t_1). Therefore our study confirm that $Zn_2VO(PO_4)_2$ should be described as a weakly coupled 2D square lattice system rather than a chain system which was proposed [20] based solely on the structural consideration. The super-exchange path corresponding to the strongest inter-

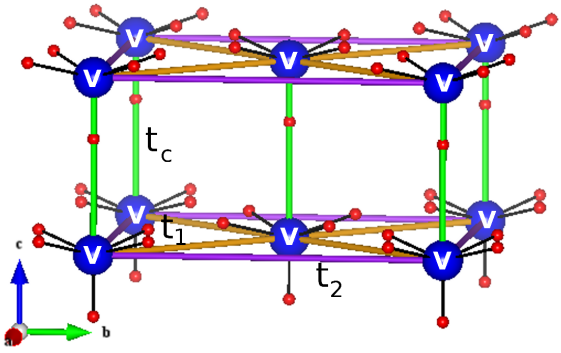

Figure 6.5 The V only sublattice of $Zn_2VO(PO_4)_2$. Shown are the dominant hoppings, t_1, t_2 and t_c

action is shown in Fig. (6.4)(c) by the superposition of two effective V-d_{xy} Wannier functions at two NN in plane V sites. From the overlap of effective wannier function it is clear that O-p like tails of Wannier function bend toward the intervening P sites indicating the importance of hybridization effect from P atom. This is justified by finite non-zero contribution of P-p projected DOS in the energy range of V-d_{xy} dominated DOS as is shown in the lower inset of Fig. (6.3). The strongest V-V interaction (t_1) is therefore mediated via V-O-P-O-V super-super-exchange path similar to that found in $(VO)_2P_2O_7$ [22].

Using the knowledge of effective hopping integrals we can estimate the antiferromagnetic super-exchange J through the second order perturbation relation $J = 4t^2/U$, U being the effective on-site Coulomb repulsion. But it requires proper estimation of U as well as energy separation of different energy levels involving in the complicated super-super exchange path. To obtain, accurate estimate of the magnetic interactions as well as to take into account the ferromagnetic contribution of the exchange interaction, we carried out total energy calculations within GGA+U with choice of U=4 eV and J_H=1 eV for different orientations of V spins, and mapped the ab-initio total energy of various spin configurations of V atoms onto the energetics of the corresponding Heisenberg model. Such an approach is found to be highly successful in description of spin models and providing estimates of magnetic interactions in a number of cases as also shown in the previous cases [23]. From this total energy calculation we found that the strongest in plane NN interaction (J_1)is antiferromagnetic of magnitude 10 K, and the

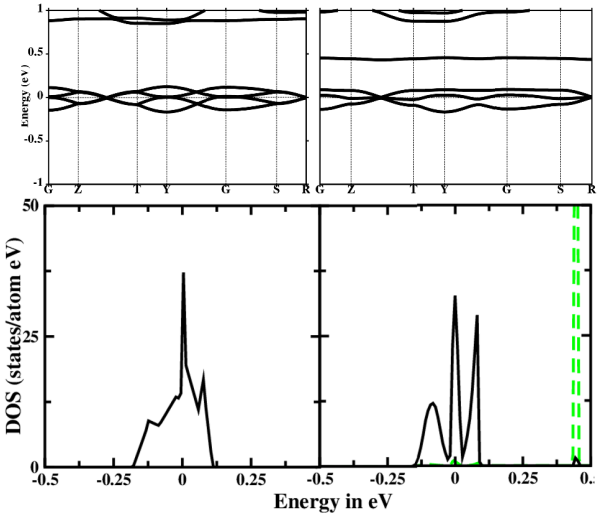

Figure 6.6 Upper panels: Comparison of the band structure of $Zn_2VO(PO_4)_2$ (left panel) and $Zn_8TiV_3O_4(PO_4)_8$ (right panel) plotted along the high symmetry points of the supercell. Lower panels: The density of states of $Zn_2VO(PO_4)_2$ (left panel) and $Zn_8TiV_3O_4(PO_4)_8$ (right panel). The V-*d* and Ti-*d* (applicable for the right panel) projected states are shown as solid and dashed lines.

ratio of other J's *i.e* $\frac{J_2}{J_1}$=0.02 and $\frac{J_c}{J_1}$=-0.03, in good agreement with the values obtained by fitting the susceptibility data [14] and Neutron scattering data [15].

6.2.3 Electronic Structure of Ti substituted Compound

Substitution of Ti, in one V site out of 4 V sites in a 1 × 1 × 2 supercell, changes the band structure significantly. In the upper panels of Fig. (6.6), we show the GGA band structure of pristine and $\frac{1}{4}$-Ti substituted compound, both plotted for 1 × 1 × 2 supercell. The 1 × 1 × 2 supercell of $Zn_2VO(PO_4)_2$ consists of 4 V sites, giving rise to the 4 V-d_{xy} bands, which cross the Fermi energy as shown in right panel of Fig. (6.6). Upon Ti substitution, Ti-d_{xy} band which is empty, splits off from the manifold of V-d_{xy} band with a gap of about 0.5 eV and remains dispersionless due to non-interacting nature of empty Ti states. The three V atom which have become in-equivalent due to Ti substitution, give rise to three V-d_{xy} bands crossing Fermi level, in accordance to their half filled nature. The degeneracy of bands in the case of Ti- substituted case gets lifted at several k-points compared to the band structure of the pristine compound due to the breaking of structural degeneracy between different V atoms. Comparing

Table 6.3 Dominant hopping interactions for the pristine and Ti-substituted compounds. Hopping interactions having magnitude less than 1 meV have been neglected.

Pristine compound			Ti-substituted compound		
Dist.	No. of neighbors	Hopping	Dist.	No. of neighbors	Hopping
4.51 Å	2	5.20 meV (t_c)	4.64 Å	1	6.00 meV ($t_c^{'}$)
6.30 Å	4	39.7 meV (t_1)	6.31 Å	2	39.7 meV ($t_1^{'}$)
8.92 Å	4	6.80 meV (t_2)	6.32 Å	2	9.50 meV ($t_1^{"}$)

the DOS of the two compounds as shown in the lower panels of Fig. (6.6), we find that widths of V-d_{xy} dominated states are nearly same in two cases, indicating strengths of the dominated V-V interaction to be nearly same between the pristine and Ti-substituted case. Carrying out NMTO-downfolding calculation to define the effective V-d_{xy} low energy Hamiltonian, as done for the pristine compound; and constructing the real space Hamiltonian, we find the dominant hopping interactions which are listed in Table. 6.3. We found that after the Ti substitution the spin model changes significantly, leading to anisotropic grouping of interactions. Comparing with the interactions of pristine compound, we find that four NN in plane interactions (t_1) which were strongest for pristine compound, groups into two strong (connecting V and V1) t_1' and two weak (connecting V and V2) t_1'' interactions.

Similarly, the out of plane interaction is significant only for the interaction from V to V1, and not other way, which makes a pair of out of plane connected V atoms for $Zn_8TiV_3O_4(PO_4)_8$ rather than a chain V atoms connected in out of plane direction as in case of $Zn_2VO(PO_4)_2$. The total energy calculation within GGA+U scheme to estimate the strengths of magnetic interactions corresponding to t_1', t_1'' and t_c' gave rise to values J_1'=8 K, $\frac{J_1''}{J_1'}$=0.03 and $\frac{J_c'}{J_1'}$=-0.04. The spin model for pristine and $\frac{1}{4}$-Ti substituted compounds, therefore can be described as weakly coupled 2-D, AFM square lattice and weakly coupled 1-D AFM chain respectively as shown in Fig. (6.7).

6.2.4 Calculation of Magnetic Properties

In the next step we computed the magnetic susceptibility as well as magnetization properties by considering the spin $\frac{1}{2}$- Heisenberg model on $N_1 \times N_2 \times N_3$ lattices. The description of spin models for

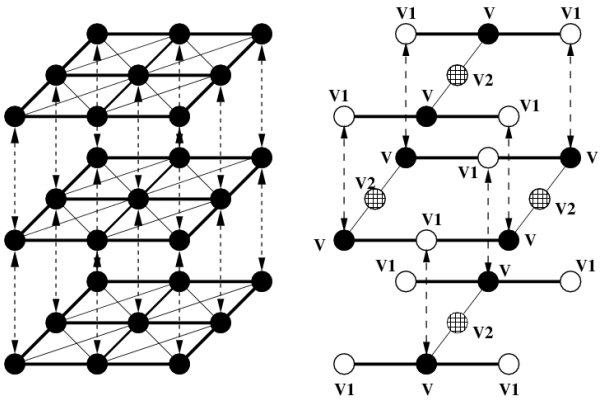

Figure 6.7 The spin models corresponding to $Zn_2VO(PO_4)_2$ (left panel) and $Zn_8TiV_3O_4(PO_4)_8$ (right panel) compounds. The thick solid, thin solid and dashed lines represent strongest J_1 (J_1') and weak J_2 (J_1'') and J_c (J_c') interactions for $Zn_2VO(PO_4)_2$ ($Zn_8TiV_3O_4(PO_4)_8$) compound. The spins corresponding to inequivalent V ions in case of the substituted $Zn_8TiV_3O_4(PO_4)_8$ compound has been marked.

the pristine and Ti-substituted compounds as obtained from ab-initio calculations, turn out to be weakly coupled 2D model and weakly coupled 1D chains respectively. The considered spin models, therefore are given as follows;

$$\begin{aligned} H^{pristine} &= J_1 \sum_{i=1}^{N1}\sum_{j=1}^{N2}\sum_{k=1}^{N3} S_{i,j,k}.(S_{i+1,j,k}+S_{i,j+1,k}) + \\ & J_2 \sum_{i=1}^{N1}\sum_{j=1}^{N2}\sum_{k=1}^{N3} S_{i,j,k}.(S_{i+1,j+1,k}+S_{i+1,j-1,k}) \\ & + J_c \sum_{i=1}^{N1}\sum_{j=1}^{N2}\sum_{k=1}^{N3} S_{i,j,k}.S_{i,j,k+1} \end{aligned}$$

$$\begin{aligned} H^{Ti-doped} &= J_1' \sum_{i=1}^{N1}\sum_{j=1}^{N2/2}\sum_{k=1}^{N3} S_{i,2j,k}.S_{i+1,2j,k} + \\ & J_1\prime \sum_{i=1}^{N1/2}\sum_{j=1}^{N2/2}\sum_{k=1}^{N3} S_{i',2j,k}.S_{i',2j\pm1,k} + \\ & J_c' \sum_{i=1}^{N1/2}\sum_{j=1}^{N2/2}\sum_{k=1}^{N3} S_{i',2j,k}.S_{i',2j,k+1} \\ & (i' = 2i - mod(k,2)) \end{aligned}$$

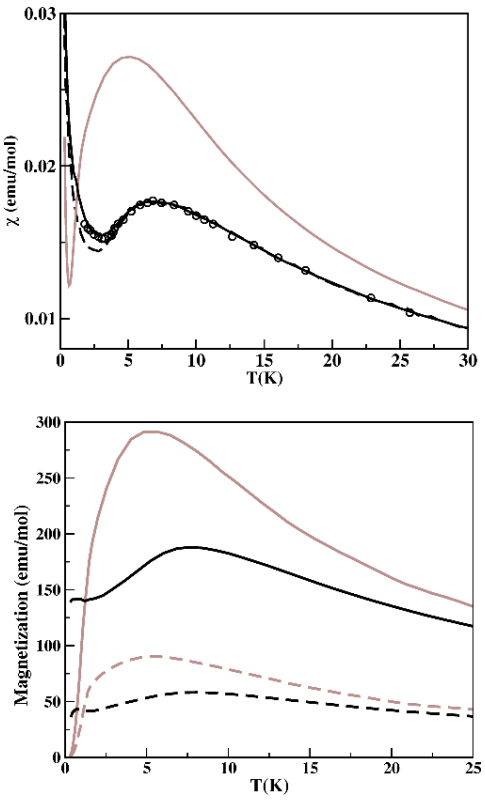

Figure 6.8 Upper panel: Calculated magnetic susceptibility plotted as a function of temperature for the pristine (black lines) and Ti-substituted (grey lines) compounds. The magnetic susceptibility for the pristine compound has been computed in absence (dashed line) and in presence of applied magnetic field of 10000 Oe (solid line). The latter has been compared with the experimentally measured data, [14] shown as open circles. Lower panel: Magnetization plotted as a function of temperature for the pristine (black lines) and Ti-substituted (grey lines) compounds for two different values of the magnetic field, H = 5000 Oe (solid line) and H= 1560 Oe (dashed line).

where J's are the exchange integrals of the spin models as shown in Fig. (6.7) as calculated from the ab-initio method (*c.f* Fig. (6.7)). The above models have been solved by the Quantum Monte Carlo (QMC) method (stochastic series expansion [24]) on a 14 $\times$ 14 $\times$ 14 lattice. The QMC computed susceptibility given by $\chi^{th} = \langle (S^z - \langle S^z \rangle)^2 \rangle$ is compared with the experimentally measured susceptibility [14] of the pristine compound in presence of magnetic field of 10000 Oe via $\chi = 0.375\ S(S+1)(\frac{g^2}{J_1})\chi^{th}$, at intermediate and high temperature. To capture the low temperature behavior we also included Curie contribution from paramagnetic impurities as $\chi^{CW} = C_{imp}/T$. The best fit to experimentally measured

susceptibility was obtained for g = 2.26, J_1 = 8 K (the ratios $\frac{J_2}{J_1}$ and $\frac{J_c}{J_1}$ was fixed at DFT estimates, 0.02 and -0.03 respectively) and C_{imp}=0.006. In the upper panel of Fig. (6.8), we show the computed susceptibility for the pristine compound in presence and absence of magnetic field, comparing with the experimental data obtained in presence of magnetic field 10000 Oe. The computed susceptibility for the Ti substituted model is also presented, which shows a drastic changes in behavior compared to the pristine compound. The susceptibility following the presence of a broad maxima, shows an exponential drop at lower temperature signaling the characteristic opening of spin gap. The change in magnetic behavior of the pristine to Ti substituted compound is also evident in the computed magnetization as a function of temperature for magnetic fields strengths, 5000 Oe and 1560 Oe as shown in bottom panel of Fig. (6.8). This undoubtedly, shows the control of magnetic ground state of a typical 2-D AFM square lattice through chemical substitution by changing the ground state from a long ranged ordered one for the pristine compound to a spin gapped one for the substituted compound. The computed thermodynamic quantities are expected to provide the database to check the validity of our predictions through future experimental measurements.

6.3 Conclusion

The analysis of electronic structure of $Zn_2VO(PO_4)_2$ compound through first principle DFT calculations and subsequent calculation of thermodynamics properties by QMC method, confirm the description of $Zn_2VO(PO_4)_2$ as weakly coupled 2-D AFM S-$\frac{1}{2}$ Heisenberg system as predicted earlier by experimental measurement. Motivated by literature [18] on the effect of spin dilution in destabilizing the long range order in 2-D AFM lattice, we designed on computer Ti substituted $Zn_8TiV_3O_4(PO_4)_8$ compound. Our theoretical study predicts $Zn_8TiV_3O_4(PO_4)_8$ compound to be a spin gapped system, given by a spin model of a weakly interacting 1-D spin chains. Our predictions may be verified in terms of future experimental measurements.

Bibliography

[1] T. Giamarchi, Ch. Rüegg, and O. Tchernyshyov, Nature Physics **4**, 198 (2008);

[2] M. B. Stone, C. Broholm, D. H. Reich, O. Tchernyshyov, P. Vorderwisch and N. Harrison, Phys. Rev. Lett. **96**, 257203 (2006);

[3] A. Zheludev, V. O. Garlea, T. Masuda, H. Manaka, L.-P. Regnault, E. Ressouche, B. Grenier, J.-H. Chung, Y. Qiu, K. Habicht, K. Kiefer, and M. Boehm, Phys. Rev. B **76**, 054450 (2007).

[4] B. Leuenberger, H. U. Güdel and J. K. Kjems, J. Mag. Mag. Matt. **53**, 175 (1985);

[5] Ch. Rüegg, B. Normand, M. Matsumoto, A. Furrer, D.F. McMorrow, K. W. Krämer, H.-U. Güdel, S. Gvasaliya, H. Mutka, and M. Boehm, Phys. Rev. Lett. **100**, 205701 (2008);

[6] H. Tanaka, K. Goto, M. Fujisawa, T. Ono, Y. Uwatoko, Physica B: Condensed Matter **329-333B**, 697 (2003).

[7] T. Hong, V. O. Garlea, A. Zheludev, J. A. Fernandez-Baca, H. Manaka, S. Chang, J. B. Leao, and S. J. Poulton, Phys. Rev. B **78**, 224409 (2008).

[8] T. Masuda, A. Fujioka, Y. Uchiyama, I. Tsukada and K. Uchinokura, Phys. Rev. Lett. **80**, 4566 (1998).

[9] L. P. Regnault, J. P. Renard, G. Dhalenne, and A. Revcolevschi, Europhys. Lett. **32**, 579 (1995);

[10] Y. Sasago, N. Koide, K. Uchinokura, M. C. Martin, M. Hase, K. Hirota, and G. Shirane, Phys. Rev. B **54**, R6835 (1996).

[11] M. C. Martin, M. Hase, K. Hirota, G. Shirane, Y. Sasago, N. Koide, and K. Uchinokura, Phys. Rev. B **56**, 3173 (1997).

[12] T. Masuda, I. Tsukada, K. Uchinokura, Y. J. Wang, V. Kiryukhin, and R. J. Birgeneau, Phys. Rev. B **61**, 4103 (2000).

[13] T. Waki, Y. Itoh, C. Michioka, K. Yoshimura, M. Kato, Phys. Rev. B **73**, 064419 (2006).

[14] N. S. Kini, E. E. Kaul and C. Geibel, J. Phys.: Condens. Matter **18**, 1303-1311 (2006)

[15] S. M. Yusuf, A. K. Bera, N. S. Kini, I. Mirebeau, and S. Petit, Phys. Rev. B **82**, 094412 (2010).

[16] E. Dagotto and T. M. Rice, Science **271**, 618 (1996).

[17] C. Zeng and V. Elser, Phys. Rev. B **42**, 8436 (1990).

[18] S. Taniguchi, Y. Nishikawa, Y. Yasui, Y. Kobayashi, M. Sato, T. Nishikawa, M. Kontani and K J. Sano, Phys. Soc. Japan **64**, 2758 (1995).

[19] V. I. Anisimov, I. V. Solovyev and M. A. Korotin, Phys. Rev. B **48**, 16929 (1993).

[20] K H Lii and H J Tsai, J. Solid State Chem. **90**, 291 (1991).

[21] The defined cell is the conventional unit cell and not the standard unit cell, which are rotated with respect to each other.

[22] A.W. Garrett, S.E. Nagler, D.A. Tennant, B.C. Sales, T. Barnes, Phys. Rev. Lett. **79**, 745 (1997).

[23] R. Valenti, T. Saha-Dasgupta, J. V. Alvarez, K. Pozgajcic, and C. Gros, Phys. Rev. Lett. **86**, 5381 (2001); T. Saha-Dasgupta, Roser Valenti, F. Capraro, and C. Gros, Phys. Rev. Lett. **95**, 107201(2005); H. Das, T. Saha-Dasgupta, C. Gros, and Roser Valenti, Phys. Rev. B **77**, 224437 (2008); M. Pregelj, H. O. Jeschke, H. Feldner, R. Valenti, A. Honecker, T. Saha-Dasgupta, H. Das, S. Yoshii, T. Morioka, H. Nojiri, H. Berger, A. Zorko, O. Zaharko, and D. Arcon, Phys. Rev. B **86**, 054402 (2012); M. Reehuis, T. Saha-Dasgupta, D. Orosel, J. Nuss, B. Rahaman, B. Keimer, O. K. Andersen, and M. Jansen, Phys. Rev. B **85**, 115118 (2012).

[24] A. W. Sandvik, Phys. Rev. B **59**, R14157 (1999); A. Dorneich and M. Troyer, Phys. Rev. E **64**, 066701 (2001); K. Louis and C. Gros, Phys. Rev. B **70**, 100410(R) (2004).

Chapter 7

First principles Study of Organic-inorganic Hybrid Framework Compound, $Mn(C_4H_4O_4)$*

7.1 Introduction and motivation of the present work

Crystalline hybrid materials containing both organic and inorganic components have become a fascinating field of research from both application as well as fundamental physics perspective. In this direction a number of new type of metalorganic framework materials have been synthesized to explore more applicability of such systems. 'Succinate's are such organic systems which are hugely used in the food processing industry, pharmaceuticals industries [1]. In addition to practical applications, succinate systems show wide range of magnetic behavior such as Co- succinate $[Co_5(OH)_2(C_4H_4O_4)_4]$ and $[Co_4(OH)_2(H_2O)_2(C_4H_4O_4)_3.2H_2O$, exhibit ferrimagnetic interactions [2], which are interesting from the academic view point.

In the present case we focus on theoretical investigation of one such compound, namely Mn succinate, $[Mn(C_4H_4O_4)]$, which consists of inorganic component Mn and organic component of succinate bridges within the unit cell of the crystal. This system has been synthesized [12] and studied by single crystal X-ray diffraction as well as by neutron diffraction experiments [13]. This particular compound

*This chapter is based on *Phys. Rev. B* **84**, *134415 (2011)*

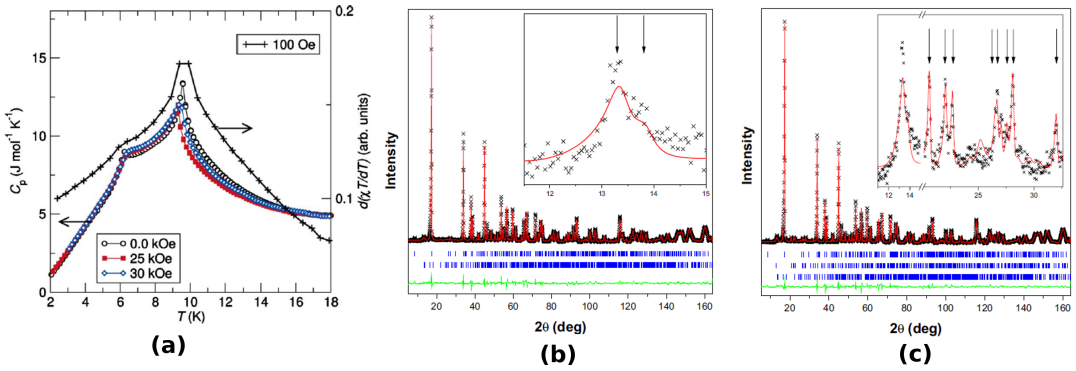

Figure 7.1 (a) Heat-capacity measurements for $MnC_4H_4O_4$ and the Fisher heat capacity determined using magnetic-susceptibility data indicating the two antiferromagnetic phase transitions at approximately 6 K and 10 K. Taken form Ref. [12]. (b) and (c) The Rietveld fit to the 8 K and 4.2 K neutron pattern respectively. The inset plot indicates the observed reflections caused by the magnetic ordering of the edge-sharing layer and corner sharing layer respectively. Figures are reproduced form Ref. [13].

is so far only known Mn succinate to exhibit nicely ordered magnetic behavior since the other known Mn succinate, $Mn_5(OH)_2(C_4H_4O_4)$ exhibits weak antiferromagnetism due to high degree of frustration. The specific heat measurements [13] carried out on $Mn(C_4H_4O_4)$ clearly exhibits magnetic ordering at two different temperatures near about $\approx$ 6 K and 10 K as shown in Fig. 7.1). The neutron diffraction study which recorded diffraction pattern in different temperatures identifies a two step ordering of Mn spins in this compound (Fig. (7.1)). The structure consists of alternating layers of edge and corner sharing MnO_6 octahedra, connected by succinate bridge. The edge sharing MnO_6 octahedra order first at 10 K, into a collinear sinusoidal spin structure with a propagation vector $\vec{k}$=(0,-0.5225,0), followed by a second antiferromagnetic ordering of the corner sharing MnO_6 octahedra at 6 K with a propagation vector $\vec{k}$=(-1,0,1). Most important thing is that the ordering in the edge sharing octahedral layer and that in the corner sharing octahedral layer are found to be independent of each other. This phenomena of two independent magnetic ordering of the same chemical species (Mn) within the same material is rare among the classical inorganic compounds. Therefore, we wish to investigate the microscopic origin of the experimentally observed two step magnetic ordering using DFT [14] based first principles electronic structure calculations. This will also act as a test the applicability of DFT technique in the case of hybrid materials with extended inorganic connectivity.

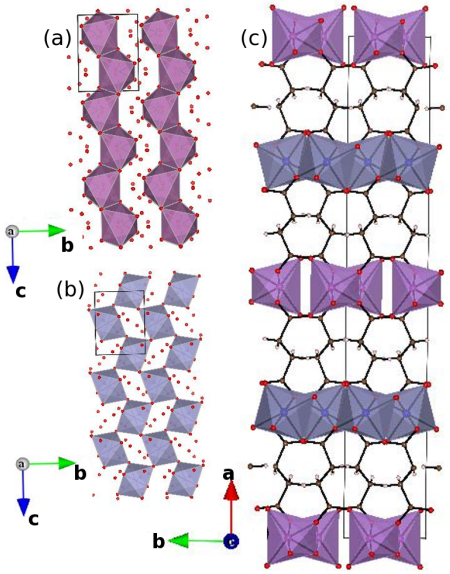

Figure 7.2 (a) The layer of edge sharing $Mn1O_6$ octahedra forming the chain like structure. (b) The layer of corner sharing $Mn2O_6$ octahedra forming connected 2-D geometry. (c) The alternate stacking of the edge shared and the corner shared MnO_6 layers connected through succinate ligands. The magenta colored octahedra belongs to the edge shared layer and the grey colored octahedra belongs to the corner shared layer.

7.2 Results and Discussions

7.2.1 Crystal Structure

$Mn(C_4H_4O_4)$ crystallizes in a monoclinic crystal structure of space group *C2/c* with Z=4 in a unit cell. The structure contains two crystallographically inequivalent Mn ions, Mn1 and Mn2, four crystallographically inequivalent oxygens and carbons, O1 to O4 and C1 to C4 respectively and four inequivalent hydrogen atoms H2A, H2B, H3A and H3B. Both Mn1 and Mn2 cations are surrounded by six oxygens in a octahedral environment, with O1 and O2 participating in formation of $Mn1O_6$ octahedra and O3 and O4 participating in formation of $Mn2O_6$ octahedra. $Mn1O_6$ octahedra are connected to another $Mn1O_6$ octahedra by sharing edges by O2 type oxygen and form a chain like structure running approximately along crystallographic *c*-axis, as shown in Fig. (7.2). Two such neighboring chains are connected to each other via O1-C1-O2 bridges as shown more clearly in Fig. (7.3). The whole connected chain system of $Mn1O_6$ octahedra form a layer in *bc* plane. Two $Mn2O_6$ octahedra are

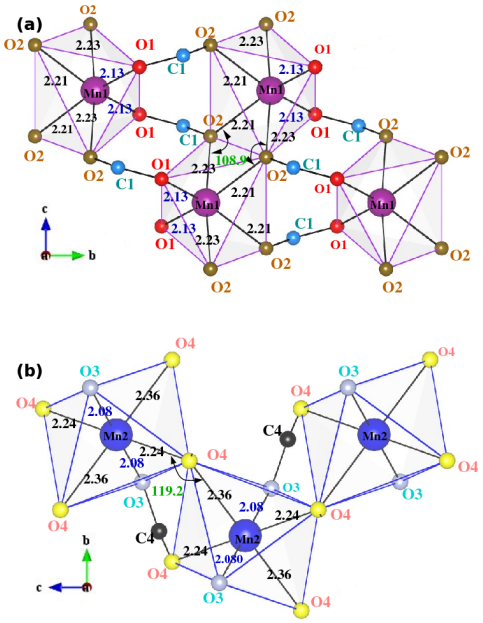

Figure 7.3 (a) Local environment of the edge shared $Mn1O_6$ octahedra, (b) Local environment of the corner shared $Mn2O_6$ octahedra. The various Mn-O bond lengths as well as the edge shared Mn-O-Mn bond angle and corner shared Mn- O-Mn bond angle have been marked.

connected by corner shared via O4 type oxygen and form a nearly 2-dimensional planar structure in *bc* plane as shown in Fig. (7.3). The edge shared $Mn1O_6$ layer and corner shared $Mn2O_6$ layers are stacked on top of each along crystallographic *a*-axis, separated by succinate ligands.

The local environment of edge sharing $Mn1O_6$ octahedral layers and corner sharing $Mn2O_6$ octahedral layers are shown in top and bottom panel of Fig. (7.3) respectively. Mn1 atom is surrounded by four O2 and two O1 atoms. The $Mn1O_6$ octahedra is slightly distorted in terms of Mn-O bond lengths differing by 0.02 Åto about 0.1 Å. Out of four O2, two are involved in the edge sharing with neighboring $Mn1O_6$ octahedra along the chain direction. Two $Mn1O_6$ octahedra belonging to two neighboring chains are connected via O1-C1-O2 path as mentioned already. Mn2 is surrounded by four O4 atoms and two O3 atoms. $Mn2O_6$ octahedra is more distorted than $Mn1O_6$ octahedra in terms of bond lengths. In $Mn2O_6$ case the bond length varies from 0.2-0.3 Å. The neighboring $Mn2O_6$ octahedra are connected through corner shared O4 atoms as well as through O3-C4-O4 bridge.

Since the position of the light elements are generally not well characterized by X-ray diffraction

technique, we have carried out the structural relaxation of the compound relaxing the internal positions of all atoms in the unit cell and keeping the lattice parameters fixed at the experimental values. Table. 7.1 shows the theoretical optimized coordinates along with the experimentally measured coordinates. The positions of light elements like O, C, H are found to change significantly in the theoretical optimization compared to the experimentally measured positions. The relaxed coordinates associated with the oxygen positions were found to change at most 5%, where as the carbon and hydrogen positions were found to change at most 7% and 38% respectively. In term of absolute value, the oxygen positions were found to move at most by 0.22 Å(O1), whereas the largest movement of carbon and hydrogen positions were found to be 0.10 Å(C3) and 0.17 Å(H3B), respectively, compared to experimentally measured positions. A comparison of selected Mn-O bond lengths and Mn-O-Mn bond angles between the experimentally measured structure and optimized structure is shown in Table. 7.2. The maximum change is found for the Mn1-O1 bond length, which is expected from the largest movement of the O1 atom during optimization. The results described in the following are carried out in the optimized crystal structure.

7.2.2 Electronic Structure

Fig. (7.4) and Fig. (7.5) show non spin polarized electronic structure of $Mn(C_4H_4O_4)$. The non spin-polarized density of states (Fig. (7.4)) consists of Mn-*d* and O-*p* and C-*p* hybridized band structure that extends from about -9 eV below the Fermi level (E_F) to about +3 eV above the E_F as shown in the top panel of Fig. (7.4). The states in range from about -9 eV to about -6 eV are mainly of C-*p* character while those in an energy range from -6 eV to -3 eV are mainly of O-*p* character. The states close to E_F are mainly dominated by Mn1-*d* and Mn2-*d* characters as shown in DOS and band structure (Fig. (7.5)). The 5-fold degeneracy of *d* levels of Mn1 and Mn2 is completely lifted due to the distorted nature of Mn1 and Mn2 octahedra. Fig. (7.5) shows orbital projected band structure which consists of Mn1 and Mn2 t_{2g} and e_g states. It clearly shows that for both Mn1 and Mn2 sites five fold degeneracy of *d* states gets completely lifted and the *d* states are grouped into three region in the energy scale. This can be seen more clearly in the energy level diagram. Fig. (7.6) shows the computed crystal field splitting at the Mn1 and Mn2 sites obtained by the NMTO downfolding calculation in which the Mn-*d* degrees of freedom were kept active and all others, *i.e* C, O and H degrees of freedom were downfolded. The

Table 7.1 The theoretically optimized atomic positions compared to the experimentally determined data. During the optimization the lattice constants are fixed at experimentally measured values, a=30.28 Å, b=4.86 Å, c=6.29 Å, β=99.50^o.

Atom	Measured Positions			Optimized Positions		
	x	y	z	x	y	z
Mn1	0.0000	0.3160	0.2500	0.0000	0.3160	0.2500
Mn2	-0.2500	-0.7500	0.0000	-0.2500	-0.7500	0.0000
O1	-0.0568	0.0628	0.1442	-0.0501	0.0660	0.1653
O2	-0.0313	0.3419	0.5464	-0.0302	0.3602	0.5464
O3	-0.1928	-0.5162	0.1008	-0.1980	-0.5148	0.0957
O4	-0.2185	-0.1213	0.2169	-0.2209	-0.1109	0.2140
C1	-0.0624	-0.1860	0.0929	-0.0598	-0.1866	0.0999
C2	-0.1082	-0.3164	0.0829	-0.1072	-0.3056	0.0876
C3	-0.1408	-0.1548	0.1948	-0.1425	-0.1544	0.1804
C4	-0.1874	-0.2726	0.1653	-0.1900	-0.2702	0.1634
H3A	-0.1290	-0.1467	0.3500	-0.1312	-0.1499	0.3678
H3B	-0.1426	0.0350	0.1400	-0.1460	0.0625	0.1433
H2A	-0.1046	-0.4910	0.1450	-0.1020	-0.4834	0.1506
H2B	-0.1210	-0.3393	-0.0620	-0.1196	-0.3318	-0.0857

on site block of the real space representation of this downfolded Hamiltonian provides the estimate of various *d* level energies as shown in Fig. (7.6). In this calculation, the choice of local coordinate axes has been adopted with local z-axis pointing along the shortest Mn-O bond and local y-axis pointing approximately along the Mn-O bond in the plane perpendicular to that. The Mn-*d* states are found to cluster around three energies, with close spacing of *xy*, *yz* and *zx* states while x^2- y^2 and $3z^2$-r^2 states are split off by large energy gaps of around 0.5 eV. The middle and bottom panels of Fig. (7.4) show Mn1-*d* and Mn2-*d* projected density of states. The sharp peaked nature of the density of states with narrow bandwidths point towards relatively weak interactions between Mn ions which is also evident from low ordering temperature. The insets show the contribution of C-*p* (left panel) and O-*p* (right panel)

Table 7.2 Bond lengths(Å) and Bond angles(^{o}) for the theoretically optimized structure compared to the experimentally determined structure.

Bond	Measured Structure	Optimized Structure
Mn1-O1	2.13 Å	1.95 Å
Mn1-O2	2.21Å	2.22 Å
Mn1-O2	2.23Å	2.14 Å
Mn1-O2-Mn1	108.9^o	112.3^o
Mn2-O3	2.08Å	1.96Å
Mn2-O4	2.24Å	2.23Å
Mn2-O4	2.36Å	2.29Å
Mn2-O4-Mn2	119.2^o	122.6^o

respectively in the energy range which is dominated by Mn-*d* character. For Mn1 the contributions from bonded O1 and O2 and the intervening C atom in O1-C1-O2 bridge have been considered, while for Mn2 correspondingly the contributions from O3 and O4 and C4 have been considered. These plots clearly indicate much larger mixing between Mn1-*d* and O1-*p*, O2-*p*, C1-*p* compared to that between Mn2-*d* and O3-*p*, O4-*p*, C4-*p*.

Fig. (7.7) shows the spin polarized density of states of $Mn(C_4H_4O_4)$, which gives rise to an insulating solution within GGA. The upper panel of Fig. (7.7) show Mn1-*d* projected density of states while the lower panel show the Mn2-*d* projected DOS. Both Mn1 and Mn2 spinpolarized DOS show rather large spin splittings at Mn sites giving rise to all Mn-*d* states being occupied in the majority spin channel and being empty in the minority spin channel. The resulting magnetic moments are listed in Table. 7.3. In agreement with the insulating nature of the solution and nominal d^5 valences of Mn^{+2}, total moment per formula unit turns out to be 5 μ_B. Out of 5 μ_B about 4.6 μ_B resides on Mn sphere while the rest are distributed between oxygens and carbons. The C atoms attached to the Mn atoms (*e.g.* C1 and C4), carry significantly larger moments compared to those belonging solely to ligands (C2 and C3). Among all the oxygen atom bonded to Mn atoms O1 and O4 carry maximum magnetic moment because O4 is the corner sharing oxygen between two $Mn2O_6$ octahedra while O1 forms the part of bridge that connects two Mn1 atom belonging to two neighboring chains. It is interesting to

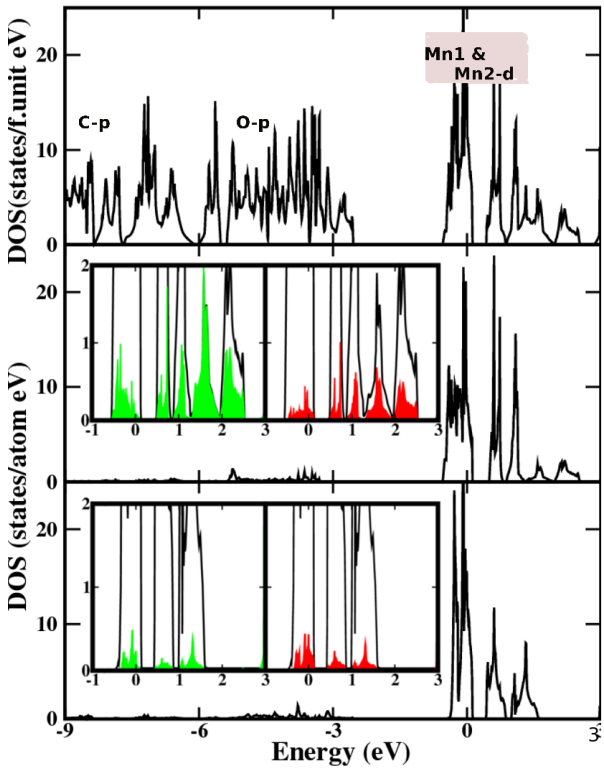

Figure 7.4 GGA non spinpolarized density of states of Mn succinate. The top panel shows the total density of states while the middle and bottom panels show the density of states projected onto Mn1-*d* and Mn-2-*d* characters respectively.The insets in the middle and bottom panels show the C-*p* projected states (left insets) and O-*p* projected states (right insets) marked as shaded regions in green/red in comparison to Mn-*d* projected states in solid lines.

note that the moment at O1 is about twice larger than that of O2, reflecting the super-super exchange path via O1-C1-O2 connecting Mn1 atoms belonging to two neighboring chains to be stronger than the edge sharing super exchange path via O2 connecting two Mn1 atoms belonging to the same chain.

7.2.3 Low Energy Hamiltonian and Hopping Interaction

To understand the nature of effective Mn-Mn interactions, we computed the effective hopping interactions connecting different Mn sites in the compound. These are obtained as the off diagonal blocks of the real space representation of the downfolded Hamiltonian in which Mn1-*d* and Mn2-*d* degrees

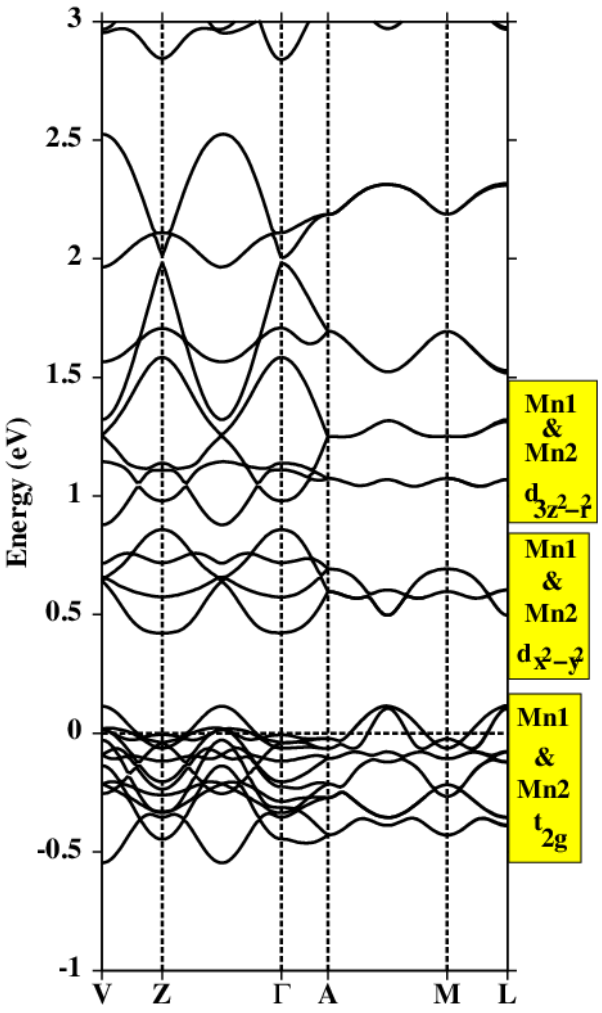

Figure 7.5 Mn-*d* orbital projected GGA non spin polarized band structure. Different band characters are marker in the figure.

of freedom have been kept active and the rest have been downfolded. We found that the computed interactions consist of mainly three dominant interactions, t_1, t_2 and t_3. The interaction between 5-*d* orbitals of Mn at a given site and 5-*d* orbitals of Mn at the connecting site, gives rise to 5×5 blocks for each of the interactions t_1, t_2, t_3. The t_1 and t_2 interactions connect two Mn1 sites, while t_3 connects two Mn2 sites. t_1 and t_2 denote the intra-chain and inter-chain Mn1-Mn1 interactions respectively and t_3 defines the nearest neighbor Mn2-Mn2 interaction in the Mn2 layer as shown in Fig. (7.8). The interactions connecting Mn1 and Mn2 belonging to two different layers were found to be orders of magnitude smaller compared to those within layers, confirming the independent nature of Mn1 and

Table 7.3 Magnetic Moments (in μ_B) at different sites as obtained in spin-polarized GGA calculation.

Atom	Moments
Mn1	4.570
Mn2	4.640
O1	0.052
O2	0.028
O3	0.026
O4	0.044
C1	0.070
C2	0.002
C3	0.001
C4	0.044
Total/f.unit	5.000

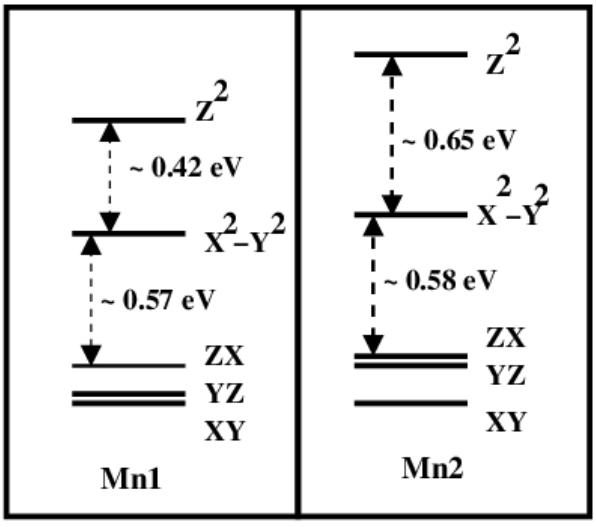

Figure 7.6 The positions of *d* energy levels at Mn1 and Mn2 sites obtained from NMTO downfolding calculation.

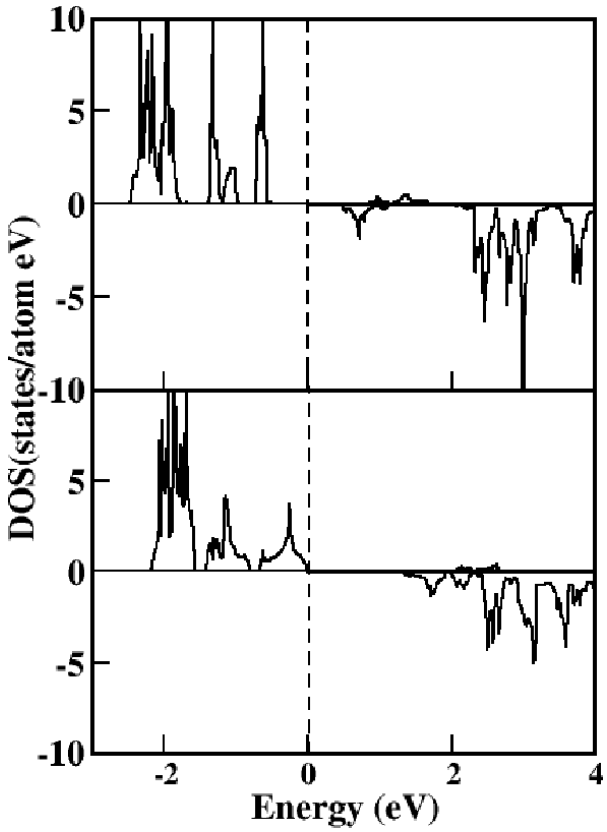

Figure 7.7 Spin polarized GGA density of states. Upper panel for Mn1 and lower panel for Mn2.

Mn2 layers with little connection with each other.

In terms of the Mn-Mn distance, the hopping interaction t_1 is the shortest neighbor interaction and t_2 is the longest neighbor interaction among the three interactions. The hopping interactions are listed in Table. 7.4. Hopping interactions show that the largest hopping integral is that connecting Mn1-*yz* and Mn1-*yz* belonging to hopping t_2, whereas the hopping between $3z^2$-r^2 and *yz* and that between *xz* and *xy* are also substantially large. This is followed by Mn2-x^2-y^2 and Mn2-*yz* hopping belonging to t_3. The hopping belonging to t_1 is much weaker compared to others. To understand this counter intuitive trend in the calculated hopping integral values, we plot in Fig. (7.9), the overlap of the underlying Wannier functions placed at two Mn sites corresponding to the strongest hopping within each of the interactions, t_1, t_2 and t_3 (from left to right). The central part of the Wannier function are shaped according to the symmetry of effective Mn-*d* character, whereas the tails sitting at the different sites are

Table 7.4 List of dominant Hopping Interactions for $Mn(C_4H_4O_4)$.

Hopping Interactions

Mn1-Mn1 intra-chain: Distance=3.61 Å

$$t_1 = \begin{pmatrix} & xy & yz & 3z^2 & xz & x^2-y^2 \\ xy & -0.04 & 0.02 & -0.02 & 0.04 & -0.05 \\ yz & 0.00 & 0.04 & 0.01 & 0.06 & 0.03 \\ 3z^2 & 0.00 & -0.02 & 0.02 & 0.03 & 0.03 \\ xz & 0.02 & -0.02 & -0.02 & -0.04 & 0.02 \\ x^2-y^2 & -0.05 & 0.03 & 0.01 & -0.03 & 0.03 \end{pmatrix}$$

Mn1-Mn1 inter-chain: Distance=4.39 Å

$$t_2 = \begin{pmatrix} & xy & yz & 3z^2 & xz & x^2-y^2 \\ xy & -0.07 & 0.04 & 0.00 & -0.00 & -0.02 \\ yz & -0.07 & -0.18 & 0.01 & 0.01 & 0.08 \\ 3z^2 & 0.04 & 0.11 & -0.02 & -0.03 & -0.06 \\ xz & 0.11 & 0.05 & -0.00 & 0.00 & -0.05 \\ x^2-y^2 & 0.05 & -0.02 & -0.01 & 0.02 & -0.02 \end{pmatrix}$$

Mn2-Mn2 intra-plane: Distance=3.97 Å

$$t_3 = \begin{pmatrix} & xy & yz & 3z^2 & xz & x^2-y^2 \\ xy & 0.02 & 0.04 & 0.04 & -0.03 & -0.05 \\ yz & -0.06 & 0.00 & 0.04 & 0.01 & -0.04 \\ 3z^2 & 0.00 & -0.06 & -0.05 & 0.01 & 0.03 \\ xz & 0.00 & 0.02 & 0.01 & 0.01 & 0.00 \\ x^2-y^2 & 0.02 & 0.06 & 0.01 & 0.10 & 0.03 \end{pmatrix}$$

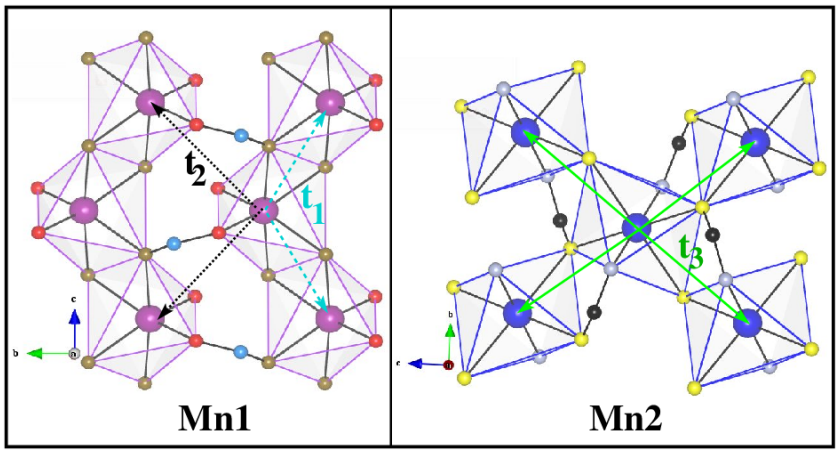

Figure 7.8 Dominant Mn-Mn hopping interactions. Left panel: Mn1-Mn1 intra-chain interaction, t_1 and inter-chain interaction, t_2, Right panel: Mn2-Mn2 interaction, t_3.

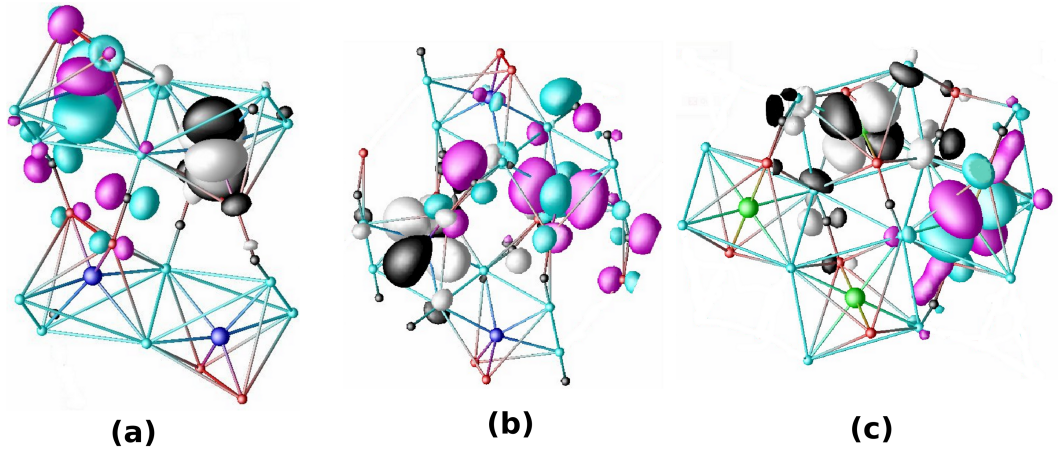

Figure 7.9 (a) Overlap of downfolded d_{xy} and $d_{x^2-y^2}$ NMTOs, placed at two Mn1 sites corresponding to the intra-chain interaction, t_1. (b) Overlap of downfolded d_{yz} NMTOs, placed at two Mn1 sites corresponding to the inter-chain interaction, t_2. (c) Overlap of downfolded d_{xz} and $d_{x^2-y^2}$ NMTOs, placed at two Mn2 sites corresponding to the t_3 interaction. Lobes of the orbitals placed at different sites are colored differently. Plotted are the orbital shapes (constant amplitude surfaces) with the lobes of opposite signs colored black (magenta) and white (cyan) at 1^{st} (2^{nd}) Mn site.

shaped according to the integrated out orbitals at their respective sites. The weights at the neighboring O and C sites depend on the extent of mixing between the respective Mn-*d* and the respective O-*p* or C-*p* and the overlap of the tails between two Wannier functions define the corresponding super-exchange path. Focusing on to the left panel (Fig. (7.9)(a)), we find the overlap between two Wannier functions, corresponding to the hopping belonging to t_1 are minimal, with two Wannier functions being aligned in two different directions which is expected for the edge shared nature of the interaction.

The hopping belonging to t_2 on the other hand is strong due to strong mixing of O-*p* and C1-*p* with Mn1, resulting into the tails of the Wannier functions forming a well defined super-super exchange path of O1- C1-O2 between two Mn atoms, as shown in the middle panel of Fig. (7.9(b)). For the case of corner shared Mn2's, there are two possible super-exchange paths, one is via corner shared O4 type oxygen and another is via succinate ligands (O3-C4-O4). The right panel *i.e* Fig. (7.9(c)) shows the overlap plot corresponding to this interaction t_3. The plot shows that the strength of overlap is minimal via the corner shared O4 path. This is because the corner shared Mn2-O4-Mn2 angle is 119.2^o, much less than 180^o. Therefore the strength of the interaction in this path is weaker compared to that expected for perfect corner shared situation. Also the other hopping path via succinate ligands contributes negligibly due to absence of any weight along the O3-C4-O4 bridge. This forms the rational for inter-chain Mn1-Mn1 interaction to be stronger than the corner shared Mn2-Mn2 interaction as reflected in the computed hopping integrals.

7.2.4 Magnetic Exchange Interaction

From the knowledge of hopping interactions, the magnetic exchange interactions may be derived through the use of super-exchange like formula as stated in the earlier chapters. However this requires knowledge of charge transfer energy which is difficult to estimate for complicated paths. We therefore attempted to estimate the magnetic exchange interactions using total energy calculations of various spin configurations and mapping the DFT total energy to the corresponding Ising model similar to the the previous cases discussed in the previous chapters. This approach, as established, is successful in predicting the qualitative estimation of exchange interactions [15]. The total energy calculation shows that the Mn1-Mn1 inter-chain exchange interaction (J_2) to be the strongest and of antiferromagnetic nature followed by the Mn2-Mn2 exchange (J_3) which is also of antiferromagnetic nature. The intra-chain

Mn1-Mn1 exchange (J_1) turn out to be of ferromagnetic nature. Experimentally it is observed that the edge shared ferromagnetic chains are coupled antiferromagnetically with a sinusoidal modulation. Our calculations correctly reproduced the ferromagnetic nature of intra-chain interaction and antiferromagnetic nature of inter-chain interaction. The sinusoidal modulation is driven by longer ranged inter-chain exchange not taken into account in our calculation. The antiferromagnetic nature of the corner shared Mn2-Mn2 interaction is also in good agreement with the experimental observation. The strength of the antiferromagnetic, corner sharing Mn2-Mn2 interaction came out to be about one third of the strength of the antiferromagnetic inter- chain Mn1-Mn1 interaction, which dominates the magnetic interactions within the Mn1 layer. The absolute values of the exchanges turned out to be small (1-2 meV) in agreement with the rather low ordering temperatures observed experimentally. Taking into account the calculated magnetic exchange, the mean field ordering temperature within Mn1 layer turned out to be about 60% larger than that within Mn2 layer in very good agreement with experimentally observed ratio of ordering temperatures within Mn1 and Mn2 layers.

7.3 Conclusion

We have studied the electronic and magnetic structure of the recently synthesized hybrid framework compound, $Mn(C_4H_4O_4)$. The compound contains extended connectivity of Mn layers which are separated by succinate ligands. Our DFT-based study brought out the trend in magnetic ordering surprisingly well. Our calculations showed that the magnetic interactions within the Mn layer formed by edge sharing of MnO_6 octahedra, are stronger than that within the Mn layer formed by corner shared MnO_6 octahedra, with almost no interaction between the two layers. This leads to a two step magnetic ordering process, with the edge shared Mn layer ordering first, followed by the ordering in corner shared Mn layer in the second step. This is in accordance with the experimental observations. The ratio of the mean field ordering temperature based on computed magnetic interactions between the one in the edge shared Mn layer and that in the corner shared Mn layer was found to be in very good agreement with the experimental findings, the first ordering temperature being 60% larger than the second one. The microscopic origin of this behaviour, turned out to be driven by the differential strength of covalency between Mn-*d* and *p* states of surrounding oxygen and carbon atoms in the edge shared and corner

shared layers.

Bibliography

[1] US National Library of Medicine National Institutes of Health Search term Search database. *http://www.ncbi.nlm.nih.gov/pmc/articles/PMC1314946/*

[2] C. Livage, C. Egger, M. Nogues and G. Ferey, J. Mater. Chem. **8**, 2743 (1998); C. Livage, C. Egger and G. Ferey, Chem. Mater. **11**, 1546 (1999).

[3] A. B. Gaspar, M. C. Muñoz and J. A. Real, J. Mater. Chem. **16** 2522 (2006).

[4] O.Kahn and C. Jay Martinez, Science **279**, 44 (1998).; P. Gamez, J. Sanchez Costa, M. Quesada and G. Aromi, Dalton Trans. 7845 (2009).; P. Gütlich, A. Hauser and H. Spiering, Angew. Chem. Int. Ed. **33**, 2024 (1994).

[5] Leslie J. Murray, Mircea Dinca and Jeffrey R. Long, Chem. Soc. Rev. **38**, 1294 (2009).

[6] M. Kosa, J. C. Tan, C.A. Merrill, M. Krack, A. K. Cheetham and M. Perrinello, Chem. Phys. Chem **11**, 2332 (2010).

[7] C. N. R. Rao, A. K. Cheetham and A. Thirumurugan, J. Phys.: Condens. Matter. **20**, 083202 (2008).

[8] S. Wang, Y. Hou, E. Wang, Y. Li, L. Xu, J. Peng, S. Liua and C. Hua, New. J. Chem. **27**, 1144 (2003). ; F. Serpaggi, T. Luxbacher, A. K. Cheetham and G. Ferey, J. Solid State Chem. **145**, 580 (1999).

[9] Y. Z. Tang, X-F Huang, Y-M Song, P.W.H Chan and R-G Xiong, Inorg. Chem. **45**, 4868 (2006).

[10] J. H. Choy, S. J. Kwon, S. J. Hwang, Y. Kim, and W. Lee,J. Mater. Chem **9**, 129 (1999). ; Y. Misaki, Sci. Technol. Adv. Mater. **10**, 024301, (2009).

[11] C. N. R. Rao and C. R. Serrao, J. Mater. Chem. **17**, 4931 (2007).

[12] Paul. J. Saines, B. C. Melot, R. Seshadri, A. K. Cheetham, Chem. Eur. J **16**, 7579 (2010).

[13] Paul. J. Saines, J. R. Hester, A. K. Cheetham, Phys. Rev. B **82**, 144435 (2010).

[14] P. Hohenberg and W. Kohn, Phys. Rev. **136**, B864 (1964). ; W. Kohn and L. J. Sham, Phys. Rev. **140**, A1133 (1965).

[15] C. S. Helberg, W. E. Pickett, L. L. Boyer, H. T. Stokes and M. J. Mehl, J. Phys. Soc. Jpn. **68**, 3489 (1999).

Chapter 8

Pressure and Temperature Driven Spin-switching in Metal-organic Coordination Polymers from ab initio Calculations*

8.1 Introduction and motivation of the present work

Spin-crossover (SCO) transition is a phenomenon in which the spin state of a transition switches reversibly between different values due to an external perturbation such as pressure, temperature, light irradiation, or magnetic field [1]. Such SCO transition has been quite common in the coordination polymers [3] with Fe^{2+} building blocks [4] which can be used for various application purposes such as memory devices, optical information storage and displays [5]. To become a useful candidates for such application purposes the system should have bistable electronic states which are cooperatively connected to each other. Though the SCO transition can be understood qualitatively by the ligand filed theory [6], as a competition between the splitting between t_{2g} and e_g energy levels, and the Hund's rule coupling (J_H) between the d electrons, this scheme is insufficient for the prediction of material specific SCO phenomena. On the other hand the theoretical approach of studying such SCO transitions

*This chapter is based on *Phys. Rev. Lett. 109, 077203 (2012)*

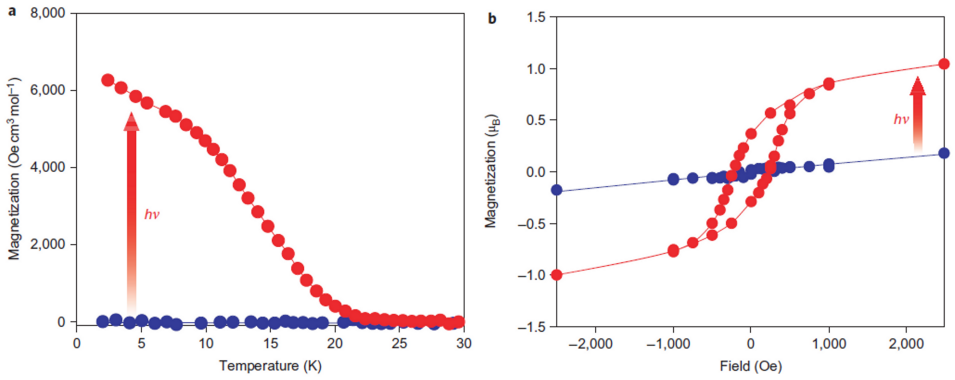

Figure 8.1 light-induced spin-crossover phenomena. a) Magnetization vs. temperature plot at 100 Oe. Light irradiation induces a spontaneous magnetization with curie temperature 2 K. b) Magnetic hysteresis curves at 2 K. Light irradiation, opens up a hysteresis loop with a coercive field of 240 Oe. Circles denote measurements before and after irradiation with 473 nm light. Figures reproduced from Ref. [10]

are restricted within the models based on elastic interactions [7] among the different transition metal sites. Recently contribution of magnetic exchange interaction [8] in building up cooperativity has been pointed out. Therefore the natural choice to understand the microscopic level of the SCO phenomenon and its cooperativity in extended systems like coordination polymers would be the density-functional theory (DFT) based calculations. This is however very challenging given the complex nature of the crystalline environment involving several SCO atoms in the unit cell and moreover, the description of the phenomenon requires proper handling of the subtle changes in the crystal structure as well as the electronic structure upon application of external stimuli.

In the present study we focus on the recently synthesized bimetallic, coordination polymeric compound, $Fe_2[Nb(CN)_8].(4\text{-pyridinealdoxime})_8.2H_2O$ [10], using combination of *ab-initio* DFT+U and *ab-initio* molecular dynamics approach. Experimentally it has been observed that this bimetallic polymer undergoes spin state transition by irradiation of laser light of appropriate frequency as shown in Fig. (8.1). Our motivation is to explore and understand how the spin state transition gets influenced by other external perturbations, like pressure, temperature or chemical substitution.

8.2 Calculation details

In the first-principles DFT calculations we have used the plane wave basis set and pseudo-potentials as implemented in the Vienna Ab-initio Simulation Package (VASP) [11] with choice of Projector-Augmented Wave (PAW) potential [12]. The exchange-correlation function was chosen to be that of generalized gradient approximation (GGA) implemented following the parametrization of Perdew-Burke-Ernzerhof [13]. During the structural optimization the position of the ions were relaxed towards equilibrium until the Hellmann-Feynman forces become less than 0.01 eV/Å. For the plane wave calculation a 500 eV plane wave cutoff was used. A k-point mesh of $3\times3\times4$ in the Brillouin zone was used in the calculations. The missing correlation effect of the transition metals is incorporated through LDA+U [14] calculations. To check the consistency of U values in our calculations we varied the U values at Fe site from 3 eV to 6 eV and at Nb site from 1 eV to 2 eV. The results reported in this chapter are for the choice of U being 5 eV at the Fe site and 2 eV at the Nb site, and the J value set to 1 eV for both Fe and Nb. The ab initio molecular dynamics (AIMD) method used in the present work is as implemented in VASP within the framework of the canonical ensemble (NVT). The temperature was increased or decreased from an initial value, using a Nosé-Hoover [15] thermostat with a time step of 1 fs for each molecular dynamics step and 600 temperature steps between initial and final temperature. At the final step the system was further thermalized for a time duration of 1 ps.

8.3 Results and Discussion

8.3.1 Crystal Structure

$Fe_2[Nb(CN)_8].(4\text{-pyridinealdoxime})_8.2H_2O$ forms a three dimensional connected network of Fe-Nb atoms which are bridged by cyanide (CN).The crystal structure formed in the tetragonal space group $I4_1/a$ [10] consists of three basic building blocks, distorted FeN_6 octahedra, NbC_8 dodecahedra and cyanide (CN)-bridge. The schematic figure of the crystal structure are shown in the Fig. (8.2). The two apical positions of the octahedral units are formed by cyanide N atoms while the other four positions are formed by N atoms belonging to rings of 4-pyridinealdoxime. Among the eight CN groups connected to Nb, four are connected to Fe while the remaining four are free and saturated by hydrogens. Some of

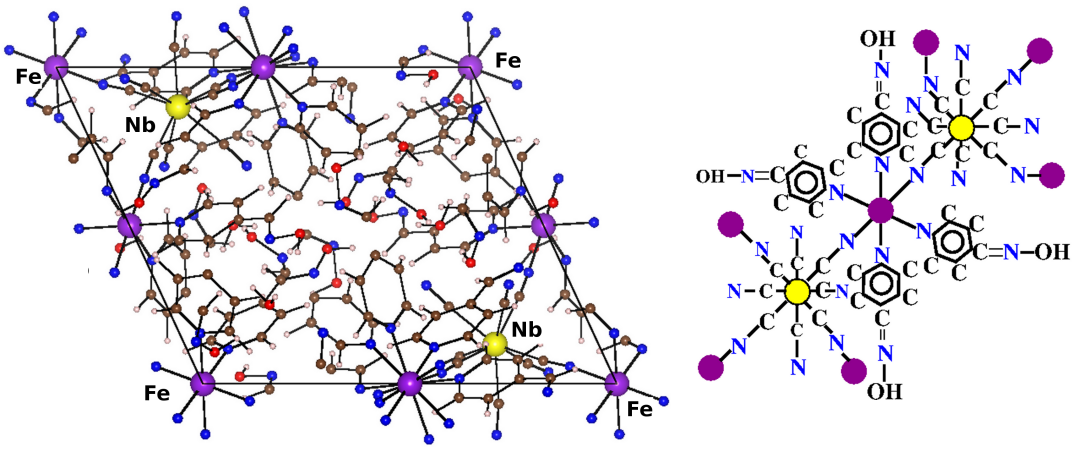

Figure 8.2 Left panel shows the crystal structure of the system in a tetragonal unit cell. Fe , Nb, N, C, O and H atoms are represented by magenta, yellow, blue, brown, red and pink color balls respectively. Right panel highlights the environment around Fe and Nb sites.

the waters are connected to the hydroxyl group of 4-pyridinealdoxime through hydrogen bridges and the rest are non bonded, giving rise to a total of 290 atoms in the unit cell.

8.3.2 Structural optimization: Effect of hydrostatic pressure

The reported crystal structure data [10] obtained by Rietveld refinement of the powder X-ray diffraction measured at 300 K does not contain the hydrogen positions which are difficult to detect through X-ray diffraction. In the first step, starting from the reported crystal structure data, we therefore positioned the hydrogen atoms at their suitable positions as demanded by the symmetry and the crystal structure of the compound and relaxed their positions by minimizing the forces while keeping the positions of other atoms and the lattice constants fixed at their experimental measured values. The calculated electronic structure carried out on this structure shows that the Fe is in high spin (HS) state with a magnetic moment at Fe site (M^{Fe}) of 3.75 μ_B and the moment at Nb site (M^{Nb}) is obtained to be -0.58 μ_B, aligned antiparallely to the Fe moment. This confirms that Fe^{2+} valence with S=2 and Nb^{4+} valence with S=1/2 spin and the antiferromagnetic coupling between Fe and Nb spins, as deduced in the experimental study [10]. In the next step, starting from the HS structure (ambient conditioned experimental structure), we reduced the unit cell volume keeping the shape and the aspect ratios of the unit cell same as that of the HS structure, which mimic the application of uniform hydrostatic pressure, and re-optimized all the

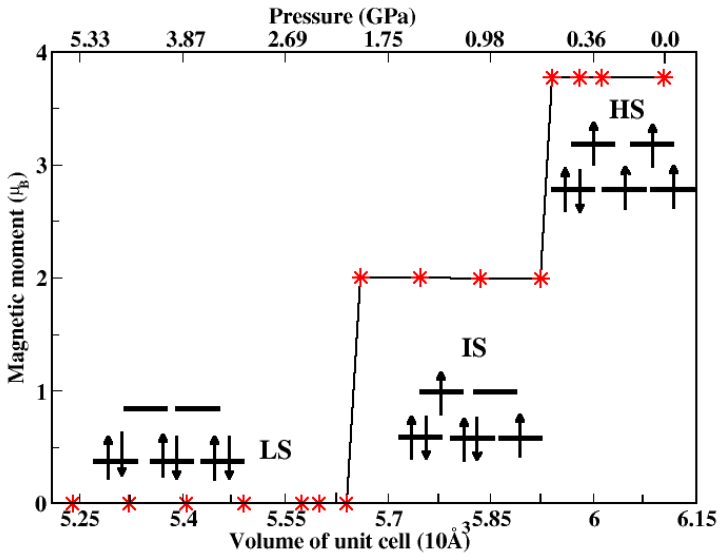

Figure 8.3 Computed magnetic moment at the Fe site plotted *vs* the unit cell volume of the Fe-Nb complex. The hydrostatic pressures corresponding to selected volumes are marked in the upper ordinate. The t_{2g} and e_g orbital occupations of Fe in HS, IS and LS states are shown schematically.

atomic positions. The obtained results are summarized in the Fig. (8.3). Upon volume reduction, we find a remarkable, two-step spin transition process at the Fe site, with first transition from *High spin* (HS) (M^{Fe}= 3.75 μ_B) to *Intermediate Spin* (IS) (M^{Fe}= 2.00 μ_B) upon volume reduction by $\approx$ 3%, and consecutively to *Low Spin* (LS) (M^{Fe}= 0.0 μ_B) upon further reduction of volume by $\approx$ 7%, while the Nb moment stays more or less constant, $M^{Nb} \approx 0.6\mu_B$. The details of the theoretical optimized crystal structures for the three spin states are shown in Table. 8.1

This two-step transition is driven by the changes in the Fe-N bond lengths, the average Fe-N bond length along C-N bridges reduces from a value of 2.04 Å at HS state to 1.93 Å in IS state to 1.91 Å in LS state. The average Fe-N bond length along the 4-pyridinealdoxime rings also shows a substantial change from an average value of 2.23 Å in HS state to 2.09 Å in IS state to 2.04 Å in LS state. To understand the nature of cooperative behavior of this extended network system we calculate the magnetic moment in two different cycles, once starting from the ambient pressure HS state structure and gradually decreasing the unit cell volume upto high pressure LS state structure and then in the next

Table 8.1 The optimized theoretical crystal structure for ambient pressure, and for 2.94% and 7.58% reduced volumes. During the optimization the lattice parameters are kept fixed at the mentioned values. The space group is in all three cases $I4_1/a$. The atomic coordinates are given in IORIGIN=1 setting.

Atom	Ambient Pressure a=20.200 Å, c=14.956 Å			2.94% reduced volume a=20.000 Å, c=14.808 Å			7.52% reduced volume a=19.680 Å, c=14.571 Å		
	x	y	z	x	y	z	x	y	z
Fe	-.2500	0.0000	0.3750	-.2500	0.0000	0.3750	-.2500	0.0000	0.3750
Nb	0.0000	0.0000	0.5000	0.0000	0.0000	0.5000	0.0000	0.0000	0.5000
C1	0.1257	0.0723	-.0122	0.1285	0.0729	-.0083	0.1243	0.0722	-.0106
C2	0.1558	0.0512	0.0718	0.1576	0.0523	0.0777	0.1556	0.0488	0.0744
C3	0.1218	0.0640	0.1516	0.1233	0.0668	0.1577	0.1218	0.0620	0.1572
C4	0.2176	0.0199	0.0778	0.2198	0.0202	0.0848	0.2185	0.0153	0.0807
C5	0.1485	0.0430	0.2322	0.1502	0.0474	0.2396	0.1494	0.0411	0.2393
C6	0.2420	0.0032	0.1617	0.2441	0.0039	0.1699	0.2447	-.0006	0.1664
C7	0.0073	0.0683	0.3811	0.0070	0.0696	0.3809	0.0064	0.0696	0.3767
C8	0.2394	0.1764	-.1469	0.2359	0.1730	-.1456	0.2560	-.1788	-.1016
C9	0.2854	-.1858	0.1296	0.2828	-.1831	0.1249	-.1055	0.0035	0.4567
C10	-.1032	0.0033	0.4573	-.1063	0.0044	0.4537	0.2893	-.1857	0.1288
C11	0.2811	0.1958	0.1319	0.2775	0.1975	0.1368	0.2869	0.1929	0.1328
C12	0.2440	0.2474	-.1303	0.2416	0.2441	-.1269	0.1407	0.1886	-.3680
C13	0.1463	0.1897	-.3689	0.1483	0.1875	-.3630	0.2461	0.2513	-.1302
C14	-.1965	-.1505	0.3915	-.1977	-.1535	0.3984	-.1944	-.1431	0.3928
N1	0.1428	0.0452	-.0871	0.1423	0.0414	-.0823	0.1469	0.0534	-.0899
N2	0.1076	-.0167	-.3247	0.1104	-.0157	-.3249	0.1092	-.0147	-.3173
N3	0.2120	-.1372	-.1215	0.2139	-.1327	-.1137	0.2090	-.1396	-.1336
N4	0.2081	0.0136	0.2382	0.2100	0.0168	0.2466	0.2108	0.0118	0.2460
N5	-.1581	0.0017	0.4320	-.1613	0.0038	0.4256	-.1613	0.0033	0.4285
N6	-.2476	0.1137	0.3601	-.2461	0.1160	0.3531	-.2477	0.1060	0.3606
O1	0.0000	0.0000	0.1000	0.0000	0.0000	0.1000	0.0000	0.0000	0.1003
O2	0.1133	0.0681	-.1639	0.1137	0.0646	-.1606	0.1140	0.0804	-.1660
O3	0.2266	-.0729	-.0952	0.2315	-.0685	-.0879	0.2166	-.0742	-.1008

	x	y	z	x	y	z	x	y	z
H1	0.0327	-.0202	-.0609	0.0384	-.0064	-.0606	0.0305	-.0248	-.0603
H2	0.1120	-.0882	0.0090	0.1163	-.0945	0.0084	0.1081	-.0812	0.0033
H3	0.0866	-.0692	0.1496	0.0913	-.0735	0.1456	0.0789	-.0645	0.1546
H4	0.0895	-.0743	-.1535	0.0924	-.0753	-.1594	0.0884	-.0736	-.1610
H5	0.1900	-.0440	-.1152	0.1930	-.0382	-.1004	0.1880	-.0445	-.1394
H6	0.2479	0.0104	0.0190	0.2511	0.0100	0.0263	0.2486	0.0031	0.0202
H7	0.1206	0.0509	0.2935	0.1225	0.0568	0.3012	0.1215	0.0492	0.3023
H8	0.1938	0.1570	-.1769	0.1877	0.1539	-.1700	0.2029	0.1580	-.1904
H9	0.2545	0.1490	0.1317	0.2597	-.1342	0.1340	0.2605	0.1442	0.1310
H10	0.2620	-.1376	0.1383	0.2503	0.1504	0.1367	0.2652	-.1364	0.1369
H11	0.2916	-.0172	0.1684	0.2937	-.0178	0.1770	0.2955	-.0215	0.1727
H12	-.1450	0.1161	0.3691	-.1424	0.1175	0.3630	-.1428	0.1100	0.3658
H13	-.1500	-.1236	0.3999	-.1507	-.1268	0.4088	-.1474	-.1150	0.4042

cycle starting from the LS state high pressure structure and keep on increasing the unit cell volume upto the ambient pressure structure and calculate the magnetic moment at each step. The results are shown in Fig. (8.4). We find the transitions to be extremely sharp, showing finite hysteresis behavior between the up-down cycle which is indication of the cooperative behavior of the system, induced by the coordination polymer geometry. Considering typical bulk modulus values of metal-organic systems, B_0= 20 GPa and $(\frac{\delta B_0}{\delta P})_{V_0}$= 7 [18], the volume reduction of $\approx$ 3% (required to drive the HS to IS transition) would amount to application of about 1 GPa pressure while $\approx$ 7% volume reduction (required to drive the HS to LS transition) would amount to about 2 GPa pressure. We note that the IS state of Fe^{2+}, though less common compared to LS or HS, has been reported in the literature [2] specially for compounds under pressure.

The spin-polarized density of states (DOS) projected on Fe-*d*, Nb-*d*, C-*p* and N-*p* are shown in Fig. (8.5), for HS, IS, and LS configurations. The top panel exemplifies the antiparallel alignment of HS Fe and Nb at ambient pressure. Interestingly, we note that for the IS configuration, the relative alignment of Nb majority and minority spin states to that of Fe is reversed compared to that in HS state,

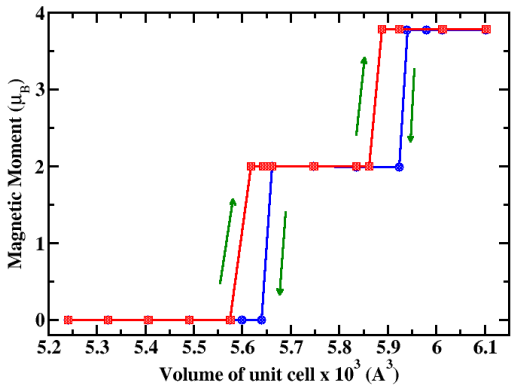

Figure 8.4 Computed magnetic moment at the Fe site plotted as a function of the unit cell volume of the Fe-Nb complex. The moment *vs* volume is the same as Fig. (8.3), but here plotted for two different paths. The data points in blue denote the path following a decreasing volume, starting from the HS state and the data points in red) denote the path following an increasing volume, starting from the LS state. Both HS $\rightarrow$ IS and IS $\rightarrow$ LS transitions exhibit interesting hysteresis effects.

i.e. predicting a parallel alignment of Fe and Nb spins. Note that within the DFT+U formulation, this metal-organic compound is predicted to be an insulator in the studied volume range.

8.3.3 Temperature effect and Ab-initio molecular dynamics (AIMD) results

Following the study of the effect of isotropic volume reduction (hydrostatic pressure), we focus on the effect of temperature. For this purpose, we carried out ab-initio molecular dynamics (AIMD) simulations, where the final temperatures were fixed at different values. First, starting from the ambient pressure 300 K HS state we could through AIMD simulations obtain the SCO transition to the LS state by fixing the quenching temperature to 20 K, in agreement with experimental observation [10]. The relative free energy difference between the HS and LS systems, $\frac{F^{HS}-F^{LS}}{F^{HS}}$, is about 10^{-5}, and $\Delta F^{HS\rightarrow LS}$=25 kJ/mol, which agrees reasonably well with relative energy estimates for SCO molecular systems [19]. Second, starting from the T=0 K optimized crystal structure of the IS state reported above, we carried out AIMD simulations setting the final temperature to 300 K. We found the AIMD simulation *to predict a temperature- driven* IS to HS transition. To make sure that the AIMD simulation captures the necessary expansion of the Fe-N bond lengths, we calculate the variation of Fe-N bond lengths as a function

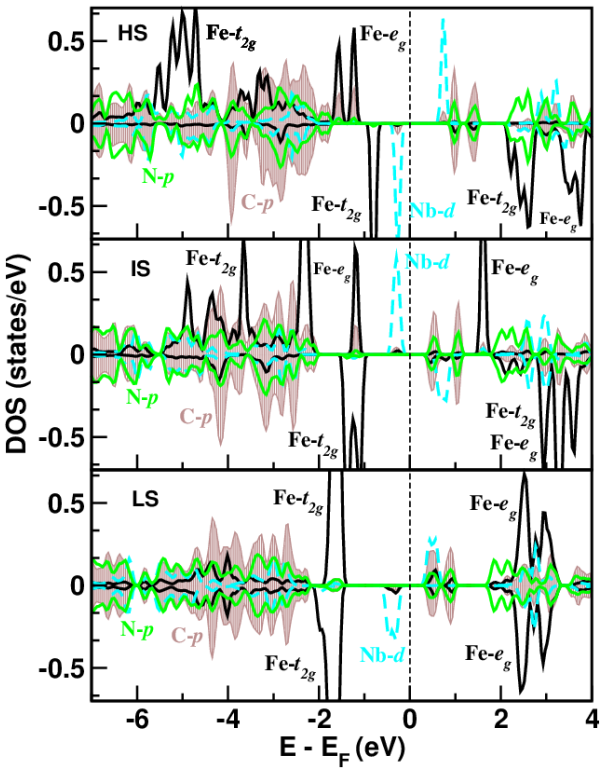

Figure 8.5 Density of states projected onto spin-polarized Fe-*d* (black, solid), Nb-*d* (cyan, dashed), N-*p* (green, solid) and C-*p* (shaded area) states, for HS, IS, and LS configurations (top to bottom panel) of the Fe-Nb SCO compound. The zero energy is set at the Fermi energy (E_F). The upper and lower subpanels in each panel, correspond to up and down spin channels, respectively.

of temperature, shown in Fig. (8.6). We found that the average value of Fe-N bond lengths varies form the value of 2.09 Å in the T=0 K structure to 2.22 Å in the 300 K structure for the Fe-N bond lengths belonging to 4-pyridinealdoxime ring. The Fe-N bond belonging to the C-N bridge changes from 1.93 Å in T=0 K structure to 2.05 Å in T= 300 K structure.

The computed Fe magnetic moment of the 300 K crystal structure was found to be 3.73 μ_B in agreement with a HS state of Fe. This HS state (referred as HS-2 hereafter) however is *distinct* from the ambient pressure 300 K HS state (referred as HS-1 hereafter) in terms of the long-range magnetic order which consists of ferromagnetically aligned Fe and Nb spins with a total magnetic moment of 9.0 μ_B/f.u., as opposed to the antiparallel aligned configuration HS-1 at ambient pressure 300 K, with a total magnetic moment of 7.0 μ_B/f.u. In order to understand the origin of this change of the nature of the magnetic coupling between Fe and Nb in the two different HS states, we plotted the magnetization density for

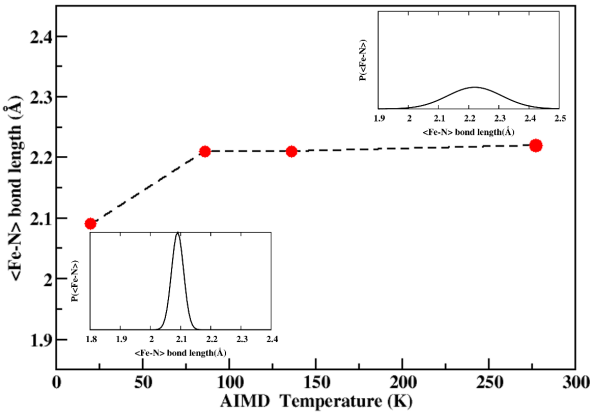

Figure 8.6 Evolution of the average Fe-N bond length as a function of temperature, starting from the low temperature IS state at 2.94% reduced volume to the high temperature HS-2 state. The insets show the computed probability distributions P of the average bond lengths at $T = 20$ K and $T = 275$ K.

the HS-1 and HS-2 state, in Fig. (8.7). We observe that the magnetic interaction connecting Fe and Nb proceeds through the Fe-N-C-Nb super-super-exchange path. Interesting changes happen with the bond angles in the connected path. While the Fe-N-C bond angle shows a change as large as about 8^o between the HS-1 and HS-2 structures, the N-C-Nb bond angle shows little change. This modification causes the relative orientation of the magnetization density at Fe and N sites to flip from antiparallel in HS-1 to parallel in HS-2 (note the change in color of the density at N site). This in turn causes the sign of the magnetization densities at C and Nb sites to flip also, which are aligned antiparallely and parallely in HS-1 and HS-2 states, respectively, to the magnetization density at the N site. This change is reflected also in the calculated magnetic moments at N and C sites, which are found to be -0.03 μ_B and +0.03 μ_B, respectively, for HS-1 and +0.06 μ_B and -0.01 μ_B, respectively, for HS-2. The change in bond angle causes a change in hopping interactions and importantly, change in the relative energy level positions, leading to changes in Fe-N hybridization between majority and minority spin channels, thereby flipping the sign of the induced moment at the N site.

8.3.4 Combined Pressure-Temperature route

The obtained pressure and temperature driven SCO transitions are summarized in the schematic diagram, Fig. (8.8), which forms the central point of our study. Note that only the temperature-induced

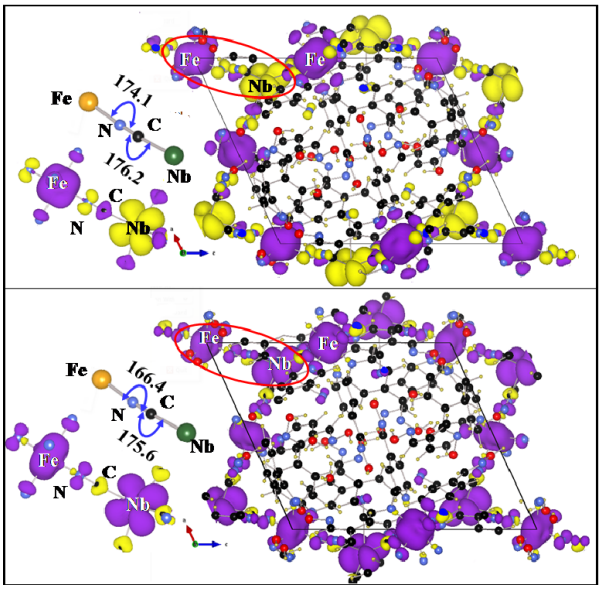

Figure 8.7 Magnetization density plots for the HS-1 (upper panel) and HS-2 (lower panel) states (isosurface value set at 0.025/Å^3). The magenta and yellow color indicates positive and negative values of the magnetization densities, respectively. Also shown are the structural comparison of the super-exchange Fe-N-C-Nb path in HS-1 and HS-2, together with a zoomed plot of the magnetization density along the super-exchange path.

transition between LS and HS-1 was thus-far observed [10], all other states are *ab initio* predictions. The plot emphasizes that employing the combined pressure-temperature route complex evolution of various spin-states can be uncovered and even the long-range order of spins can be tuned, opening up the possibility of designing SCOs from an antiferro-/ferri-magnet to a ferromagnet. A further interesting aspect of the SCO in coordination polymers is the existence of the thermal hysteresis loop. To assess the feasibility of our method to capture the thermal hysteresis one would need to carry out AIMD simulations at many different temperature values with small intervals (the width of the hysteresis is estimated to about a few K [10]) which, for the current system with $\sim$300 atoms in the unit cell, the existing computational resources did not allow us to do.

8.3.5 Mn substitution

Finally, we studied the influence of chemical substitution on this system by replacing of Fe by Mn. In the experimental [10] study the authors reported the synthesis of Mn variant of this system with somewhat different H_2O composition, but did not characterize the spin state transition behavior. So we

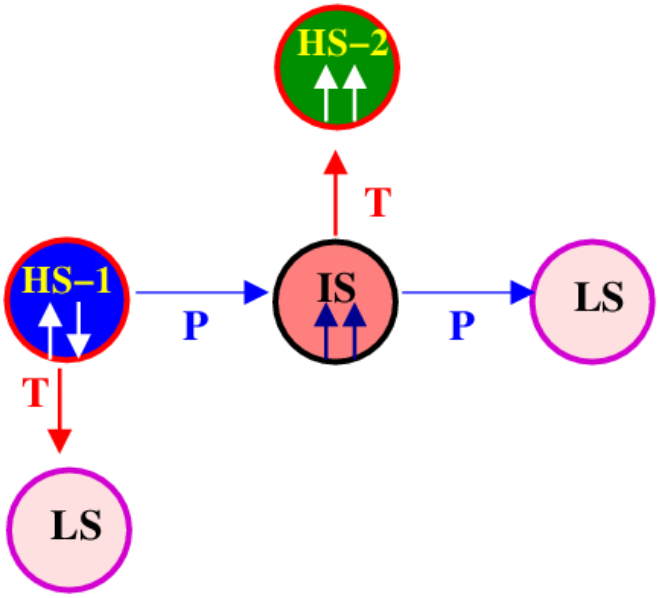

Figure 8.8 Schematic representation of the temperature-pressure induced spin-state transitions in the Fe-Nb framework.

took up this case also in our study to understand the change in the SCO behavior in the Mn variant of this system. To study computationally the effect of Fe-Mn substitution, we started with experimental crystal structure data of the Fe-Nb compound measured at 300 K, replaced Fe by Mn, performed the full optimization of the crystal structure, unit- cell volume as well as atomic positions. A HS state consisting of a Mn S=$\frac{5}{2}$ spin aligned antiparallel to a Nb S=$\frac{1}{2}$ spin was obtained, concordant with experimental observation [10] made on a related Mn-Nb framework. In the next step the effect of uniform hydrostatic pressure was investigated. We found that upon volume reduction, a one-step transition from HS (S=$\frac{5}{2}$) to LS state (S=$\frac{1}{2}$) at the Mn site was achieved around a volume reduction of 10%, amounting to application of hydrostatic pressure of about 3 GPa (see Fig. (8.9)). Comparing with Fe-Nb, we note that the Mn variant exhibits one-step transition in contrast to the two-step transition predicted for Fe compound and the HS to LS transition requires a larger volume compression compared to that of the Fe compound. We also calculate the magnetic exchange interaction along the the Fe/Mn-N-C-Nb super-super-exchange path for the both Fe-Nb and Mn-Nb systems. It turn out that magnetic interaction (J) is stronger for Mn-Nb system compared to the Fe-Nb case. The calculated values of J for Mn-Nb is $J_{Mn-Nb} \approx 5$ meV whereas for Fe-Nb case it was $J_{Fe-Nb} \approx 2$ meV. These results are

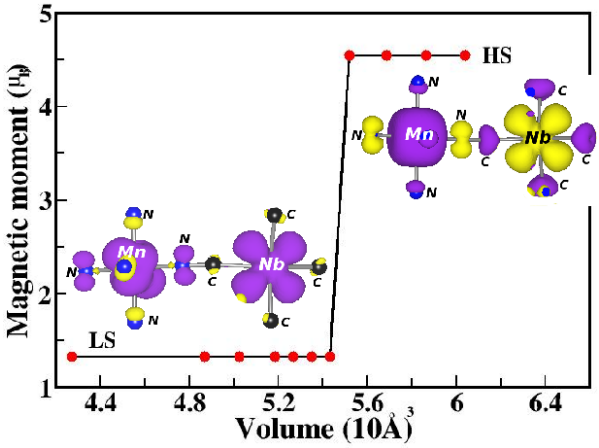

Figure 8.9 Magnetic moment at the Mn site plotted against the unit-cell volume of the Mn-Nb complex. The magnetization density plots in the insets illustrate the pressure-induced switching from ferrimagnetic alignment between Mn^{2+} (S=$\frac{5}{2}$) and Nb^{4+} (S=$\frac{1}{2}$) to ferromagnetic alignment between Mn^{2+} (S=$\frac{1}{2}$) and Nb^{4+} (S=$\frac{1}{2}$) along the superexchange path.

very much consistent with the larger volume reduction required in the case of Mn-Nb compared to the Fe-Nb case for the spin state transition. Interestingly, we again obtained the change in the nature of the long-range magnetic order from a HS state with ferrimagnetic order of Mn-$\frac{5}{2}$ and Nb-$\frac{1}{2}$ spins to a LS state with ferromagnetic order of Mn-$\frac{1}{2}$ and Nb-$\frac{1}{2}$ spins.

8.4 Conclusion

In conclusion, combination of DFT+U and AIMD calculation offers a promising first-principles approach to SCO transitions. Considering the present example, through combined pressure and temperature route, not only the known LS to HS-1 switching of spin-states of Fe in an Fe-Nb based bimetallic metal-organic coordination polymer could be explained, also switching to previously unknown spin-states has been unveiled. Furthermore, our *ab initio* simulations predict switching of the long- range magnetic order, between ferri- and ferromagnetic. The pressures predicted to induce these switching are in the range of 1-2 GPa, making verification in the laboratory feasible. Substitution of Fe by Mn leads to a one-step SCO transition between a Mn HS and LS state, as opposed to a two-step SCO transition obtained for the Fe-Nb coordination complex, from HS to IS and to LS. The successful descriptions of the SCO transitions underline that *ab initio* calculations could in the near future be employed to

map out the pressure-temperature phase diagram of SCO coordination complexes and even to design suitable SCO properties.

Bibliography

[1] *Spin Crossover in Transition Metal Compounds*, edited by P. Gütlich and H. A. Goodwin, *Topics in Current Chemistry*, **233-235** (Springer, Berlin, 2004); V. Niel, A. L. Thompson, M. C. Muñoz, A. Galet, A. E. Goeta, and J. A. Real, Angew. Chem. Int. Ed. **42**, 3760 (2003); N. Ould Moussa, G. Molnár, S. Bonhommeau, A. Zwick, S. Mouri, K. Tanaka, J. A. Real, and A. Bousseksou, Phys. Rev. Lett. **94**, 107205 (2005).

[2] P. Gütlich and H. A. Goodwin, Top. Curr. Chem. **233**, 1 (2004); J. Li *et al.*, Proc. Natl. Acad. Sci. USA **101**, 14027 (2004); C. McCammon *et al.*, Nature Geoscience **1**, 684 (2008).

[3] O. Kahn and C. J. Martinez, Science **279**, 44 (1998).

[4] P. Gamez, J. Sánchez Costa, M. Quesada, and G. Aromí, Dalton Trans. **7845** (2009).

[5] S. Bonhommeau, G. Molnár, A. Galet, A. Zwick, J. A. Real, J. J. McGarvey, and A. Bousseksou, Angew. Chem. Int. Ed. **44**, 4069 (2005).

[6] F. A. Cotton, G. Wilkinson, and P. L. Gaus, *Basic Inorganic Chemistry*, (3^{rd} Ed.) (Wiley, 1995).

[7] P. Gütlich, A. Hauser, and H. Spiering, Angew. Chem. Int. Ed. **33**, 2024 (1994); N. Willenbacher and H. Spiering, J. Phys. C: Solid State Phys. **21**, 1423 (1988); H. Spiering and N. Willenbacher, J. Phys.: Condens. Matter **1**, 10089 (1989); M. Nishino, K. Boukheddaden, Y. Konishi, and S. Miyashita, Phys. Rev. Lett. **98**, 247203 (2007).

[8] C. Timm, Phys. Rev. B **73**, 014423 (2006).

[9] T. Bucko, J. Hafner, S. Lebègue, and J. G. Ángyán, Phys. Chem. Chem. Phys. **14**, 5389 (2012).

[10] S.-i. Ohkoshi, K. Imoto, Y. Tsunobuchi, S. Takano, and H. Tokoro, Nat. Chem. **3**, 564 (2011).

[11] G. Kresse and J. Hafner, Phys. Rev. B **47**, R558 (1993); G. Kresse and J. Furthmüller, Phys. Rev. B **54**, 11169 (1996).

[12] P. E. Blöchl, Phys. Rev. B **50**, 17953 (1994); G. Kresse and D. Joubert, *ibid*, **59**, 1758 (1999).

[13] J. P. Perdew, K. Burke, and M. Ernzerhof, Phys. Rev. Lett. **77**, 3865 (1996).

[14] S. L. Dudarev, G. A. Botton, S. Y. Savrasov, C. J. Humphreys, and A. P. Sutton, Phys. Rev. B **57**, 1505 (1998).

[15] S. Nosé, Mol. Phys. **52**, 255 (1984); S. Nosé and M. L. Klein, Phys. Rev. B **33**, 339 (1985).

[16] S. Lebègue, S. Pillet, and J. G. Ángyán, Phys. Rev. B **78**, 024433 (2008).

[17] B. Gallois, J. A. Real, C. Hauw, and J. Zarembowich, Inorg. Chem. **29**, 1152 (1990).

[18] W. Zhou and T. Yildirim, Phys. Rev. B **74**, 180301(R) (2006); D. F. Bahr, J. A. Reid, W. M. Mook, C. A. Bauer, R. Stumpf, A. J. Skulan, N. R. Moody, B. A. Simmons, M. M. Shindel and M. D. Allendorf, Phys. Rev. B **76**, 184106 (2007); J. A. Greathouse and M. D. Allendorf, J. Phys. Chem. C **112**, 5795 (2008).

[19] H. Paulsen and A. Trautwein, Top. Curr. Chem. **235**, 197 (2004).

Chapter 9

Summary and Outlook

This thesis is devoted to the investigation of microscopic origin of many exciting and intriguing physical properties of different complex and novel materials, employing primarily first principles technique. In chapters 3-8, we have considered three different category of compounds, namely i) perovskite structured transition metal oxides, (Sr,Ca)RuO_3 and $BiCoO_3$, ii) low dimensional quantum spin systems $Sr_3BB'O_6$ (B=Ni/Cu, B$'$=Pt/Ir), and $Zn_2VO(PO_4)_2$ in pristine and Ti substituted form, and iii) metalorganic compounds, Mn-succinate and Fe-Nb coordination polymer. In the present chapter we summarize the central findings that emerge out of our study and discuss the future directions.

9.1 Summary

Chapter 3:

In this chapter we have studied the different aspects of perovskite ruthenate compounds $SrRuO_3$ and $CaRuO_3$. Objective of our study was two fold. Firstly, we wanted to understand the contrasting magnetic behavior of isovalent and isostructural compounds $SrRuO_3$ and $CaRuO_3$. Secondly, to explore the effect of correlation on the electronic properties of $SrRuO_3$ and $CaRuO_3$. The major findings of this study are as follows:

(i) Our study revealed an unusual evolution of the local structural parameters involving Sr atoms upon switching on magnetism. This is counter intuitive given the common belief that A-site cation

plays the role of a "spectator". This finding indicates that in these ruthenates compounds the magneto-structural coupling is mediated by the A-site cation. Our theoretical results are supported by experimental measurements.

(ii) Our DFT calculations combined with DMFT show both $SrRuO_3$ and $CaRuO_3$ to be correlated metals with reasonably high mass enhancements. The coherence temperature for $CaRuO_3$ is found to be substantially lower than that for $SrRuO_3$, providing a possible explanation for the observed non-Fermi liquid like behavior in $CaRuO_3$ and its absence in $SrRuO_3$.

Chapter 4:

In this chapter, we investigated the issue related to the changes in the electronic structure of $BiCoO_3$ between the ambient pressure (AP) phase and high pressure (HP) phase. There is an apparent controversy on the HP phase crystal symmetry and physical properties between different theoretical studies. We settle down the physical properties and crystal symmetry of $BiCoO_3$ in both ambient pressure and high pressure phase. The major findings of this study are as follows:

(i) In AP phase Co^{4+} is in high spin state (S=2) with a large gap at the Fermi level. In HP phase Co^{4+} is in low spin state (S=0) with a small but finite gap in the Fermi level. The opening of the gap is driven by the octahedral distortion. Calculated energy gap values in the two phases are consistent with the experimental resistivity measurements.

(ii) $BiCoO_3$ exists in a polar tetragonal structure and distorted orthorhombic structure in AP phase and HP phase respectively. The obtained crystal symmetry and electronic behavior are found to be guided by the the covalent mixing between O-*p* states with Bi lone pair *s* and *p* states.

Chapter 5:

Using first principle density functional theory, in this chapter we investigated the electronic structure of

a class of low dimensional quantum spin chain compounds of general formula $A_3BB'O_6$. B and B′ sites can host a wide verity of magnetic or non-magnetic cations giving rise to intra-chain and inter-chain coupling of variable sign and magnitude. In our study, we focused on three compounds, Sr_3NiPtO_6, Sr_3CuPtO_6, Sr_3NiIrO_6 formed from choice of $3d$ and $5d$ elements in B and B′ sites. In the first two cases *i.e* Sr_3NiPtO_6 and Sr_3CuPtO_6, Ni and Cu are magnetic but Pt is nonmagnetic whereas for the case of Sr_3NiIrO_6 both Ni and Ir are magnetic. The major findings of this study are as follows:

(i) In all the three cases the intra-chain interaction is substantially large compared to the other inter-chain interactions. The strength of inter-chain interactions in the case of Sr_3CuPtO_6 is found larger compared to the inter-chain interactions of the other compounds.

(ii) Calculating magnetic exchanges from total energy calculation of different magnetic configurations we found that for Sr_3NiPtO_6 intra-chain interaction is antiferromagnetic in nature and inter-chain interaction is of ferromagnetic nature. For Sr_3CuPtO_6 compound both intra-chain and inter-chain interactions are antiferromagnetic type while in the case of Sr_3NiIrO_6 the intra-chain and inter-chain interactions are found to be ferromagnetic and antiferromagnetic type, respectively.

(iii) Calculations of magneto-crystalline anisotropy energy show easy axis anisotropy in the case of Sr_3NiPtO_6 and Sr_3CuPtO_6 compound and easy plan anisotropy for Sr_3NiIrO_6 compound.

Chapter 6:

In this chapter, we studied another low dimensional quantum spin system of chemical formula $Zn_2VO(PO_4)_2$. Our aim was to settle down the apparent controversy that whether this system can be represented by 1D chain or 2D square lattice system. The other important motivation was how to destabilize the long range magnetic ordering found in the pristine system by external perturbation. The major findings of this study are as follows:

(i) From our calculated magnetic exchange interaction we found that in-plane exchange interactions

of square geometry are much stronger that the out of plane interactions of 1-D geometry. Our calculations, therefore, confirm that $Zn_2VO(PO_4)_2$ should be considered as a 2D antiferromagnetic square lattice spin $\frac{1}{2}$ system instead of previous prediction of 1D spin chain system.

(ii) We substituted $\frac{1}{4}$ of vanadium site by isovalent Ti atom. Ti substitution is found to destabilize long range antiferromagnetic ordering in 2D square lattice of the parent compound giving rise to spin gapped ground state. The underlying spin model is that of a weakly interacting 1-D spin chain. Our predictions may be verified in terms of future experimental measurements comparing with our computed thermodynamic properties.

Chapter 7:

In this chapter, we studied the electronic and magnetic structure of the organic-inorganic hybrid framework compound, Mn-succinate [$Mn(C_4H_4O_4)$]. This compound contains extended connectivity of Mn layers which are separated by succinate ligands. Experimentally it was found that this system undergoes two step magnetic ordering of Mn spins. This type of multiple transition of the same element (*i.e* Mn) is rare among the conventional inorganic system. The major findings of our study on this hybrid material are as follows:

(i) Our calculations showed that the magnetic interactions within the Mn layer formed by edge sharing of MnO_6 octahedra, to be stronger than that within the Mn layer formed by corner shared MnO_6 octahedra, with almost no interaction between the two layers. These leads to two step magnetic ordering, with edge shared octahedral Mn spins ordering first, followed by the ordering of corner shared octahedral Mn spins. These is in accordance with experimental observations. The microscopic origin of this behavior, turn out to be driven by the differential strength of covalency between Mn-*d* and *p* states of surrounding oxygen and carbon atoms in the edge shared and corner shared layers.

(ii) We found from our calculation the the ratio of mean field transition temperatures for two magnetic ordering is 0.6, while agrees with the experimental estimates, 6 K and 10 K for the two magnetic

transitions.

Chapter 8:

In the last chapter we studied another hybrid organic-inorganic system, coordination polymer compound $Fe_2[Nb(CN)_8].(4\text{-pyridinealdoxime})_8.2H_2O$. This system is known for its spin cross over phenomena upon application of light. In this study our aim was to explore other possible route of the spin state transition in this system as well as tuning of the magnetic ground state. Our major findings are as follows:

(i) This system undergoes two step spin state transition from high spin state (S=2) to low spin state (S=0) transition by the application of hydrostatic pressure. During the transition the system travel through a new intermediate spin state (S=1), which was previously not known. Both the transitions are found to be accompanied by the hysteresis effect.

(ii) The system also show spin state transition upon application of temperature.

(iii) One can tune the magnetic ordering from ferrimagnetic to ferromagnetic alignment between Fe and Nb spins by the combined route of application of temperature and pressure.

(iv) We studied the Mn variant of this system and found that it shows one step spin state transition from high spin state ($S=\frac{5}{2}$) to low spin ($S=\frac{1}{2}$) state.

9.2 Scope for future work:

(i) Study of $BaRuO_3$: Perovskite ruthenates are interesting, due to the possible interplay between the structural aspect and electron-electron correlation aspect. In literature there exists a large number of reported ruthenate materials which are not properly understood at microscopic level. As an extension

of our work on ruthenates we would wish to explore the compound $BaRuO_3$. Though $BaRuO_3$ is isovalent and has same electronic configuration as that of the previously studied two ruthenates, $SrRuO_3$ and $CaRuO_3$, it shows very different properties compared to other two. Due to the larger ionic radius of Ba^{2+} compared to Sr^{2+} and Ca^{2+} the crystal structure of $BaRuO_3$ is very different than the others. In the case of $BaRuO_3$ the tolerance factor is t=$\frac{Ba-O}{\sqrt{Ru-O}} > 1$, which favors hexagonal poly-type structures as opposed to $SrRuO_3$ and $CaRuO_3$, for which t< 1 favoring orthorhombic structure with cubic staking. $BaRuO_3$ form in a different crystal structures depending on the synthesis pressure, from 9R [ambient pressure] to 4H [3 GPa] to 6H [5 GPa], all based on hexagonal symmetry [1]. Only recently, cubic phase of $BaRuO_3$ has been synthesized under very high pressure condition [2]. The hexagonal close stacking versus cubic close staking of BaO_2 layers corresponds to the face sharing verses corner sharing connections between the two neighboring RuO_6 octahedra. The four poly-types of $BaRuO_3$ 9R, 4H, 6H and 3C exhibit varying properties. The study of $BaRuO_3$, therefore, provide an unique opportunity to study the influence structural changes within the same compound.

(ii) Surface Electronic Structure of $BiCoO_3$: In the next step in our study on $BiCoO_3$, we wish to extend our investigation to surface electronic structure of $BiCoO_3$. In particular,we wish to focus on strong spin-orbit interaction of Bi lone pair, how if modifies the surface electronic structure of $BiCoO_3$.

(iii) Study of Cooperativity in Metalorganics : The cooperative effect in extended metalorganic systems is very important. This cooperative effect arises in extended systems and not observed in isolated molecular magnetic systems. Generally this cooperative effect is manifested in terms of memory effect via commonly used temperature driven path. To simulate the temperature driven hysteresis effect in the case of large extended system containing 300-400 atoms per unit cell is a major challenge from computational perspective. For this purpose, one needs to carry out ab-initio molecular dynamics at each temperature step once in forward cycle (heating) and another is backward cycle (cooling). Our next aim is to carry out such a detailed ab-initio molecular dynamic simulation and reproduce the temperate driven hysteresis effect, pinpointing the influencing factors.

Bibliography

[1] M.L. Foo, Q. Huang, J. W. Lynn, W. L. Lee, T. Klimczuk, I. S. Hagemann, N. P. Ong and R. J. Cava; Journal of Solid State Chemistry, **179**, 563-572 (2006); A. Antoro, I. Natali Sora and Q. Huang, Journal of Solid State Chemistry, **151**, 245-222 (2000); J.G. Zhao, L.X. Yang, Y. Yu, F.Y. Li, R.C. Yu, Z. Fang, L.C. Chen and C.Q. Jin, Journal of Solid State Chemistry, **180**, 2816-2823 (2007).

[2] C.-Q. Jin, J.-S. Zhou, J. B. Goodenough, Q. Q. Liu, J. G. Zhao, L. X. Yang, Y. Yu, R. C. Yu, T. Katsura, A. Shatskiy, and E. Ito, PNAS **105**,7115-7119 (2008).